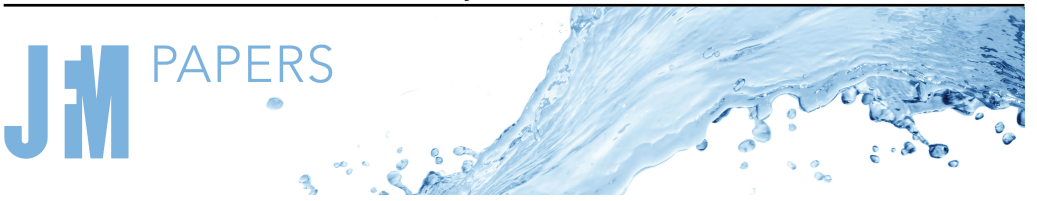
J. Fluid Mech. (2025), *vol.* 1014, A36, doi:10.1017/jfm.2025.10176



Flow in an electrically conducting drop due to an oscillating magnetic field

V. Kumaran

Department of Chemical Engineering, Indian Institute of Science, Bangalore 560012, India

Corresponding author: V. Kumaran, kumaran@iisc.ac.in

(Received 14 August 2024; revised 19 December 2024; accepted 12 April 2025)

A drop of an electrically conducting non-magnetic fluid of radius R, electrical conductivity κ, density ρ_i and viscosity η_i is suspended in a non-conducting medium of density ρ_o, viscosity η_o and subject to an oscillating magnetic field of magnitude H_0 and angular frequency ω. Oscillating eddy currents are induced in the drop due to Faraday's law. The Lorentz force density, the cross product of the current density and the magnetic field, is the superposition of a steady component and an oscillating component with frequency 2ω. The characteristic velocity due to the Lorentz force density is $(\mu_0 H_0^2 R/\eta_i)$ times a function of the dimensionless parameter $\beta = \sqrt{\mu_0 \kappa \omega R^2}$, the square root of the ratio of the frequency and the current relaxation rate. Here, μ_0 is the magnetic permeability. The characteristic velocities for the steady and oscillatory components increase proportional to β^4 for $\beta \ll 1$, and decrease proportional to β^{-1} for $\beta \gg 1$. The steady flow field consists of two axisymmetric eddies in the two hemispheres with flow outwards along the magnetic field axis and inwards along the equator. The flow in the drop induces a biaxial extensional flow in the surrounding medium, with compression along the magnetic axis and extension along the equatorial plane. The oscillating component of the velocity depends on β and the Reynolds number Re_ω based on the frequency of oscillations. For $Re_\omega \gg 1$, the amplitude of the oscillatory velocity decreases proportional to Re_ω^{-1} for $\beta \ll 1$, and proportional to $Re_\omega^{-1/2}$ for $\beta \gg 1$.

Key words: electrohydrodynamic effects, magneto convection

1. Introduction

Magnetic fields have been used to manipulate flows through the motion of suspended magnetic particles. A magnetorheological fluid (Klingenberg 2001; de Vicente, Klingenberg & Hidalgo-Alvarez 2011) consists of micron-sized magnetic particles suspended in a viscous oil. In the absence of a magnetic field, the particles are well dispersed and the fluid flows freely in a conduit. When a magnetic field is applied across

© The Author(s), 2025. Published by Cambridge University Press. This is an Open Access article, distributed under the terms of the Creative Commons Attribution licence (https://creativecommons.org/licenses/by/4.0/), which permits unrestricted re-use, distribution and reproduction, provided the original article is properly cited.

https://doi.org/10.1017/jfm.2025.10176 Published online by Cambridge University Press

the conduit, the particles aggregate and jam the gap, resulting in cessation of flow. The clustering of particles is anisotropic, with elongated chains of particles along the magnetic field direction. The transition between the freely flowing and jammed suspension takes place over time scales of the order of milliseconds, thereby enabling applications in brakes, dampers and mechanical actuators. The rheology is usually described by the Bingham model, and the Bingham number (ratio of yield stress and viscous stress) is a function of the Mason number, the ratio of the magnetic and viscous forces (Klingenberg, Ulicny & Golden 2007). A mechanistic model for the relation between the Bingham and Mason number (Sherman, Becnel & Wereley 2015) is based on the relative magnitudes of the applied shear force and the magnetic force between a pair of particles. This provides a criterion for the stress required for the initiation of flow in the jammed state. The instability of a uniform suspension of magnetic particles subject to shear has been studied (Kumaran 2022) to model the initiation of jamming when a magnetic field is applied. An isolated particle in a uniform magnetic field experiences a torque but no net force. Interparticle hydrodynamic and magnetic interactions result in a diffusive term in the particle concentration equation. The diffusion tensor is anisotropic, and the diffusion coefficient is positive along the magnetic field direction and negative in the two perpendicular directions, leading to the formation of chains that jam the conduit.

A magnetic field has also been used to generate flow in a ferrofluid, which is a suspension of nanometre-sized magnetic particles (Moskowitz & Rosensweig 1967; Zaitsev & Shliomis 1969). These exhibit a curious 'spin-up' phenomenon where the fluid rotates in the direction opposite to the rotation of the magnetic field (Chaves, Zahn & Rinaldi 2008; Rosensweig 2023). In the constitutive relation for these fluids, the stress contains an antisymmetric part or 'couple stress' with a 'spin viscosity' coefficient proportional to the gradient of the local angular vorticity (Stokes 1966; Rosensweig 2000; Rinaldi & Zahn 2002).

There is no net force on a paramagnetic or ferromagnetic particle in a steady or oscillating field, but there is a torque on the particle. Complex behaviour is observed when a particle in a steady magnetic field is subject to shear (Almog & Frankel 1995; Sobecki *et al.* 2018; Kumaran 2021*a*,*b*). In a steady magnetic field in the absence of flow, the particle aligns in the field direction. In a shear flow in the absence of a magnetic field, the orientation of a spheroid undergoes closed orbits called 'Jeffery orbits' (Jeffery 1923; Hinch & Leal 1979), which depend on the initial condition. As the ratio of the magnetic and shear torque is increased, there is a progression from the rotating state to the static state. Different kinds of transitions are observed depending on the aspect ratio of the particle, including multiple steady states and rotating limit cycles (Kumaran 2020*a*).

The dynamics of a magnetic particle in an oscillating magnetic field is found to be critically dependent on the magnetisation model used (Misra & Kumaran 2024*a*). The orientation vector of a permanent dipole undergoes an oscillatory motion between the two poles of the oscillatory magnetic field, whereas non-hysteretic induced dipoles align in the magnetic field direction in the long time limit. The hysteretic Stoner–Wohlfarth model exhibits a transition between an 'oscillating' magnetic moment and a 'rotating' magnetic moment as the field strength is increased. The effect of shear on a spherical dipolar particle has also been studied (Puyesky & Frankel 1998; Misra & Kumaran 2024*b*). This exhibits a transition between rotating and static states in the $\Sigma - \omega$ plane, where Σ is the ratio of the magnetic and hydrodynamic torque, and ω is the ratio of the magnetic field frequency and the strain rate. The boundary between these two states is complex, with features such as Arnold tongues, phase-locking and discontinuous changes in the rotation number.

There have been some studies on the effect of steady and time-dependent magnetic fields on suspended conducting particles (Moffatt 1990; Kumaran 2019, 2020*b*). A particle

https://doi.org/10.1017/jfm.2025.10176 Published online by Cambridge University Press

suspended in a flow is rotated by the shear. Eddy currents are induced in a rotating conductor in a magnetic field. The resultant magnetic moment due to the eddy currents results in a torque on the particle due to the applied magnetic field. This results in an antisymmetric part of the rate of deformation tensor (Batchelor 1970), which is related to the product of the magnetic field and the fluid vorticity at the particle centre. The drag and lift forces on a particle in an oscillating magnetic field have been calculated (Moffatt 1990), and some of these results have been verified in experimental studies (Bolcato *et al.* 1993).

In metal processing, 'electromagnetic stirring' has been used for inducing flow, mixing and homogenising materials and for stabilising interfaces (Moffatt 1991). Magnetic damping has also been used to attenuate fluid motion (Davidson 1999). A time-varying magnetic field induces currents inside the metal in the molten state, and this causes a Lorentz force that generates flow or deforms interfaces. These flows in large scale industrial processes are turbulent, three-dimensional and complex. The fundamental understanding of the effect of time-varying magnetic fields on conducting fluids is now well established (Moffatt 1978). In large scale applications, the depth of penetration of an oscillating magnetic field into a conducting metal is referred to as the 'skin depth' (Landau, Lifshitz & Pitaevskii 2014). The force within this skin layer acts as a tangential velocity or stress boundary condition at the surface of the fluid, and generates flow. The alternating magnetic field creates time-dependent and chaotic flows which mix and stir the molten metal. Computational fluid dynamics has been used to predict flows generated in molten metals by time-varying magnetic fields (Timofeev & Khatsayuk 2016; Shvydkiy, Baake & Koppen 2020).

Here, we examine the prospect of using magnetokinetic forcing for generating flow and mixing in small-scale and microfluidic applications. There have been extensive studies on electrokinetic flows in drops, pioneered by the work of Rayleigh (1882) on rain drops and Taylor (1964, 1966) on water drops subject to electric fields. Models for perfect and leaky dielectrics have been developed (Melcher & Taylor 1969). While these earlier studies predicted that the interfacial stress is perpendicular to the surface and there is deformation without flow, it is now known that flows are generated for drops with finite conductivity (Feng & Scott 1996; Das & Saintillan 2021). Detailed studies of drop coalescence (Mhatre, Deshmukh & Thaokar 2015) and breakup (Karyappa, Deshmukh & Thaokar 2014) have also been carried out. There are no equivalent studies of the effect of magnetic fields on conducting liquids.

The potential to generate flows within metallic drops could be of importance in metallurgical applications, where flows could be used to homogenise or amorphise molten metals before freezing. Another potential application is to enhance mixing and transport in microfluidic systems. While electrokinetic flows have been extensively used (Squires & Bazant 2004), the electromotive force due to an applied electric field is sensitive to the concentration of ions in a solution. Such electromotive forces are not caused by magnetic fields acting on conducting fluids, and so there is likely to be relatively less sensitivity to the ionic composition of the fluid. The flow generated within a spherical drop due to an oscillating magnetic field (Moffatt 1991) induces velocity fluctuations outside the drop. These could be used to enhance mixing and transport. The hydrodynamic interaction with other drops or boundaries could also generate drop motion, which could enhance fluid velocity fluctuations at small scales. The velocity and strain rates that could be generated are estimated in § 5.

The flow within and outside a conducting drop of viscosity η_i suspended in a non-conducting medium of viscosity η_o is calculated in the limit where the nonlinear term in the momentum conservation equation is negligible, and where the capillary number

https://doi.org/10.1017/jfm.2025.10176 Published online by Cambridge University Press

(ratio of stresses due to Lorentz force and surface tension) is small. Both these assumptions are examined in § 5. The flow-induced deformation of the drop in the low capillary number limit is calculated from the velocity field in a spherical drop. It is not assumed that the Reynolds number based on the magnetic field frequency is small. A preliminary calculation of the steady flow for a spherical drop with a zero shear stress boundary condition at the surface is provided in Kumaran (2024).

The derivation of the electric and magnetic fields is given in Appendix A, since the principles used are well known (Landau *et al.* 2014). If the frequency of the magnetic field is ω, the frequency of the induced eddy current is also ω. The Lorentz force density, which is the cross product of the current density and the magnetic field, consists of a steady part and an oscillating part, the latter with frequency 2ω. The steady and oscillating parts of the force density are derived in Appendix B.

The velocity field is derived using the stream function formulation in a spherical coordinate system in § 2. The results for the steady and oscillating parts of the velocity field are presented in § § 3 and 4, respectively. Here, we have used the expressions for the Lorentz force density derived in Appendix B. The velocity, strain rate, stress and the Joule heating that could be generated in practical applications are estimated in § 5. The important results are summarised in § 6.

2. Velocity field

A conducting drop of radius R, density ρ_i, viscosity η_i and electrical conductivity κ is suspended in a fluid with density ρ_o and viscosity η_o. An oscillating magnetic field of amplitude H_0 and angular frequency ω is applied in the $\hat{\boldsymbol{H}}$ direction. The magnetic field far from the drop is

$$\boldsymbol{H}^{\dagger} = H_0\hat{\boldsymbol{H}}\cos(\omega t) = \tfrac{1}{2}H_0\hat{\boldsymbol{H}}(\exp(\imath\omega t^{\dagger}) + \exp(-\imath\omega t^{\dagger})). \tag{2.1}$$

Both the drop and the suspending medium are non-magnetic, so the magnetic permeability is assumed to be that of vacuum, μ_0.

The magnetic and electric fields are determined in Appendix A by solving the Maxwell equations for an uncharged, non-magnetic electrically conducting drop in a non-conducting medium (Landau *et al.* 2014). The oscillating magnetic field induces oscillating eddy currents of frequency ω in the direction perpendicular to the magnetic field, which circulates around the axis of the drop. The nature of the electric and magnetic fields depends on the dimensionless parameter $\beta = \sqrt{\mu_0\kappa\omega R^2}$, which is the square root of the ratio of the magnetic field frequency and the current relaxation rate. This parameter can also be interpreted as the ratio of the drop radius and the 'penetration depth' of the magnetic field $(\mu_0\kappa\omega)^{-1/2}$. For $\beta \ll 1$, the penetration depth is much larger than the drop radius, and there is an oscillating magnetic field throughout the drop. For $\beta \gg 1$, the drop radius is much larger than the penetration depth, and the magnetic field disturbance is restricted to a 'skin layer' of depth $\beta^{-1}R$ at the surface.

The Lorentz force density is the cross product of the current density and the magnetic field. This contains a steady component and an oscillatory component with frequency 2ω. These two components are calculated in Appendix B. These are used in the following sections to determine the velocity field.

The linearised mass and momentum equations for the velocity field are

$$\boldsymbol{\nabla}^{\dagger}\cdot\boldsymbol{v}^{\dagger} = 0, \tag{2.2}$$

https://doi.org/10.1017/jfm.2025.10176 Published online by Cambridge University Press

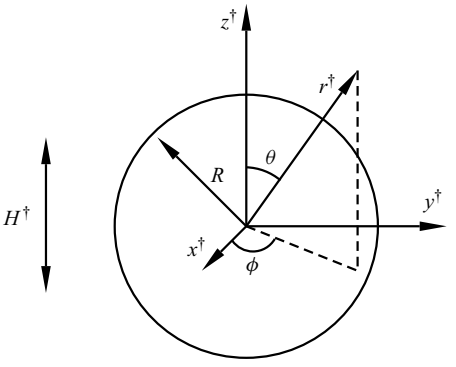


Figure 1. The configuration and coordinate system for analysing the flow in and around a conducting drop of radius R subjected to an oscillating magnetic field $\boldsymbol{H}^\dagger$. The magnetic field is applied along the z (axial) direction.

$$\rho\frac{\partial \boldsymbol{v}^\dagger}{\partial t^\dagger} = -\boldsymbol{\nabla}^\dagger p^\dagger + \eta\boldsymbol{\nabla}^{\dagger 2}\boldsymbol{v}^\dagger + \boldsymbol{f}^\dagger. \tag{2.3}$$

Here, $\boldsymbol{\nabla}^\dagger$ is the gradient operator, $\boldsymbol{v}^\dagger$ is the velocity field, $p^\dagger$ is the pressure field and ρ and η are the fluid density and viscosity. The Lorentz force density $\boldsymbol{f}^\dagger$ is calculated in Appendix B. It should be noted that † is used to denote dimensional variables, while dimensionless variables are expressed without the superscript. In (2.3), the nonlinear convective term has been neglected. The validity of this approximation is examined in § 5.

The pressure is eliminated by taking the curl of the momentum (2.3),

$$\rho\frac{\partial(\boldsymbol{\nabla}^\dagger \times \boldsymbol{v}^\dagger)}{\partial t^\dagger} = \eta\boldsymbol{\nabla}^{\dagger 2}(\boldsymbol{\nabla}^\dagger \times \boldsymbol{v}^\dagger) + \boldsymbol{\nabla}^\dagger \times \boldsymbol{f}^\dagger. \tag{2.4}$$

The incompressibility condition is satisfied by using the stream function formulation for an axisymmetric flow.

The flow is analysed in the spherical coordinate system shown in figure 1 with the z axis along the magnetic field direction. Here, $r^\dagger$ is the distance from the centre of the drop, the azimuthal angle θ is the angle between the position vector and the axial z direction and ϕ is the meridional angle around the axis.

In Appendix B, it is shown that the current density and electric field are in the meridional ϕ direction. Since the Lorentz force density is the cross product of the current density and the magnetic field, the Lorentz force density does not have a component in the ϕ direction. Consequently, the flow is axisymmetric, and the velocity $v_\phi^\dagger$ is zero. The two non-zero components of the velocity are expressed in terms of the stream function $\psi^\dagger$,

$$v_r^\dagger = -\frac{1}{r^{\dagger 2}\sin(\theta)}\frac{\partial\psi^\dagger}{\partial\theta}, \quad v_\theta^\dagger = \frac{1}{r^\dagger\sin(\theta)}\frac{\partial\psi^\dagger}{\partial r^\dagger}. \tag{2.5}$$

The terms in (2.4) are expressed in terms of the stream function using the definitions (2.5) (Happel & Brenner 1983),

$$\boldsymbol{\nabla}^\dagger \times \boldsymbol{v}^\dagger = \frac{\hat{\boldsymbol{e}}_\phi}{r^\dagger\sin(\theta)}\left(\frac{\partial^2}{\partial r^{\dagger 2}} + \frac{\sin(\theta)}{r^{\dagger 2}}\frac{\partial}{\partial\theta}\left(\frac{1}{\sin(\theta)}\frac{\partial}{\partial\theta}\right)\right)\psi^\dagger, \tag{2.6}$$

https://doi.org/10.1017/jfm.2025.10176 Published online by Cambridge University Press

$$\boldsymbol{\nabla}^{\dagger 2}(\boldsymbol{\nabla}^{\dagger} \boldsymbol{\times} \boldsymbol{v}^{\dagger}) = \frac{\hat{\boldsymbol{e}}_\phi}{r^\dagger \sin(\theta)} \left(\frac{\partial^2}{\partial r^{\dagger 2}} + \frac{\sin(\theta)}{r^{\dagger 2}} \frac{\partial}{\partial \theta} \left(\frac{1}{\sin(\theta)} \frac{\partial}{\partial \theta} \right) \right)^2 \psi^\dagger. \tag{2.7}$$

These are substituted into the curl of the momentum (2.4) and multiplied by $r^\dagger \sin(\theta)$. The resulting vector equation has a non-zero component only along the $\hat{\boldsymbol{e}}_\phi$ direction, which is

$$\rho \frac{\partial}{\partial t^\dagger} \left(\frac{\partial^2}{\partial r^{\dagger 2}} + \frac{\sin(\theta)}{r^{\dagger 2}} \frac{\partial}{\partial \theta} \left(\frac{1}{\sin(\theta)} \frac{\partial}{\partial \theta} \right) \right) \psi^\dagger = \eta \left(\frac{\partial^2}{\partial r^{\dagger 2}} + \frac{\sin(\theta)}{r^{\dagger 2}} \frac{\partial}{\partial \theta} \left(\frac{1}{\sin(\theta)} \frac{\partial}{\partial \theta} \right) \right)^2 \psi^\dagger + \sin(\theta) \left(\frac{\partial (r^\dagger f_\theta^\dagger)}{\partial r^\dagger} - \frac{\partial f_r^\dagger}{\partial \theta} \right). \tag{2.8}$$

Here, $f_r^\dagger$ and $f_\theta^\dagger$ are the components of $\boldsymbol{f}^\dagger$ along the $r^\dagger$ and θ directions, respectively.

The electric and magnetic fields are determined in Appendix A, and the Lorentz force density in the momentum equation, (2.8), is calculated in the Appendix B. Here, it is found that the steady and oscillatory components of the Lorentz force density have the form

$$\sin(\theta) \left(\frac{\partial (r^\dagger f_\theta^\dagger)}{\partial r^\dagger} - \frac{\partial f_r^\dagger}{\partial \theta} \right) = \sin(\theta)^2 \cos(\theta) F^\dagger(r^\dagger), \tag{2.9}$$

where $F^\dagger(r^\dagger)$ is only a function of $r^\dagger$. The term $\sin(\theta)^2 \cos(\theta) = 2\mathcal{I}_3(\cos(\theta))$, where $\mathcal{I}_3$ is the third-order Gegenbauer polynomial. The Gegenbauer polynomials are solutions of the equation

$$\sin(\theta) \frac{\mathrm{d}}{\mathrm{d}\theta} \left(\frac{1}{\sin(\theta)} \frac{\mathrm{d}\mathcal{I}_n}{\mathrm{d}\theta} \right) + n(n-1)\mathcal{I}_n = 0, \tag{2.10}$$

for integer n. These form an orthogonal basis set. Since the inhomogeneous term in (2.8) is proportional to $\mathcal{I}_3(\cos(\theta)) = 1/2 \sin(\theta)^2 \cos(\theta)$, the stream function is necessarily of the form

$$\psi^\dagger(r^\dagger, \theta, t^\dagger) = g^\dagger(r^\dagger, t^\dagger) \sin(\theta)^2 \cos(\theta), \tag{2.11}$$

where $g^\dagger$ is independent of θ. This is substituted into (2.6) and (2.7) to obtain

$$\boldsymbol{\nabla}^\dagger \boldsymbol{\times} \boldsymbol{v}^\dagger = \frac{\hat{\boldsymbol{e}}_\phi}{r^\dagger \sin(\theta)} \left(\frac{\partial^2 g^\dagger}{\partial r^{\dagger 2}} - \frac{6 g^\dagger}{r^{\dagger 2}} \right) \sin(\theta)^2 \cos(\theta), \tag{2.12}$$

$$\boldsymbol{\nabla}^{\dagger 2}(\boldsymbol{\nabla}^\dagger \boldsymbol{\times} \boldsymbol{v}^\dagger) = \frac{\hat{\boldsymbol{e}}_\phi}{r^\dagger \sin(\theta)} \left(\frac{\partial^4 g^\dagger}{\partial r^{\dagger 4}} - \frac{12}{r^{\dagger 2}} \frac{\partial^2 g^\dagger}{\partial r^{\dagger 2}} + \frac{24}{r^{\dagger 3}} \frac{\partial g^\dagger}{\partial r^\dagger} \right) \sin(\theta)^2 \cos(\theta). \tag{2.13}$$

These are substituted into the momentum (2.8), and the equation is divided by $\sin(\theta)^2 \cos(\theta)$, to obtain an equation for $g^\dagger$,

$$\rho \frac{\partial}{\partial t^\dagger} \left(\frac{\partial^2 g^\dagger}{\partial r^{\dagger 2}} - \frac{6 g^\dagger}{r^{\dagger 2}} \right) = \eta \left(\frac{\partial^4 g^\dagger}{\partial r^{\dagger 4}} - \frac{12}{r^{\dagger 2}} \frac{\partial^2 g^\dagger}{\partial r^{\dagger 2}} + \frac{24}{r^{\dagger 3}} \frac{\partial g^\dagger}{\partial r^\dagger} \right) + F^\dagger. \tag{2.14}$$

The velocity components are expressed in terms of $g^\dagger$ using (2.5) and (2.11),

$$v_r^\dagger = V_r^\dagger (3\cos(\theta)^2 - 1), \quad v_\theta^\dagger = V_\theta^\dagger \sin(\theta) \cos(\theta), \tag{2.15}$$

https://doi.org/10.1017/jfm.2025.10176 Published online by Cambridge University Press

where $V_r^\dagger$ and $V_\theta^\dagger$ are independent of θ,

$$V_r^\dagger = -\frac{g^\dagger}{r^{\dagger 2}}, \quad V_\theta^\dagger = \frac{1}{r^\dagger}\frac{\partial g^\dagger}{\partial r^\dagger}. \tag{2.16}$$

The pressure is most conveniently determined from the azimuthal momentum equation

$$\rho\frac{\partial v_\theta^\dagger}{\partial t^\dagger} = -\frac{1}{r^\dagger}\frac{\partial p^\dagger}{\partial \theta} + \eta\left(\frac{1}{r^{\dagger 2}}\frac{\partial}{\partial r^\dagger}\left(r^{\dagger 2}\frac{\partial v_\theta^\dagger}{\partial r^\dagger}\right) + \frac{2}{r^{\dagger 2}}\frac{\partial v_r^\dagger}{\partial \theta} + \frac{1}{r^{\dagger 2}\sin(\theta)}\frac{\partial}{\partial \theta}\left(\sin(\theta)\frac{\partial v_\theta^\dagger}{\partial \theta}\right) - \frac{v_\theta^\dagger}{r^{\dagger 2}\sin(\theta)^2}\right) + f_\theta^\dagger. \tag{2.17}$$

In the above equation, all terms containing $v_\theta^\dagger$ are proportional to $\sin(\theta)\cos(\theta)$. In Appendix B, it is shown that $\bar{f}_\theta = 0$ for the steady flow (B10), and $\tilde{f}_\theta = \tilde{F}_\theta(r^\dagger)\sin(\theta)\cos(\theta)$, where $\tilde{F}_\theta$ (B18) is only a function of $r^\dagger$. Therefore, $\sin(\theta)\cos(\theta)$ is a common factor for all the terms in (2.17). The expressions (2.15) and (2.16) are substituted for $v_\theta^\dagger$ into (2.17). The pressure is expressed as

$$p^\dagger = P^\dagger(r^\dagger)(3\cos(\theta)^2 - 1) + \frac{2\gamma}{R}, \tag{2.18}$$

where the first term on the right-hand side is the pressure due to the flow, the second term on the right-hand side is the Laplace pressure in the absence of flow and γ is the surface tension. Here, the pressure is set equal to zero far from the drop, and there is a pressure discontinuity at the surface due to surface tension. Equation (2.18) for the pressure and (2.15) for the velocities are substituted into (2.17), and the resulting equation is divided by $\sin(\theta)\cos(\theta)$, to obtain an equation for $P^\dagger$ which is independent of θ,

$$\begin{aligned}\rho\frac{\partial}{\partial t^\dagger}\left(\frac{1}{r^\dagger}\frac{\partial g^\dagger}{\partial r^\dagger}\right) &= \frac{6P^\dagger}{r^\dagger} + \eta\left(\frac{1}{r^{\dagger 2}}\frac{\partial}{\partial r^\dagger}\left(r^{\dagger 2}\frac{\partial}{\partial r^\dagger}\left(\frac{1}{r^\dagger}\frac{\partial g^\dagger}{\partial r^\dagger}\right)\right) - \frac{6}{r^{\dagger 3}}\frac{\partial g^\dagger}{\partial r^\dagger} + \frac{12 g^\dagger}{r^{\dagger 4}}\right) + F_\theta^\dagger(r) \\ &= \frac{6P^\dagger}{r^\dagger} + \eta\left(\frac{1}{r^\dagger}\frac{\partial^3 g^\dagger}{\partial r^{\dagger 3}} - \frac{6}{r^{\dagger 3}}\frac{\partial g^\dagger}{\partial r^\dagger} + \frac{12 g^\dagger}{r^{\dagger 4}}\right) + F_\theta^\dagger(r^\dagger).\end{aligned} \tag{2.19}$$

The normal and shear components of the fluid stress are

$$\sigma_{rr}^\dagger = -p^\dagger + 2\eta\frac{\partial v_r^\dagger}{\partial r^\dagger} = \Sigma_{rr}^\dagger(3\cos(\theta)^2 - 1) - \frac{2\gamma}{R}, \tag{2.20}$$

$$\sigma_{\theta r}^\dagger = \eta\left(r^\dagger\frac{\partial}{\partial r^\dagger}\left(\frac{v_\theta^\dagger}{r^\dagger}\right) + \frac{1}{r^\dagger}\frac{\partial v_r^\dagger}{\partial \theta}\right) = \Sigma_{\theta r}^\dagger\sin(\theta)\cos(\theta). \tag{2.21}$$

Here, $\Sigma_{rr}^\dagger$ and $\Sigma_{\theta r}^\dagger$ are independent of θ,

$$\begin{aligned}\Sigma_{rr}^\dagger &= -P^\dagger + \eta\left(\frac{4g^\dagger}{r^{\dagger 3}} - \frac{2}{r^{\dagger 2}}\frac{\partial g^\dagger}{\partial r^\dagger}\right), \\ &= \eta\left(\frac{1}{6}\frac{\partial^3 g^\dagger}{\partial r^{\dagger 3}} - \frac{3}{r^{\dagger 2}}\frac{\partial g^\dagger}{\partial r^\dagger} + \frac{6g^\dagger}{r^{\dagger 3}}\right) + \frac{r^\dagger F_\theta^\dagger}{6} - \frac{\rho}{6}\frac{\partial}{\partial t^\dagger}\left(\frac{\partial g^\dagger}{\partial r^\dagger}\right),\end{aligned} \tag{2.22}$$

$$\Sigma_{\theta r}^\dagger = \eta\left(\frac{1}{r^\dagger}\frac{\partial^2 g^\dagger}{\partial r^{\dagger 2}} - \frac{2}{r^{\dagger 2}}\frac{\partial g^\dagger}{\partial r^\dagger} + \frac{6g^\dagger}{r^{\dagger 3}}\right). \tag{2.23}$$

https://doi.org/10.1017/jfm.2025.10176 Published online by Cambridge University Press

The last term on the right-hand side in (2.20) is the Laplace pressure difference across the interface due to surface tension.

It should be noted that (2.20)–(2.23) are the fluid stresses; these do not include the Maxwell stress due to the magnetic field. The Maxwell stress is expressed as $\boldsymbol{\sigma}^\dagger = \mu_0(\boldsymbol{H}^\dagger\boldsymbol{H}^\dagger - 1/2\boldsymbol{I}(\boldsymbol{H}^\dagger \cdot \boldsymbol{H}^\dagger))$, where $\boldsymbol{I}$ is the isotropic tensor. The divergence of this stress is the Lorentz body force density that is incorporated in the momentum equation. Since the magnetic field is continuous across the interface (it is assumed the magnetic permeability of the inner and outer fluids are equal), the Maxwell stress is the same in both fluids at the interface. Therefore, there is no net contribution to the interfacial stress balance condition due to the Maxwell stress.

The boundary conditions at the interface are the continuity of velocity and the continuity of stress. Since the surface tension is considered sufficiently high that the drop is non-deformable, the radial velocity at the surface is zero. We use superscripts $^{(i)}$ and $^{(o)}$ to denote the fields within and outside the drop, respectively. The zero normal velocity condition at the interface is $v_r^\dagger = 0$ at $r^\dagger = R$ both within and outside the drop. This is expressed in terms of $g^\dagger$ using (2.15) and (2.16),

$$g^{(i)\dagger} = g^{(o)\dagger} = 0 \quad \text{at} \quad r^\dagger = R. \tag{2.24}$$

The tangential velocity continuity condition at the interface is $v_\theta^{(i)\dagger} = v_\theta^{(o)\dagger}$ at $r^\dagger = R$. This is expressed using (2.15) and (2.16),

$$\frac{\partial g^{(i)\dagger}}{\partial r^\dagger} = \frac{\partial g^{(o)\dagger}}{\partial r^\dagger} \quad \text{at} \quad r^\dagger = R. \tag{2.25}$$

The tangential stress continuity condition is $\sigma_{\theta r}^{(i)\dagger} = \sigma_{\theta r}^{(o)\dagger}$ at $r^\dagger = R$. Using (2.21) and (2.23), and recognising that $g^\dagger$ is zero at the interface from (2.24), we obtain

$$\frac{\partial^2 g^{(i)\dagger}}{\partial r^{\dagger 2}} - \frac{2}{R}\frac{\partial g^{(i)\dagger}}{\partial r^\dagger} = \eta_r\left(\frac{\partial^2 g^{(o)\dagger}}{\partial r^{\dagger 2}} - \frac{2}{R}\frac{\partial g^{(o)\dagger}}{\partial r^\dagger}\right) \quad \text{at} \quad r^\dagger = R. \tag{2.26}$$

Here, $\eta_r = (\eta_o/\eta_i)$ is the ratio of viscosities of the fluids outside and inside the drop.

The boundary condition at the centre of the drop $r^\dagger = 0$ are the symmetry conditions $v_r^{(i)\dagger} = 0$ and $v_\theta^{(i)\dagger} = 0$, which are expressed in terms of $g^{(i)\dagger}$ using (2.15) and (2.16),

$$\frac{g^{(i)\dagger}}{r^{\dagger 2}} \to 0 \quad \text{and} \quad \frac{1}{r^\dagger}\frac{\partial g^{(i)\dagger}}{\partial r^\dagger} \to 0 \quad \text{for} \quad r^\dagger \to 0. \tag{2.27}$$

The boundary condition far from the drop is also the zero-velocity condition,

$$\frac{g^{(o)\dagger}}{r^{\dagger 2}} \to 0 \quad \text{and} \quad \frac{1}{r^\dagger}\frac{\partial g^{(o)\dagger}}{\partial r^\dagger} \to 0 \quad \text{for} \quad r^\dagger \to \infty. \tag{2.28}$$

The non-dimensionalisation scheme is as follows.

(i) All lengths are scaled by the drop radius R.
(ii) The scaled time is defined as $t = \omega t^\dagger$, were ω is the frequency of the magnetic field oscillations.
(iii) The non-dimensional parameter $\beta = \sqrt{\omega\mu_0\kappa R^2}$ is the square root of the ratio of the frequency of oscillations and the relaxation rate of the eddy currents.
(iv) The magnetic field $\boldsymbol{H}^\dagger$ is non-dimensionalised by the amplitude of the applied magnetic field, H_0, so $\boldsymbol{H} = (\boldsymbol{H}^\dagger/H_0)$.

https://doi.org/10.1017/jfm.2025.10176 Published online by Cambridge University Press

Quantity	Dimensional	Scale factor	Scaled
Distance from origin	$r^\dagger$	R	r
Position vector	$\boldsymbol{x}^\dagger$	R	$\boldsymbol{x}$
Time	$t^\dagger$	ω^{-1}	t
Magnetic field	$\boldsymbol{H}^\dagger$, $\tilde{\boldsymbol{H}}^\dagger$	H_0	$\boldsymbol{H}$, $\tilde{\boldsymbol{H}}$
Current density	$\boldsymbol{J}^\dagger$, $\tilde{\boldsymbol{J}}^\dagger$	(H_0/R)	$\boldsymbol{J}$, $\tilde{\boldsymbol{J}}$
Electric field	$\boldsymbol{E}^\dagger$, $\tilde{\boldsymbol{E}}^\dagger$	$(H_0/R\kappa)$	$\boldsymbol{E}$, $\tilde{\boldsymbol{E}}$
Lorentz force density	$\boldsymbol{f}^\dagger$, $\bar{\boldsymbol{f}}^\dagger$, $\tilde{\boldsymbol{f}}^\dagger$	$(\mu_0 H_0^2/R)$	$\boldsymbol{f}$, $\bar{\boldsymbol{f}}$, $\tilde{\boldsymbol{f}}$
Fluid velocity	$\bar{\boldsymbol{v}}^{(i)\dagger}$, $\bar{\boldsymbol{v}}^{(o)\dagger}$, $\tilde{\boldsymbol{v}}^{(i)\dagger}$, $\tilde{\boldsymbol{v}}^{(o)\dagger}$	$(\mu_0 H_0^2 R/\eta_i)$	$\bar{\boldsymbol{v}}^{(i)}$, $\bar{\boldsymbol{v}}^{(o)}$, $\tilde{\boldsymbol{v}}^{(i)}$, $\tilde{\boldsymbol{v}}^{(o)}$
Stream function	$\bar{\psi}^{(o)\dagger}$, $\bar{\psi}^{(i)\dagger}$, $\tilde{\psi}^{(o)\dagger}$, $\tilde{\psi}^{(i)\dagger}$	$(\mu_0 H_0^2 R^3/\eta_i)$	$\bar{\psi}^{(o)}$, $\bar{\psi}^{(i)}$, $\tilde{\psi}^{(o)}$, $\tilde{\psi}^{(i)}$
Stress	$\boldsymbol{\sigma}^\dagger$, $\bar{\boldsymbol{\sigma}}^\dagger$, $\tilde{\boldsymbol{\sigma}}^\dagger$	$(\mu_0 H_0^2)$	$\boldsymbol{\sigma}$, $\bar{\boldsymbol{\sigma}}$, $\tilde{\boldsymbol{\sigma}}$

Table 1. The symbols for the dimensional and scaled quantities and the scale factors. Here, R is the drop radius, H_0 is the amplitude of the applied magnetic field, κ is the electrical conductivity, μ_0 is the permittivity of free space and η_i is the viscosity of the fluid in the drop.

(v) The scaling for the current density $\boldsymbol{J}^\dagger$ is determined from Ampere's circuital law, $\boldsymbol{\nabla}^\dagger \times \boldsymbol{H}^\dagger = \boldsymbol{J}^\dagger + \epsilon(\partial \boldsymbol{E}^\dagger/\partial t^\dagger)$. The second term on the right-hand side is neglected in comparison with the first in Ampere's circuital law for a conducting drop, and the scaled current density is $\boldsymbol{J} = \boldsymbol{J}^\dagger/(H_0/R)$.

(vi) The electric field is determined by Ohm's law, $\boldsymbol{J}^\dagger = \kappa \boldsymbol{E}^\dagger$, and the scaling for the electric field is $\boldsymbol{E} = \boldsymbol{E}^\dagger/(H_0/R\kappa)$.

(vii) The force density is given by the Lorentz force law for a fluid without free charges, $\boldsymbol{f}^\dagger = \mu_0(\boldsymbol{J}^\dagger \times \boldsymbol{H}^\dagger)$. Therefore, the scaling for the force density is $\boldsymbol{f} = \boldsymbol{f}^\dagger/(\mu_0 H_0^2/R)$.

(viii) The scaling for the velocity is obtained by balancing the viscous term in the momentum equation within the drop, $\eta_i \boldsymbol{\nabla}^{\dagger 2}\boldsymbol{v}^\dagger$, and the force density $\boldsymbol{f}^\dagger$. This provides the scaling for the velocity, $\boldsymbol{v} = \boldsymbol{v}^\dagger/(\mu_0 H_0^2 R/\eta_i)$.

(ix) From (2.5), the non-dimensionalised stream function is $\psi = \psi^\dagger/(\mu_0 H_0^2 R^3/\eta_i)$.

(x) The viscous stress within the drop is $\eta_i(\boldsymbol{\nabla}\boldsymbol{v}^\dagger + (\boldsymbol{\nabla}\boldsymbol{v}^\dagger)^{\mathrm{T}})$, where the superscript $^{\mathrm{T}}$ denotes the transpose. Therefore, the scaled stress is $\boldsymbol{\sigma} = \boldsymbol{\sigma}^\dagger/(\mu_0 H_0^2)$.

The symbols for the dimensional and dimensionless variables are collated in table 1. In this table, there are symbols with two different accents. The symbols with overbars, $\bar{\star}$, are steady components of the quantities that are independent of time, which are real. The symbols with tildes, $\tilde{\star}$, are related to the oscillating components of quantities which are complex. The physical magnetic and electric fields are defined as $\star = 1/2(\tilde{\star}\exp(\imath t) + \tilde{\star}^*\exp(-\imath t))$, and the physical flow quantities are defined as $\star = \bar{\star} + 1/2(\tilde{\star}\exp(2\imath t) + \tilde{\star}^*\exp(-2\imath t))$. All quantities are expressed in dimensionless form in the following analysis.

The inhomogeneous term $F(r)$ in the momentum (2.14), due to the Lorentz force density, is calculated in Appendix B. This is expressed as the sum of a steady and an oscillating part,

$$F(r,t) = \bar{F}(r) + \tfrac{1}{2}(\tilde{F}(r)\exp(2\imath t) + \tilde{F}^*(r)\exp(-2\imath t)). \tag{2.29}$$

https://doi.org/10.1017/jfm.2025.10176 Published online by Cambridge University Press

Since the relation (2.14) is linear, the function g is also expressed as

$$g(r,t) = \bar{g}(r) + \tfrac{1}{2}(\tilde{g}(r)\exp(2\imath t) + \tilde{g}^*(r)\exp(-2\imath t)). \tag{2.30}$$

Equation (2.14) is solved separately within and outside the drop, and the velocity and stress boundary conditions at the interface are used to determine the constants in the solution.

The drop deformation and oscillation is estimated in the limit where the capillary number is small, that is, the surface tension forces are much larger than the forces generated by flow. The flow field is calculated assuming the drop is spherical. This flow field is then used to calculate the deformation of the surface. The surface shape is assumed to be of the form

$$r = 1 + h(\theta, t), \tag{2.31}$$

where $h(\theta)$, the surface displacement, scales as Ca, the capillary number. From (2.20) and (2.22), it is evident that the normal stress is of the form $\Sigma_{rr}(3\cos(\theta)^2 - 1)$, where Σ_{rr} is only a function of the radius. (There is, of course, an isotropic radial pressure difference across the interface due to the Laplace pressure, which is the last term on the right-hand side of (2.20).) Therefore, the surface displacement is also expressed as

$$h(\theta,t) = h_0(t)(3\cos(\theta)^2 - 1). \tag{2.32}$$

The function $h_0(t)$ is expressed as the sum of a steady and an oscillating part,

$$h_0 = \bar{h}_0 + \tfrac{1}{2}(\tilde{h}_0\exp(2\imath t) + \tilde{h}_0^*\exp(-2\imath t)). \tag{2.33}$$

The parameters $\bar{h}_0$ and $\tilde{h}_0$ are evaluated from the normal stress balance at $r = 1$.

2.1. *Steady component of flow*

The equation for the steady component of the velocity within the drop is determined by setting the time derivative equal to zero in (2.14),

$$\frac{\mathrm{d}^4\bar{g}^{(i)}}{\mathrm{d}r^4} - \frac{12}{r^2}\frac{\mathrm{d}^2\bar{g}^{(i)}}{\mathrm{d}r^2} + \frac{24}{r^3}\frac{\mathrm{d}\bar{g}^{(i)}}{\mathrm{d}r} + \bar{F} = 0. \tag{2.34}$$

Since there is no Lorentz force outside the drop, the scaled equation for $\bar{g}^{(o)}$ is

$$\frac{\mathrm{d}^4\bar{g}^{(o)}}{\mathrm{d}r^4} - \frac{12}{r^2}\frac{\mathrm{d}^2\bar{g}^{(o)}}{\mathrm{d}r^2} + \frac{24}{r^3}\frac{\mathrm{d}\bar{g}^{(o)}}{\mathrm{d}r} = 0. \tag{2.35}$$

Equation (2.35) for the flow outside the drop is solved subject to the boundary conditions (2.28) for $r \to \infty$ and (2.24) for $r = 1$ to obtain the solution

$$\bar{g}^{(o)} = C\left(1 - \frac{1}{r^2}\right), \tag{2.36}$$

where C is a constant of integration. The velocity components are

$$\bar{v}_r = \frac{C(1-r^2)(3\cos(\theta)^2 - 1)}{r^4}, \tag{2.37}$$

$$\bar{v}_\theta = \frac{2C\sin(\theta)\cos(\theta)}{r^4}. \tag{2.38}$$

The constant C is determined from the condition for the tangential velocity (2.15) at the surface,

$$C = \tfrac{1}{2}\ \bar{V}_\theta\big|_{r=1}. \tag{2.39}$$

https://doi.org/10.1017/jfm.2025.10176 Published online by Cambridge University Press

The tangential stress boundary condition, (2.26), is divided by $(\mathrm{d}\bar{g}^{(o)}/\mathrm{d}r)$, which is equal to $(\mathrm{d}\bar{g}^{(i)}/\mathrm{d}r)$ from the tangential velocity boundary condition (2.25),

$$\frac{\mathrm{d}^2\bar{g}^{(i)}}{\mathrm{d}r^2}\left(\frac{\mathrm{d}\bar{g}^{(i)}}{\mathrm{d}r}\right)^{-1} - 2 = \eta_r\left(\frac{\mathrm{d}^2\bar{g}^{(o)}}{\mathrm{d}r^2}\left(\frac{\mathrm{d}\bar{g}^{(o)}}{\mathrm{d}r}\right)^{-1} - 2\right) \quad \text{at} \quad r^\dagger = 1. \tag{2.40}$$

Substituting the solution (2.36) for $\bar{g}^{(o)}$ in (2.40), the tangential velocity boundary condition reduces to

$$\frac{\mathrm{d}^2\bar{g}^{(i)}}{\mathrm{d}r^2}\left(\frac{\mathrm{d}\bar{g}^{(i)}}{\mathrm{d}r}\right)^{-1} = 2 - 5\eta_r \quad \text{at} \quad r^\dagger = 1. \tag{2.41}$$

Equation (2.34) is solved for $\bar{g}^{(i)}$ subject to the boundary conditions (2.27) for $r \to 0$ and the conditions (2.24) and (2.41) at $r = 1$.

The normal stress at the surface is given by (2.20) and (2.22). Here, $\bar{F}_\theta = 0$ because the steady component of the body force is in the radial direction. The time derivative on the right-hand side of (2.22) is also zero. Inside the drop, the solution of (2.34) is substituted into (2.20) and (2.22) to obtain

$$\bar{\sigma}_{rr}^{(i)} = \left(\frac{1}{6}\frac{\partial^3\bar{g}^{(i)}}{\partial r^3} - \frac{3}{r^2}\frac{\partial\bar{g}^{(i)}}{\partial r} + \frac{6\bar{g}^{(i)}}{r^3}\right)(3\cos(\theta)^2 - 1) - 2Ca^{-1}. \tag{2.42}$$

Here, $Ca = (\mu_0 H_0^2 R/\gamma)$ is the capillary number, and the last term on the right-hand side in (2.42) is the result of the non-dimensionalisation of the last term on the right-hand side in (2.20). At the surface $r = 1$, $\bar{g}^{(i)} = 0$, and the normal stress is

$$\bar{\sigma}_{rr}^{(i)}\Big|_{r=1} = \left(\frac{1}{6}\frac{\partial^3\bar{g}^{(i)}}{\partial r^3} - 3\frac{\partial\bar{g}^{(i)}}{\partial r}\right)(3\cos(\theta)^2 - 1) - 2Ca^{-1}. \tag{2.43}$$

The normal stress outside the drop is determined using the solutions (2.38) and (2.39) for $\bar{g}^{(o)}$,

$$\bar{\sigma}_{rr}^{(o)} = \eta_r\ \bar{V}_\theta\big|_{r=1}\left(\frac{3}{r^3} - \frac{4}{r^5}\right)(3\cos(\theta)^2 - 1). \tag{2.44}$$

At the surface $r = 1$, the normal stress is

$$\bar{\sigma}_{rr}^{(o)}\Big|_{r=1} = -\eta_r\ \bar{V}_\theta\big|_{r=1}(3\cos(\theta)^2 - 1). \tag{2.45}$$

The normal stress balance at the drop surface $r = 1$ is

$$\begin{aligned}\bar{\sigma}_{rr}^{(i)}\Big|_{r=1} - \bar{\sigma}_{rr}^{(o)}\Big|_{r=1} &= -2Ca^{-1} - 2Ca^{-1}\nabla_s^2\bar{h}(\theta)\\ &= -2Ca^{-1} + 6Ca^{-1}\bar{h}_0(3\cos(\theta)^2 - 1),\end{aligned} \tag{2.46}$$

where ∇_s is the Laplacian along the spherical surface $r = 1$. The expressions (2.43) and (2.45) are substituted into (2.46). The first term on the right-hand side in (2.46) cancels the last term on the right-hand side in (2.43) for $\bar{\sigma}_{rr}^{(i)}$, and the resulting equation is divided by $(3\cos(\theta)^2 - 1)$ to determine $\bar{h}_0$. Since the left-hand side of (2.46) is independent of the capillary number, it is evident that $\bar{h}_0$ is proportional to the capillary number in the limit $Ca \ll 1$ considered here.

https://doi.org/10.1017/jfm.2025.10176 Published online by Cambridge University Press

2.2. *Oscillatory component of flow*

The oscillatory component of the forcing in (2.29) and the function g in (2.30) are substituted into the momentum balance (2.14). The coefficient of $\exp(2\imath t)$ in the resulting equation is

$$\frac{\mathrm{d}^4\tilde{g}^{(i)}}{\mathrm{d}r^4} - \frac{12}{r^2}\frac{\mathrm{d}^2\tilde{g}^{(i)}}{\mathrm{d}r^2} + \frac{24}{r^3}\frac{\mathrm{d}\tilde{g}^{(i)}}{\mathrm{d}r} - \tilde{\alpha}^2\left(\frac{\mathrm{d}^2\tilde{g}^{(i)}}{\mathrm{d}r^2} - \frac{6\tilde{g}^{(i)}}{r^2}\right) + \tilde{F} = 0, \tag{2.47}$$

where the complex parameter $\tilde{\alpha}$ is proportional to the square root of the Reynolds number, $Re_\omega = (\rho_i \omega R^2/\eta_i)$, based on the frequency of oscillations and the density and viscosity of the fluid within the drop,

$$\tilde{\alpha} = \sqrt{2\imath\rho_i\omega R^2/\eta_i} = \sqrt{2\imath\, Re_\omega}. \tag{2.48}$$

There is no forcing for the flow outside the drop, and the equivalent of (2.47) is

$$\frac{\mathrm{d}^4\tilde{g}^{(o)}}{\mathrm{d}r^4} - \frac{12}{r^2}\frac{\mathrm{d}^2\tilde{g}^{(o)}}{\mathrm{d}r^2} + \frac{24}{r^3}\frac{\mathrm{d}\tilde{g}^{(o)}}{\mathrm{d}r} - \tilde{\alpha}_o^2\left(\frac{\mathrm{d}^2\tilde{g}^{(o)}}{\mathrm{d}r^2} - \frac{6\tilde{g}^{(o)}}{r^2}\right) = 0, \tag{2.49}$$

where

$$\tilde{\alpha}_o = \sqrt{2\imath\rho_o\omega R^2/\eta_o} = \sqrt{2\imath\, Re_\omega^{(o)}}. \tag{2.50}$$

Equation (2.49) for $\tilde{g}^{(o)}$ can be solved analytically,

$$\begin{aligned}\tilde{g}^{(o)} = {} & \frac{D_1}{r^2} + D_2 r^3 + D_3 \exp(\tilde{\alpha}_o r)\left(1 - 3(\tilde{\alpha}_o r)^{-1} + 3(\tilde{\alpha}_o r)^{-2}\right) \\ & + D_4 \exp(-\tilde{\alpha}_o r)\left(1 + 3(\tilde{\alpha}_o r)^{-1} + 3(\tilde{\alpha}_o r)^{-2}\right).\end{aligned} \tag{2.51}$$

The constants D_2 and D_3 are zero due to the condition (2.28) that the velocity tends to zero for $r \to \infty$. A relation between D_1 and D_4 is obtained from the zero normal velocity condition (2.24) at $r = 1$, and the equation for the stream function is

$$\tilde{g}^{(o)} = \frac{6D}{\tilde{\alpha}_o^2}\left(\frac{1}{r^2} - \exp(-\tilde{\alpha}_o(r-1))\left(\frac{1 + 3(\tilde{\alpha}_o r)^{-1} + 3(\tilde{\alpha}_o r)^{-2}}{1 + 3\tilde{\alpha}_o^{-1} + 3\tilde{\alpha}_o^{-2}}\right)\right). \tag{2.52}$$

The boundary condition (2.26) is simplified using the above solution for $\tilde{g}^{(o)}$. If we divide the right- and left-hand sides of (2.26) by $(\mathrm{d}\tilde{g}^{(o)}/\mathrm{d}r)\big|_{r=1}$, which is equal to $(\mathrm{d}\tilde{g}^{(i)}/\mathrm{d}r)\big|_{r=1}$ (boundary condition (2.25)), we obtain

$$\frac{\mathrm{d}^2\tilde{g}^{(i)}}{\mathrm{d}r^2}\left(\frac{\mathrm{d}\tilde{g}^{(i)}}{\mathrm{d}r}\right)^{-1} = 2(1-\eta_r) + \eta_r\frac{\mathrm{d}^2\tilde{g}^{(o)}}{\mathrm{d}r^2}\left(\frac{\mathrm{d}\tilde{g}^{(o)}}{\mathrm{d}r}\right)^{-1} \quad \text{at } r = 1. \tag{2.53}$$

The right-hand side of the above boundary condition is evaluated using the solution (2.52),

$$\frac{\mathrm{d}^2\tilde{g}^{(i)}}{\mathrm{d}r^2}\left(\frac{\mathrm{d}\tilde{g}^{(i)}}{\mathrm{d}r}\right)^{-1} = 2(1-\eta_r) - \eta_r\left(\frac{3 + 3\tilde{\alpha}_o + \tilde{\alpha}_o^2}{1 + \tilde{\alpha}_o}\right) \quad \text{at } r = 1. \tag{2.54}$$

Equation (2.47) is solved for $\tilde{g}^{(i)}$ subject to the boundary conditions (2.24) and (2.54) at $r = 1$ and the conditions (2.27) for $r \to 0$.

The shear and normal stresses are simplified using the same procedure as that used in (2.42)–(2.46) for a steady flow, but with the important difference that the inertial term

https://doi.org/10.1017/jfm.2025.10176 Published online by Cambridge University Press

on the momentum equation is $(\tilde{\alpha}^2/r)(\partial \tilde{g}/\partial r)\sin(\theta)^2\cos(\theta)$ in dimensionless form. The oscillatory component of the pressure is expressed as

$$\tilde{p}^{(i)} = \tilde{P}^{(i)}(r)(3\cos(\theta)^2 - 1). \tag{2.55}$$

This is substituted into the θ momentum balance to obtain the oscillating component of (2.19),

$$\frac{\tilde{\alpha}^2}{r}\frac{\mathrm{d}\tilde{g}^{(i)}}{\mathrm{d}r} = \frac{6\tilde{P}^{(i)}}{r} + \frac{1}{r}\frac{\mathrm{d}^3\tilde{g}^{(i)}}{\mathrm{d}r^3} - \frac{6}{r^3}\frac{\mathrm{d}\tilde{g}^{(i)}}{\mathrm{d}r} + \frac{12\tilde{g}^{(i)}}{r^4} + \tilde{F}_\theta(r). \tag{2.56}$$

The oscillatory components (coefficients of $\exp(2\imath t)$) in the expressions for the tangential and normal stresses are

$$\tilde{\sigma}_{rr}^{(i)} = -\tilde{p}^{(i)} + 2\frac{\partial \tilde{v}_r^{(i)}}{\partial r} = \tilde{\Sigma}_{rr}^{(i)}(3\cos(\theta)^2 - 1), \tag{2.57}$$

$$\tilde{\sigma}_{\theta r}^{(i)} = \left(r\frac{\partial}{\partial r}\left(\frac{\tilde{v}_\theta^{(i)}}{r}\right) + \frac{1}{r}\frac{\partial \tilde{v}_r^{(i)}}{\partial \theta}\right) = \tilde{\Sigma}_{\theta r}^{(i)}\sin(\theta)\cos(\theta), \tag{2.58}$$

where, $\tilde{\Sigma}_{rr}^{(i)}$ and $\tilde{\Sigma}_{\theta r}^{(i)}$ are

$$\begin{aligned}\tilde{\Sigma}_{rr}^{(i)} &= -\tilde{P}^{(i)} + \left(\frac{4\tilde{g}^{(i)}}{r^3} - \frac{2}{r^2}\frac{\mathrm{d}\tilde{g}^{(i)}}{\partial r}\right),\\ &= \frac{1}{6}\frac{\mathrm{d}^3\tilde{g}^{(i)}}{\mathrm{d}r^3} - \frac{3}{r^2}\frac{\mathrm{d}\tilde{g}^{(i)}}{\mathrm{d}r} + \frac{6\tilde{g}^{(i)}}{r^3} + \frac{r\tilde{F}_\theta}{6} - \frac{\tilde{\alpha}^2}{6}\frac{\mathrm{d}\tilde{g}^{(i)}}{\mathrm{d}r},\end{aligned} \tag{2.59}$$

$$\tilde{\Sigma}_{\theta r}^{(i)} = \left(\frac{1}{r}\frac{\mathrm{d}^2\tilde{g}^{(i)}}{\mathrm{d}r^2} - \frac{2}{r^2}\frac{\mathrm{d}\tilde{g}^{(i)}}{\mathrm{d}r} + \frac{6\tilde{g}^{(i)}}{r^3}\right). \tag{2.60}$$

The stresses outside the drop are calculated from $\tilde{g}^{(o)}$ (2.52), in a similar manner. The pressure is expressed as

$$\tilde{p}^{(o)} = \tilde{P}^{(o)}\big(3\cos(\theta)^2 - 1\big). \tag{2.61}$$

The pressure is determined from the θ momentum equation, resulting in an equation similar to (2.56) but without the forcing term,

$$\frac{\eta_r\tilde{\alpha}_o^2}{r}\frac{\mathrm{d}\tilde{g}^{(o)}}{\mathrm{d}r} = \frac{6\tilde{P}^{(o)}}{r} + \eta_r\left(\frac{1}{r}\frac{\mathrm{d}^3\tilde{g}^{(o)}}{\mathrm{d}r^3} - \frac{6}{r^3}\frac{\mathrm{d}\tilde{g}^{(o)}}{\mathrm{d}r} + \frac{12\tilde{g}^{(o)}}{r^4}\right). \tag{2.62}$$

Here, the factors η_r on the left- and right-hand sides of the equation result from the use of the viscosity of the inner fluid, η_i, for non-dimensionalisation. The shear and normal stresses, equivalent to (2.57)–(2.60), are

$$\tilde{\sigma}_{rr}^{(o)} = -\tilde{p}^{(o)} + 2\eta_r\frac{\partial \tilde{v}_r^{(o)}}{\partial r} = \tilde{\Sigma}_{rr}^{(o)}(3\cos(\theta)^2 - 1), \tag{2.63}$$

$$\tilde{\sigma}_{\theta r}^{(o)} = \eta_r\left(r\frac{\partial}{\partial r}\left(\frac{\tilde{v}_\theta^{(o)}}{r}\right) + \frac{1}{r}\frac{\partial \tilde{v}_r^{(o)}}{\partial \theta}\right) = \tilde{\Sigma}_{\theta r}^{(o)}\sin(\theta)\cos(\theta), \tag{2.64}$$

where, $\tilde{\Sigma}_{rr}^{(o)}$ and $\tilde{\Sigma}_{\theta r}^{(o)}$ are

$$\tilde{\Sigma}_{rr}^{(o)} = \eta_r\left(\frac{1}{6}\frac{\mathrm{d}^3\tilde{g}^{(o)}}{\mathrm{d}r^3} - \frac{3}{r^2}\frac{\mathrm{d}\tilde{g}^{(o)}}{\mathrm{d}r} + \frac{6\tilde{g}^{(o)}}{r^3}\right) - \frac{\eta_r\tilde{\alpha}_o^2}{6}\frac{\mathrm{d}\tilde{g}^{(o)}}{\mathrm{d}r}, \tag{2.65}$$

https://doi.org/10.1017/jfm.2025.10176 Published online by Cambridge University Press

$$\tilde{\Sigma}^{(o)}_{\theta r} = \eta_r \left(\frac{1}{r} \frac{\mathrm{d}^2 \tilde{g}^{(o)}}{\mathrm{d}r^2} - \frac{2}{r^2} \frac{\mathrm{d}\tilde{g}^{(o)}}{\mathrm{d}r} + \frac{6\tilde{g}^{(o)}}{r^3} \right). \tag{2.66}$$

The oscillatory response of the surface deformation is defined by the parameter $\tilde{h}_0$ (2.31)–(2.33). This is determined from the oscillatory component of the normal stress equation, which is the analogue of (2.46) for the steady displacement,

$$\tilde{\sigma}^{(i)}_{rr}\Big|_{r=1} - \tilde{\sigma}^{(o)}_{rr}\Big|_{r=1} = 6Ca^{-1}\tilde{h}_0(3\cos(\theta)^2 - 1), \tag{2.67}$$

where (2.57) and (2.63) are substituted for $\tilde{\sigma}^{(i)}_{rr}$ and $\tilde{\sigma}^{(o)}_{rr}$.

3. Steady component of velocity field

The fourth-order ordinary differential (2.34) for $\bar{g}^{(i)}$ is solved with $\bar{F}$ given by (B12), and subject to the boundary conditions (2.24) and (2.41) at $r = 1$ and (2.27) for $r \to 0$.

3.1. *Flow outside the drop*

The velocity components outside the drop are given by (2.37) and (2.38), with the constant C given by (2.39). This is a biaxial extensional flow, where there is extension along the equatorial $x-y$ plane and compression along the z axis. Consider a flow driven by the rate of deformation tensor of the form

$$\bar{G} = \begin{pmatrix} \hat{\boldsymbol{e}}_x & \hat{\boldsymbol{e}}_y & \hat{\boldsymbol{e}}_z \end{pmatrix} \begin{pmatrix} \frac{1}{2} & 0 & 0 \\ 0 & \frac{1}{2} & 0 \\ 0 & 0 & -1 \end{pmatrix} \begin{pmatrix} \hat{\boldsymbol{e}}_x \\ \hat{\boldsymbol{e}}_y \\ \hat{\boldsymbol{e}}_z \end{pmatrix}. \tag{3.1}$$

In Stokes flow, the general expression for the velocity and pressure fields in indicial notation are

$$\bar{v}_i = C_1 G_{ij} \Phi^{(1)}_j + C_2 G_{jk} \Phi^{(3)}_{ijk} + \frac{p x_i}{2\eta}, \tag{3.2}$$

$$\bar{p} = 2\eta C_3 G_{jk} \Phi^{(2)}_{jk}, \tag{3.3}$$

where each index represents a vector direction, and a repeated index implies a dot product. Here, C_1, C_2 and C_3 are constants, $\Phi^{(1)}_i$, $\Phi^{(2)}_{ij}$ and $\Phi^{(3)}_{ijk}$ are the solutions of the Laplace equation in spherical coordinates,

$$\Phi^{(1)}_i = \frac{\partial}{\partial x_i}\left(\frac{1}{r}\right) = -\frac{x_i}{r^3}, \quad \Phi^{(2)}_{ij} = \frac{\partial}{\partial x_i}\frac{\partial}{\partial x_j}\left(\frac{1}{r}\right) = \frac{3x_i x_j}{r^5} - \frac{\delta_{ij}}{r^3},$$
$$\Phi^{(3)}_{ijk} = \frac{\partial}{\partial x_i}\frac{\partial}{\partial x_j}\frac{\partial}{\partial x_k}\left(\frac{1}{r}\right) = \frac{3\delta_{ij}x_k}{r^5} + \frac{3\delta_{jk}x_i}{r^5} + \frac{3\delta_{ik}x_j}{r^5} - \frac{15x_i x_j x_k}{r^7}. \tag{3.4}$$

Here, δ_{ij} is the Kronecker delta. The velocity field is incompressible only if $C_1 = 0$ in (3.2). The zero normal velocity boundary condition at the surface implies that

$$v_i n_i = v_i x_i = 0 \text{ at } r = 1, \tag{3.5}$$

where $\boldsymbol{n} = \boldsymbol{x}$ is the unit vector at the surface $r = 1$. The zero normal velocity condition provides a relation between the constants C_2 and C_3,

$$C_2 G_{jk} x_i \Phi^{(3)}_{ijk} + C_3 x_i^2 G_{jk} \Phi^{(2)}_{jk} = 0 \text{ at } r = 1. \tag{3.6}$$

This is solved to obtain $C_3 = 3C_2$, and the velocity field is a function of one constant C_2.

https://doi.org/10.1017/jfm.2025.10176 Published online by Cambridge University Press

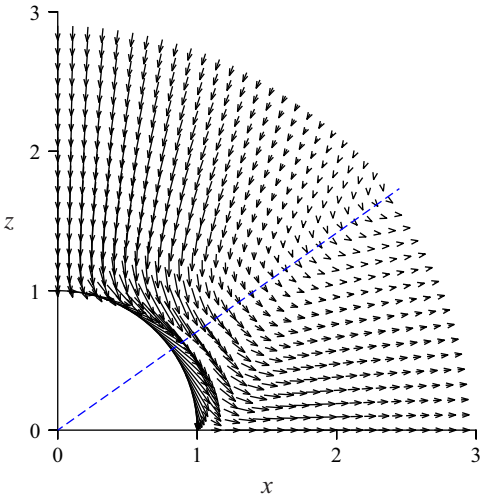


Figure 2. The velocity vectors (arrows) for the flow outside the drop due to an oscillating magnetic field. The applied magnetic field is along the z axis, and x is along any direction in the equatorial plane. The solid quarter-circle is the boundary of the drop. The flow is in the azimuthal direction ($\bar{v}_r = 0$) on the blue dashed line.

The radial and azimuthal components of the velocity and the pressure can now be calculated from the expressions (3.2) and (3.3) with $C_1 = 0$ and $C_3 = 3C_2$,

$$\bar{v}_r = \frac{9C_2(1-r^2)(3\cos(\theta)^2-1)}{2r^4}, \tag{3.7}$$

$$\bar{v}_\theta = \frac{9C_2\sin(\theta)\cos(\theta)}{r^4}, \tag{3.8}$$

$$\bar{p} = -\frac{9C_2\eta_r(3\cos(\theta)^2-1)}{r^3}. \tag{3.9}$$

Comparing (2.38), (2.39) and (3.8), we find that

$$C_2 = \frac{\bar{V}_\theta\big|_{r=1}}{9}. \tag{3.10}$$

The velocity vectors outside the drop are shown in figure 2. There is a biaxial extensional flow with compression along the axial direction and extension in the equatorial plane. This is generated by an axisymmetric point force dipole aligned along the axial direction.

The 'particle stress' for a suspension of particles in the Stokes regime is defined as

$$\bar{\sigma}^p_{ij} = \frac{1}{V}\int_S \mathrm{d}S\ \ \bar{\sigma}_{ik}n_k x_j\big|_{r=1}\,, \tag{3.11}$$

where V is the volume of the particle, S is the surface and $\boldsymbol{n}$ is the outwards unit normal. For biaxial extension, the particle stresses are related, $\bar{\sigma}^{(p)}_{xx} = \bar{\sigma}^{(p)}_{yy} = -2\bar{\sigma}^{(p)}_{zz}$, and it is sufficient to determine any one component. The component $\bar{\sigma}^{(p)}_{zz}$ is

$$\bar{\sigma}^{(p)}_{zz} = \frac{1}{V}\int_S \mathrm{d}S\,(\cos(\theta)\bar{\sigma}_{rr} - \sin(\theta)\bar{\sigma}_{\theta r})\cos(\theta), \tag{3.12}$$

https://doi.org/10.1017/jfm.2025.10176 Published online by Cambridge University Press

where $\bar{\sigma}_{rr}$ and $\bar{\sigma}_{\theta r}$ are given in (2.20) and (2.21). Substituting the expressions (3.7) and (3.8) for the velocity components and (3.10) for the constant C_2, we find that

$$\bar{\sigma}_{zz}^{(p)} = \frac{6\eta_r \ \bar{V}_\theta\big|_{r=1}}{5}. \tag{3.13}$$

There is a factor η_r in the above expression because the viscosity to be used in (2.20) and (2.21) is η_o for the fluid outside the drop, whereas the velocities are scaled by the viscosity η_i of the inner fluid in table 1.

3.2. *Asymptotic results for $\beta \ll 1$*

The approximation (B13) for $\bar{F}$ is substituted into (2.34), and solved analytically to obtain

$$\bar{g}^{(i)} = M_1 r^5 + M_2 r^3 + M_3 + \frac{M_4}{r^2} - \frac{\beta^4 r^7}{10\,080}, \tag{3.14}$$

where M_1, M_2, M_3 and M_4 are constants of integration. The boundary condition (2.27) for $r \to 0$ requires $M_3 = M_4 = 0$. The normal velocity condition (2.24) and the tangential stress balance condition (2.41) are used to determine the constants M_1 and M_2, and the final expression for $\bar{g}^{(i)}$ is

$$\bar{g}^{(i)} = \frac{\beta^4 r^3 (1 - r^2)(5r^2(1 + \eta_r) - 5\eta_r - 9)}{50\,400(1 + \eta_r)}. \tag{3.15}$$

The tangential velocity measure $\bar{V}_\theta$ (2.16) and stress measure $\bar{\Sigma}_{\theta r}$ (2.23) at the surface $r = 1$ are

$$\begin{aligned} \bar{V}_\theta\big|_{r=1} &= \left.\frac{\bar{v}_\theta}{\sin(\theta)\cos(\theta)}\right|_{r=1} = \frac{\beta^4}{6300(1 + \eta_r)}, \\ \bar{\Sigma}_{\theta r}\big|_{r=1} &= \left.\frac{\bar{\sigma}_{\theta r}}{\sin(\theta)\cos(\theta)}\right|_{r=1} = -\frac{\beta^4 \eta_r}{1260(1 + \eta_r)}. \end{aligned} \tag{3.16}$$

The parameter $\bar{h}_0$, which characterises the steady shape deformation is determined from (2.46), where the normal stresses inside and outside the drop are given by (2.43) and (2.45), respectively,

$$Ca^{-1}\bar{h}_0 = -\frac{\beta^4(17 + 18\eta_r)}{75\,600(1 + \eta_r)}. \tag{3.17}$$

The parameter $\bar{h}_0$ is negative in the limit $\beta \ll 1$, and it increases proportional to β^4. The implications of this are discussed in § 3.5.

3.3. *Asymptotic results for $\beta \gg 1$*

In this limit, the approximation (B14) for $\bar{F}$ is substituted into (2.34). The solution for $\bar{g}^{(i)}$ is expressed as the sum of the general solution $\bar{g}_g^{(i)}$ and the particular solution $\bar{g}_p^{(i)}$. The general solution of the homogeneous equation which satisfies the condition (2.27) for $r \to 0$ is

$$\bar{g}_g^{(i)} = N_1 r^3 + N_2 r^5, \tag{3.18}$$

where N_1 and N_2 are constants to be determined from the boundary conditions at the interface. The approximation for the particular solution $\bar{g}_p^{(i)}$ in the limit $\beta \gg 1$ is determined as follows. Since the variation of $\bar{F}$ is restricted to a region of thickness β^{-1}

https://doi.org/10.1017/jfm.2025.10176 Published online by Cambridge University Press

close to the wall, the scaled distance from the wall can be defined as $\xi = \beta(1-r)$. When expressed in terms of the scaled variable ξ, (2.34) is

$$\beta^4 \frac{\mathrm{d}^4 \bar{g}_p^{(i)}}{\mathrm{d}\xi^4} - \frac{12\beta^2}{(1-\xi/\beta)^2}\frac{\mathrm{d}^2 \bar{g}_p^{(i)}}{\mathrm{d}\xi^2} - \frac{24\beta}{(1-\xi/\beta)^3}\frac{\mathrm{d}\bar{g}_p^{(i)}}{\mathrm{d}\xi} + \left(\frac{9\beta \exp\left[-\sqrt{2}\xi\right]}{4\sqrt{2}(1-\xi/\beta)^2}\right) = 0. \quad (3.19)$$

Here, we have used the approximation (B14) for $\bar{F}$. The first and last terms on the right-hand side are dominant terms in the limit $\beta \gg 1$. The following solution is obtained by retaining only these two terms and approximating $(1-\xi/\beta) \approx 1$:

$$\bar{g}_p^{(i)} = -\frac{9\exp\left[-\sqrt{2}\xi\right]}{16\sqrt{2}\beta^3} = -\frac{9\exp\left[-\sqrt{2}\beta(1-r)\right]}{16\sqrt{2}\beta^3}. \quad (3.20)$$

The solution for $\bar{g}^{(i)}$ is the sum of (3.18) for $\bar{g}_g^{(i)}$ and (3.20) for $\bar{g}_p^{(i)}$. In the resulting equation, one of the constants is determined from the condition (2.24) that the normal velocity is zero at $r = 1$. The resulting solution has one unknown constant,

$$\bar{g}^{(i)} = N\left(r^5 - r^3\right) + \frac{9\left(r^3 - \exp\left[-\sqrt{2}\beta(1-r)\right]\right)}{16\sqrt{2}\beta^3}. \quad (3.21)$$

The constant N is determined using the boundary condition (2.41), and the final solution for $\bar{g}^{(i)}$ is

$$\bar{g}^{(i)} = \frac{9\left(r^3 - \exp\left[-\sqrt{2}\beta(1-r)\right]\right)}{16\sqrt{2}\beta^3} - \frac{9r^3(1-r^2)}{80\sqrt{2}\beta(1+\eta_r)} + \frac{9(2-5\eta_r)r^3(1-r^2)}{160\beta^2(1+\eta_r)} + \frac{27\eta_r r^3(1-r^2)}{32\sqrt{2}\beta^3(1+\eta_r)}. \quad (3.22)$$

The third and fourth terms on the right-hand side in the above equation are included, because they become dominant for $\eta_r \gg 1$. Using the approximation (3.22) for $\bar{g}^{(i)}$, the measures for the tangential velocity and stress at the interface, (2.16) and (2.23), are

$$\bar{V}_\theta\big|_{r=1} = \left.\frac{\bar{v}_\theta}{\sin(\theta)\cos(\theta)}\right|_{r=1} = \frac{9}{40\sqrt{2}\beta(1+\eta_r)},$$
$$\bar{\Sigma}_{\theta r}\big|_{r=1} = \left.\frac{\bar{\sigma}_{\theta r}}{\sin(\theta)\cos(\theta)}\right|_{r=1} = -\frac{9\eta_r}{8\sqrt{2}\beta(1+\eta_r)}. \quad (3.23)$$

The drop deformation in the limit of low capillary number is characterised by the parameter $\bar{h}_0$, which is determined from (2.46), (2.43) and (2.45). In the limit $\beta \gg 1$, $\tilde{g}^{(i)} \sim \beta^{-1}$ (3.22). The pressure is evaluated from (2.56), in which the dominant term is the third derivative of $\tilde{g}^{(i)}$ on the right-hand side which is $O(1)$ due to the first term on the right-hand side of (3.22). Due to this term, $\bar{\sigma}_{rr}^{(i)}$ is $O(1)$. The stress in the outer fluid $\bar{\sigma}_{rr}^{(o)}$ is $O(\beta^{-1})$, because the flow is driven by the tangential velocity and stress at the interface which is proportional to β^{-1}. Therefore, the parameter $\bar{h}_0$ is calculated from the relation (2.46),

$$Ca^{-1}\bar{h}_0 = \frac{\bar{\Sigma}_{rr}^{(i)}\big|_{r=1}}{6} = \frac{1}{36}\left.\frac{\mathrm{d}^3\tilde{g}^{(i)}}{\mathrm{d}r^3}\right|_{r=1} = -\frac{1}{32}. \quad (3.24)$$

Here, we have retained only the $O(1)$ contribution to $(\mathrm{d}^3\tilde{g}^{(i)}/\mathrm{d}r^3)$ on the right-hand side.

https://doi.org/10.1017/jfm.2025.10176 Published online by Cambridge University Press

3.4. *Numerical results for $\beta \sim 1$*

The fourth-order differential equation (2.34) for $\bar{g}^{(i)}$, with the function $\bar{F}$ specified by (B12), is solved numerically as follows. A third-order polynomial expansion of $\bar{F}$ about $r = 0$ is used to determine the function $\bar{g}^{(i)}$ analytically at $r = 0.02$ that satisfies the conditions (2.27) at $r = 0$. The solution contains two constants, since (2.34) is a fourth-order equation. For initial guesses of these two constants, numerical integration using a fourth-order Runge–Kutta scheme is used to determine the value of $\bar{g}^{(i)}$ and its derivatives at $r = 1$. A two-dimensional Newton–Raphson iteration procedure is used to converge to the values of the constants that satisfy the conditions (2.24) and (2.41).

The stream function is calculated from $\bar{g}^{(i)}$ using (2.11), and the velocities within the drop are determined from the relations (2.15). The vector plots for the circulation within the drop are shown in figure 3 for $\beta = 1$ and for three different viscosity ratios. The vectors are shown in the meridional $x-z$ plane, where z is the axis in the direction of the magnetic field, and x is any direction on the equatorial plane perpendicular to the magnetic field. The velocity field is axisymmetric about the z axis. The velocity field below the equatorial plane is a mirror image of that above the equatorial plane. Therefore, the velocity field is shown only for $z > 0$ in figure 3.

An axisymmetric circulation is observed in each hemisphere, where the flow is inwards at the equatorial plane, and outwards along the axis. The circulation is from the axis to the equatorial plane close to the surface, and in the opposite direction near the centre. There is a spherical surface, shown by the dashed red lines in figure 3, where $\bar{v}_\theta = 0$, and the flow is in the radial direction. The velocity is the azimuthal direction, and $\bar{v}_r = 0$, along the dashed blue lines. The intersection of these two is the centre of circulation where the velocity is zero. The inward velocity at the equatorial plane can be understood from the direction of the body force density. Equations (A31)–(A33) show that the electric field is in the $-\hat{\boldsymbol{e}}_\phi$ direction along the surface. Equation (A24) shows that the magnetic field near the surface has contributions in the $\hat{\boldsymbol{e}}_r$ and $-\hat{\boldsymbol{e}}_\theta$ direction for $\beta \ll 1$, while (A29) shows that the magnetic field is primarily in the $-\hat{\boldsymbol{e}}_\theta$ direction for $\beta \gg 1$. Consequently, the force density, which is the cross product of the electric and magnetic fields, is in the $-\hat{\boldsymbol{e}}_r$ direction at the equator, resulting in an inwards flow. The electric field and the force density decrease to zero along the axis, but mass conservation results in an outwards flow. This results in the circulation pattern observed in figure 3.

As the ratio of viscosities η_r is increased, figure 3 shows that the flow pattern does not change qualitatively. However, the tangential velocity at the surface decreases as η_r increases. The limit $\eta_r \to \infty$ is equivalent to the zero tangential velocity condition at the surface. However, figure 3 shows that internal circulation persists even when the tangential velocity at the surface is zero.

The velocity measures $\bar{V}_r = \bar{v}_r/(3\cos(\theta)^2 - 1)$ and $\bar{V}_\theta = \bar{v}_\theta/(\cos(\theta)\sin(\theta))$, (2.15)–(2.16), are shown as a function of r in figure 4. The radial velocity, shown by the red curves, is zero at the centre and the surface of the drop, and has a maximum in between. The velocity in the azimuthal direction decreases from zero near the centre, reaches a minimum and then increases and becomes positive. The dashed red line in figure 3 shows the location at which the azimuthal velocity passes through zero. The tangential velocity has zero slope at the surface for $\eta_r \to 0$ due to the zero-stress condition at the surface, and it decreases to zero for $\eta_r \to \infty$ consistent with the no-slip condition.

The $\beta \ll 1$ asymptotic results, derived from (3.15), are shown by the dashed black lines in figure 4(*a–c*) for $\beta = 1$. The numerical and asymptotic results are found to be in quantitative agreement. The $\beta \gg 1$ asymptotic results, derived from (3.22), are shown by the dashed black lines in figure 4(*g–i*). These asymptotic results qualitatively capture

https://doi.org/10.1017/jfm.2025.10176 Published online by Cambridge University Press

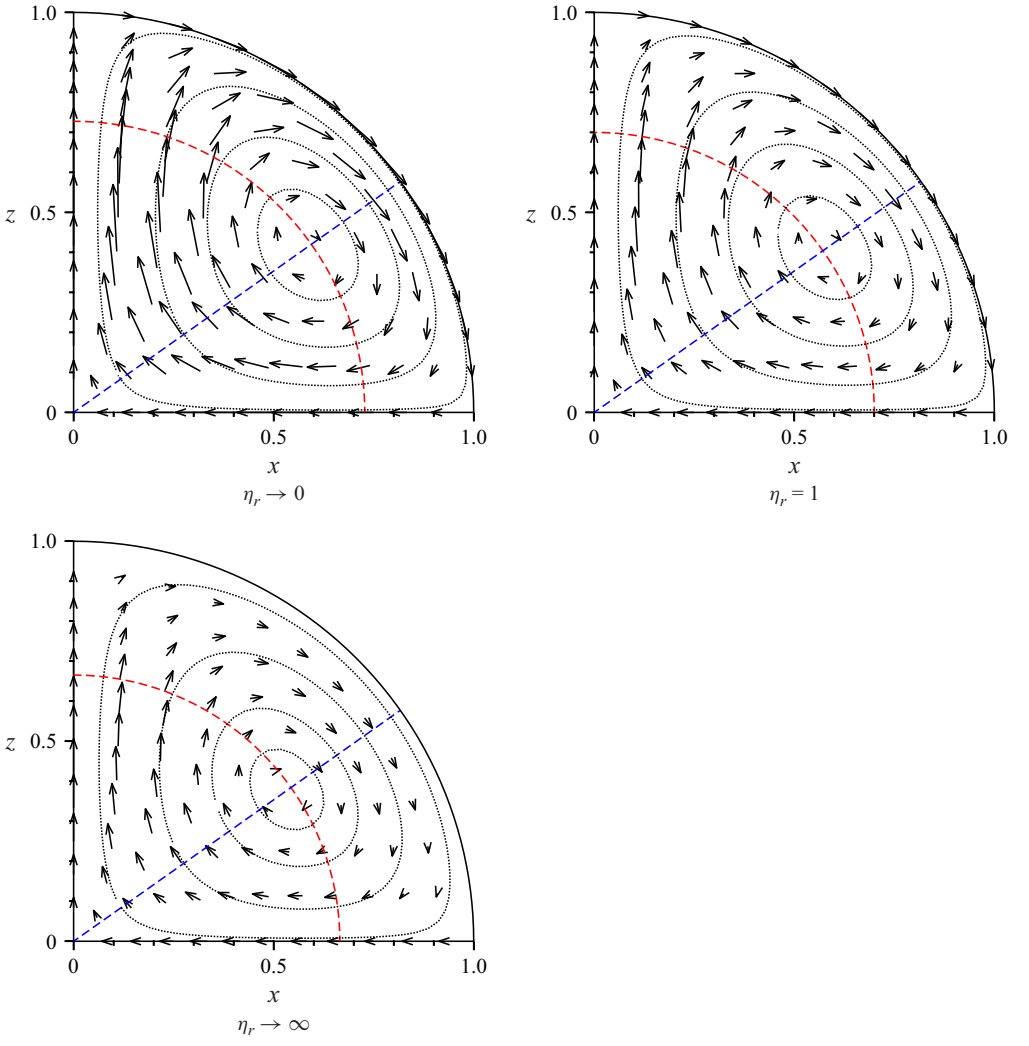


Figure 3. The velocity vectors (arrows) and the streamlines (dotted lines) for the flow in a drop due to an oscillating magnetic field for different values of the viscosity ratio η_r. The applied magnetic field is along the z axis, and x is along any direction in the equatorial plane. The solid quarter-circle is the boundary of the drop. The flow is radial ($\bar{v}_\theta = 0$) along the dashed red quarter circle. The flow is in the azimuthal direction ($\bar{v}_r = 0$) on the blue dashed line.

the variation in the velocity components, but there are quantitative differences. For $\beta = 30$ (not shown here), we find quantitative agreement to within 2 % between the asymptotic and numerical results.

The tangential velocity and stress measures at the surface, $\bar{V}_\theta\big|_{r=1}$ and $\bar{\Sigma}_{\theta r}\big|_{r=1}$, are shown as a function of β in figure 5. From the asymptotic expressions (3.16) and (3.23), $\bar{V}_\theta\big|_{r=1} \propto (1+\eta_r)^{-1}$ and $\Sigma_{\theta r}|_{r=1} \propto \eta_r/(1+\eta_r)$ in both limits for $\beta \ll 1$ and $\beta \gg 1$. Therefore, the products $(1+\eta_r)\ \bar{V}_\theta\big|_{r=1}$ and $-(1+\eta_r)\ \bar{\Sigma}_{\theta r}/\eta_r\big|_{r=1}$ are shown as a function of β in figure 5.

Figure 5 shows that $(1+\eta_r)\ \bar{V}_\theta\big|_{r=1}$ and $-((1+\eta_r)/\eta_r)\ \bar{\Sigma}_{\theta r}\big|_{r=1}$ collapse on to a universal curve independent of η_r. The $\beta \ll 1$ asymptotic expressions in (3.16), shown by the dotted red lines on the left, are in quantitative agreement with the numerical results for

https://doi.org/10.1017/jfm.2025.10176 Published online by Cambridge University Press

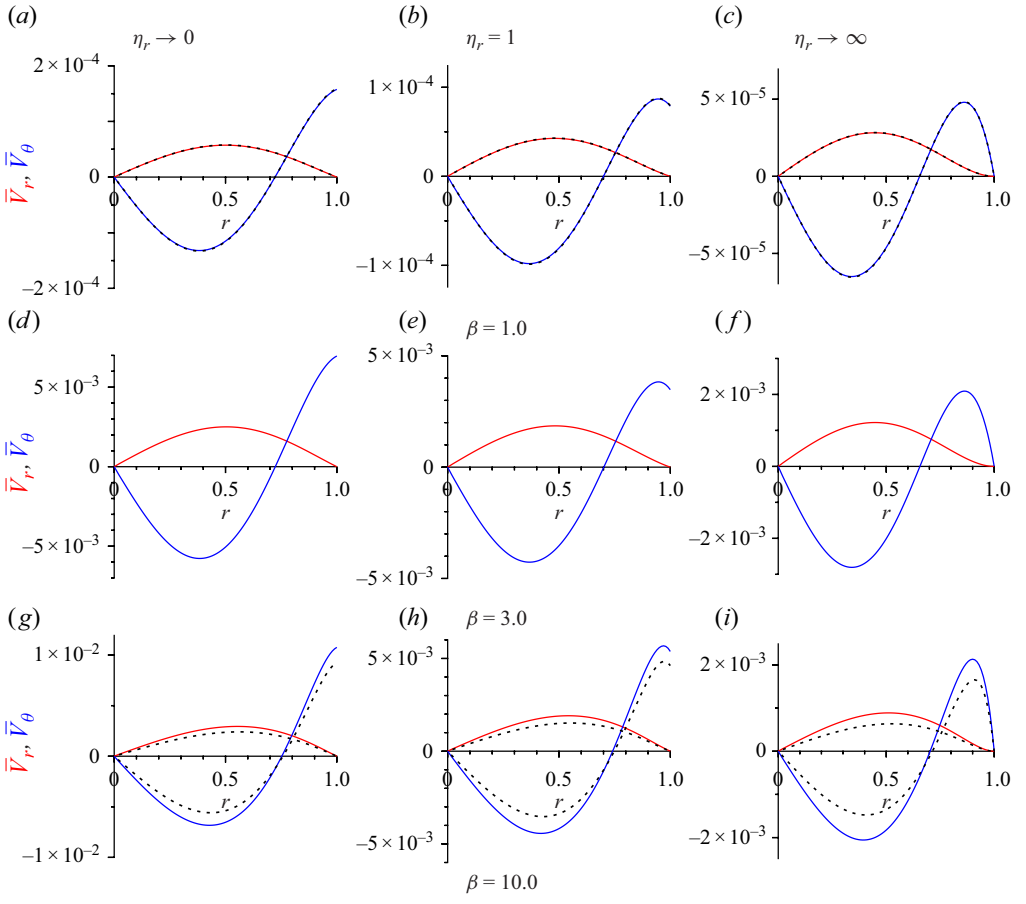


Figure 4. The velocity measures $\bar{V}_r = \bar{v}_r/(3\cos(\theta)^2 - 1)$ ((2.16), red line) and $\bar{V}_\theta = \bar{v}_\theta/(\cos(\theta)\sin(\theta))$ ((2.16), blue line) for $\eta_r \to 0$ (*a*,*d*,*g*), $\eta_r = 1$ (*b*,*e*,*h*) and $\eta_r \to \infty$ (*c*,*f*,*i*), and for $\beta = 1$ (*a*–*c*), $\beta = 3$ (*d*–*f*) and $\beta = 10$ (*g*–*i*). The dashed black lines in (*a*)–(*c*) are obtained from the $\beta \ll 1$ asymptotic solution (3.15), and the dashed black lines in the (*g*)–(*i*) are obtained from the $\beta \gg 1$ asymptotic solution (3.22).

$\beta \lesssim 1$. The $\beta \gg 1$ asymptotic expressions in (3.23), shown by the dotted red lines on the right, accurately predict the numerical results for $\beta \gtrsim 30$. The velocity and stress measures pass through a maximum at $\beta \approx 6.1$. From (3.16) and (3.23), it is also observed that

$$-((1+\eta_r)/\eta_r)\ \bar{\Sigma}_{\theta r}\big|_{r=1} = 5(1+\eta_r)\ \bar{V}_\theta\big|_{r=1}\,, \tag{3.25}$$

for $\beta \ll 1$ and $\beta \gg 1$. In figure 5, the scale in the ordinate in figure 5(*b*) is five times that in figure 5(*a*). The identical nature of the curves in figures 5(*a*) and 5(*b*) shows that (3.25) is quantitatively accurate for $\beta \sim 1$ also.

3.5. *Drop deformation*

The deformation of the drop due to the steady flow is examined in the limit of low capillary number; it is shown in § 5 that this limit is applicable for practical situations. The deformation is characterised by the parameter $\bar{h}_0$ defined in (2.31)–(2.33), which is determined from the normal stress balance (2.46) in the low capillary number limit. This parameter is negative, indicating that a spherical drop deforms into an oblate spheroid which is extended at the equator and compressed at the poles. The deformed shape is

https://doi.org/10.1017/jfm.2025.10176 Published online by Cambridge University Press

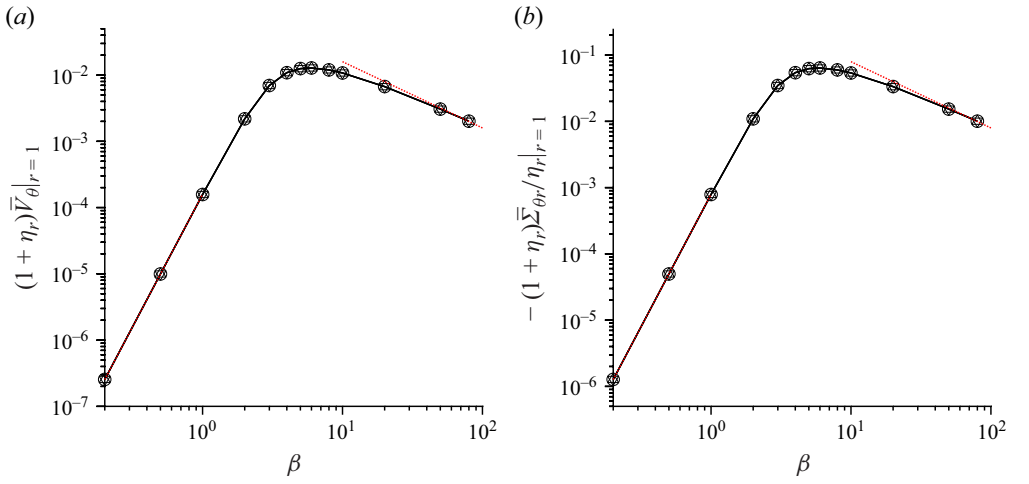


Figure 5. The measure (*a*) $(1+\eta_r)\bar{V}_\theta$ of the tangential velocity and (*b*) $-((1+\eta_r)/\eta_r)\bar{\Sigma}_{\theta r}$ of the tangential stress at the surface $r=1$ as a function of β for viscosity ratio $\eta_r \to 0$ ($\circ$), $\eta_r = 1.0$ ($\triangle$), $\eta_r \to \infty$ (∇). The definitions of $\bar{V}_\theta$ and $\bar{\Sigma}_{\theta r}$ are given in (2.16) and (2.23), respectively. The dotted red line on the left is the $\beta \ll 1$ asymptotic result (3.16). The dotted red line on the right is the $\beta \gg 1$ asymptotic result (3.23).

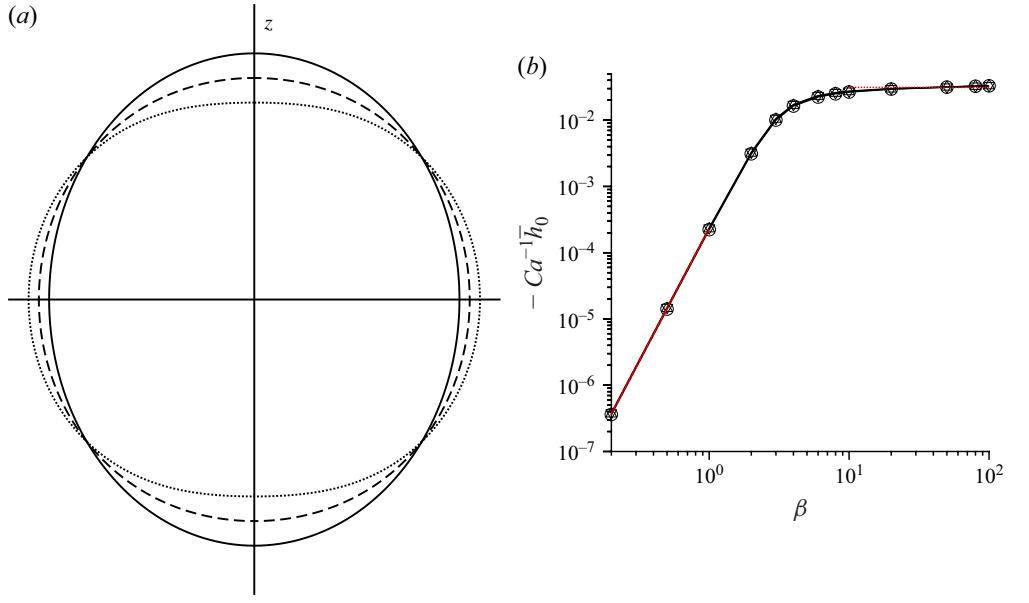


Figure 6. (*a*) The shape of the conducting drop for the spherical drop (solid line), $\bar{h}_0 = -0.05$ (dashed line) and $\bar{h}_0 = -0.1$ (dotted line), and (*b*) the parameter $-Ca^{-1}\bar{h}_0$ in (2.46) as a function of β for $\eta_r \to 0$ ($\circ$), $\eta_r = 1$ ($\triangle$) and $\eta_r \to \infty$ (∇). The dotted red lines on the left in (*b*) show (3.17) in the limit $\beta \ll 1$, and the dotted red line on the right is $-Ca^{-1}\bar{h}_0 = 1/32$ (3.24).

shown for $\bar{h}_0 = -0.05$ and -0.1 in figure 6(*a*). The shape is axisymmetric about the z axis.

From the normal stress balance (2.46) at the interface, it is evident that $\bar{h}_0 \propto Ca$, since the left-hand side is independent of Ca. The parameter $-Ca^{-1}\bar{h}_0$ is plotted as a function of β in figure 6. This figure shows that $-Ca^{-1}\bar{h}_0$ increases proportional to β^4 for $\beta \ll 1$,

https://doi.org/10.1017/jfm.2025.10176 Published online by Cambridge University Press

and it approaches a constant value for $\beta \gg 1$. The dashed red lines on the left show the asymptotic results (3.17) for different values of η_r. There are three red lines for $\eta_r \to 0$, $\eta_r = 1$ and $\eta_r \to \infty$. However, these are indistinguishable because the numerical values are very close. There is excellent agreement between the asymptotic and numerical results for $\beta \lesssim 1$. The dashed red line on the right is the $\beta \gg 1$ asymptotic result, (3.24). This is in quantitative agreement with the numerical results for $\eta_r \gtrsim 10$.

3.6. *Joule heating*

An issue of importance is whether sufficient heat can be generated by Joule heating due to the eddy currents to increase the temperature of the surrounding fluid. Attention is restricted to the total rate of heat generation in the entire drop. At steady state, this has to be the heat transfer rate from the drop to the surrounding fluid. Based on this, the difference between the drop and the ambient fluid is calculated in § 5.

The rate of generation of heat energy per unit volume is expressed in dimensional form as

$$q^\dagger = \frac{\boldsymbol{J}^\dagger \cdot \boldsymbol{J}^\dagger}{\kappa}. \tag{3.26}$$

If we substitute $\boldsymbol{J}^\dagger = 1/2(\tilde{\boldsymbol{J}}^\dagger \exp(\imath t) + (\tilde{\boldsymbol{J}}^\dagger \exp(\imath t))^*)$, the steady part of the energy generation per unit volume is

$$\bar{q}^\dagger = \frac{\tilde{\boldsymbol{J}}^\dagger \cdot \tilde{\boldsymbol{J}}^{\dagger *}}{2\kappa} = \frac{\kappa \tilde{\boldsymbol{E}}^\dagger \cdot \tilde{\boldsymbol{E}}^{\dagger *}}{2}. \tag{3.27}$$

The non-dimensional energy generation per unit volume is defined as $\bar{q} = (\bar{q}^\dagger/(H_0^2/R^2\kappa))$. Equation (3.27) is non-dimensionalised,

$$\bar{q} = \frac{\tilde{\boldsymbol{E}} \cdot \tilde{\boldsymbol{E}}^*}{2}. \tag{3.28}$$

Substituting (A31) for $\tilde{\boldsymbol{E}}$, the heat generation rate per unit volume is

$$\begin{aligned}\bar{q} &= \frac{9\sin(\theta)^2}{8\sin(\tilde{\beta})\sin(\tilde{\beta}^*)}\frac{\mathrm{d}\tilde{\chi}}{\mathrm{d}r}\frac{\mathrm{d}\tilde{\chi}^*}{\mathrm{d}r} \\ &= \frac{9\sin(\theta)^2}{8\big(\cosh\big(\sqrt{2}\beta\big) - \cos\big(\sqrt{2}\beta\big)\big)}\left(\frac{\beta^2\big(\cosh\big(\sqrt{2}\beta r\big) + \cos\big(\sqrt{2}\beta r\big)\big)}{r^2}\right. \\ &\quad \left. - \frac{\sqrt{2}\beta\big(\sinh\big(\sqrt{2}\beta r\big) + \sin\big(\sqrt{2}\beta r\big)\big)}{r^3} + \frac{\big(\cosh\big(\sqrt{2}\beta r\big) - \cos\big(\sqrt{2}\beta r\big)\big)}{r^4}\right).\end{aligned} \tag{3.29}$$

The total heat generated per unit time is

$$\begin{aligned}\bar{Q} &= 2\pi \int_0^\pi \sin(\theta)\mathrm{d}\theta \int_0^1 r^2 \mathrm{d}r\, \bar{q} \\ &= 3\pi\left(\frac{\beta\big(\sinh\big(\sqrt{2}\beta\big) + \sin\big(\sqrt{2}\beta\big)\big)}{\sqrt{2}\big(\cosh\big(\sqrt{2}\beta\big) - \cos\big(\sqrt{2}\beta\big)\big)} - 1\right).\end{aligned} \tag{3.30}$$

Here, the heat generation rate $\bar{Q}$ is non-dimensionalised by $(H_0^2 R/\kappa))$. The following limiting values of the scaled heat generation rate are derived in the limits $\beta \ll 1$ and $\beta \gg 1$:

https://doi.org/10.1017/jfm.2025.10176 Published online by Cambridge University Press

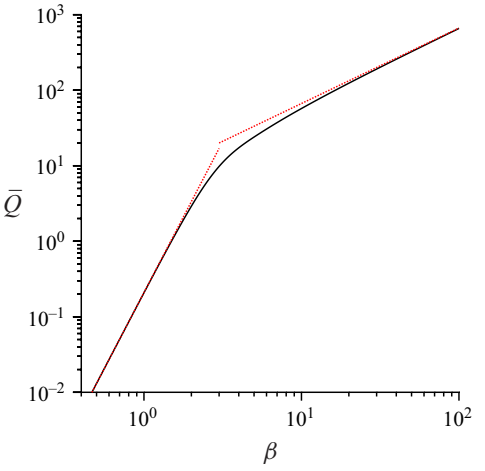


Figure 7. The non-dimensional heat generation rate per unit time $\bar{Q}$ due to Joule heating as a function of β. The dotted red line on the left is the asymptotic expression (3.31) for $\beta \ll 1$, and the dotted red line on the right is the asymptotic expression (3.32) for $\beta \gg 1$.

$$\bar{Q} = \frac{\beta^4 \pi}{15} \quad \text{for} \quad \beta \ll 1, \tag{3.31}$$

$$= \frac{3\pi\beta}{\sqrt{2}} \quad \text{for} \quad \beta \gg 1. \tag{3.32}$$

The non-dimensional heat generation rate $\bar{Q}$ is shown as a function of β in figure 7. The $\beta \ll 1$ asymptotic expression (3.31) is in quantitative agreement with the numerical solution for $\beta \lesssim 2$, while the $\beta \gg 1$ asymptotic expression (3.32) accurately predicts the heat generation rate for $\beta \gtrsim 20$.

4. Oscillatory component of velocity field

The fourth-order ordinary differential equation (2.47) for $\tilde{g}^{(i)}$ is solved with $\tilde{F}$ given by (B20), and subject to the boundary conditions (2.24) and (2.54) at $r = 1$ and (2.27) for $r \to 0$.

The velocity fields and velocity measures are examined in the limits $\beta \ll 1$ and $\beta \gg 1$, where the approximations (B25) and (B26) are used for $\tilde{F}$. The viscosity ratio η_r is set equal to unity in this section; the variation of the profiles with η_r is similar to that for a steady flow. There are two Reynolds numbers, Re_ω based on the fluid properties inside and $Re_\omega^{(o)}$ based on fluid properties outside the drop. Numerical results for the velocity fields and velocity measures are determined as a function of Re_ω in the limits $\beta \ll 1$ and $\beta \gg 1$. In addition, in each of the limits $\beta \ll 1$ and $\beta \gg 1$, asymptotic results for the velocity measures are calculated for $Re_\omega \ll 1$ and $Re_\omega \gg 1$. To narrow the parameter space, we assume that $Re_\omega = Re_\omega^{(o)}$ in the numerical calculations, but there is no restriction on the asymptotic results in the limits of low and high Re_ω.

4.1. *Flow outside the drop*

The velocity fields outside the drop are calculated from (2.52) for $\tilde{g}^{(o)}$, and the definitions (2.11) for the stream function and (2.5) for the velocity. The solution (2.52) satisfies the condition (2.24) ($\tilde{v}_r = 0$) at $r = 1$, and the tangential velocity condition (2.25) is used to

https://doi.org/10.1017/jfm.2025.10176 Published online by Cambridge University Press

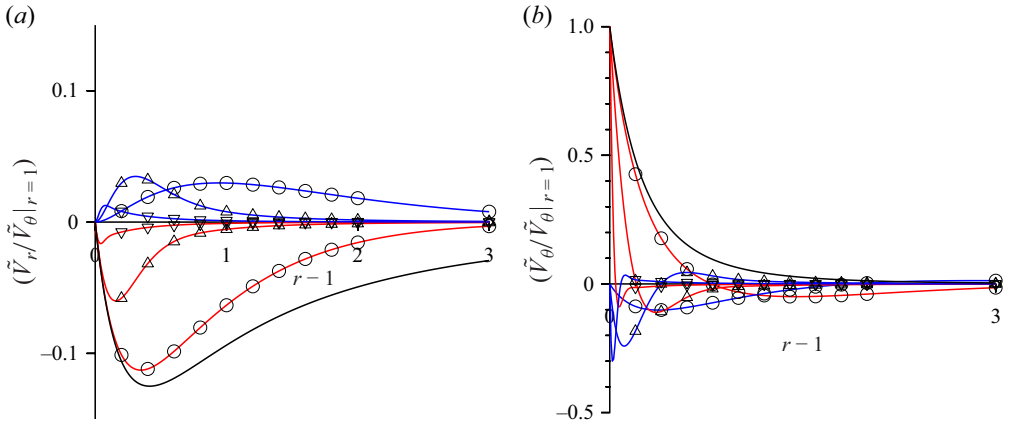


Figure 8. The velocity scaled velocity measures $(\tilde{V}_r/\tilde{V}_\theta|_{r=1})$ (*a*) and $(\tilde{V}_\theta/\tilde{V}_\theta|_{r=1})$ (*b*) as a function of the distance from the surface, $r-1$ for $Re_\omega = 1$ (○), $Re_\omega = 30$ (△), $Re_\omega = 1000$ (▽). The red lines are real parts, and the blue lines are the imaginary parts. The black line is the result (2.37)–(2.38) for $Re_\omega = 0$.

express the constant D in terms of $\tilde{V}_\theta\Big|_{r=1}$,

$$\tilde{v}_r = \tilde{V}_r\big(3\cos(\theta)^2 - 1\big), \quad \tilde{v}_\theta = \tilde{V}_\theta \sin(\theta)\cos(\theta), \tag{4.1}$$

where

$$\frac{\tilde{V}_r}{\tilde{V}_\theta|_{r=1}} = \frac{\big[\big(3+3\tilde{\alpha}_o r + \tilde{\alpha}_o^2 r^2\big)\exp\left(-\tilde{\alpha}_o(r-1)\right) - \big(3+3\tilde{\alpha}_o+\tilde{\alpha}_o^2\big)\big]}{r^4\tilde{\alpha}_o^2(1+\tilde{\alpha}_o)}, \tag{4.2}$$

$$\frac{\tilde{V}_\theta}{\tilde{V}_\theta|_{r=1}} = \frac{\big[\big(6+6\tilde{\alpha}_o r + 3\tilde{\alpha}_o^2 r^2 + \tilde{\alpha}_o^3 r^3\big)\exp\left(-\tilde{\alpha}_o(r-1)\right) - 2\big(3+3\tilde{\alpha}_o+\tilde{\alpha}_o^2\big)\big]}{r^4\tilde{\alpha}_o^2(1+\tilde{\alpha}_o)}. \tag{4.3}$$

The real and imaginary parts of the ratios $(\tilde{V}_r/\tilde{V}_\theta|_{r=1})$ and $(\tilde{V}_\theta/\tilde{V}_\theta|_{r=1})$ are shown as a function of $r-1$ by the red and blue lines in figure 8, respectively. Three different values of the Reynolds number, $Re_\omega = 1$, 30 and 1000 are considered. Also shown by the black lines are the real parts of $(\tilde{V}_r/\tilde{V}_\theta|_{r=1})$ and $(\tilde{V}_\theta/\tilde{V}_\theta|_{r=1})$ for a steady flow with $Re_\omega = 0$; these are derived from (2.37)–(2.39), and the imaginary parts are zero in this case. It is evident that the magnitudes of the velocity and the extent of the flow both decrease as Re_ω is increased. For a steady flow, (2.37)–(2.38) show that the magnitude of the velocity decreases as r^{-2} for $r \gg 1$. In contrast, (4.2)–(4.3) show that $\tilde{V}_r$ and $\tilde{V}_\theta$ contain one term that decreases proportional to r^{-4}, while the other term decreases exponentially over distance $\tilde{\alpha}_o^{-1} \sim 1/\sqrt{Re_\omega}$. Thus, the disturbance due to the oscillatory component of the velocity field is much shorter in range in comparison with that due to the steady component. Sufficiently far from the drop, the dominant contribution is due to the steady component.

4.2. *Limit* $\beta \ll 1$

In this limit, the approximation (B25) for $\tilde{F}$ is substituted into (2.47). The analytical solution for the resulting equation consists of a general solution and a particular solution

https://doi.org/10.1017/jfm.2025.10176 Published online by Cambridge University Press

which is a polynomial in r,

$$\tilde{g}^{(i)} = \frac{K_1}{r^2} + K_2 r^3 + K_3\big(\sinh(\tilde{\alpha}r)(1+3(\tilde{\alpha}r)^{-2}) - 3(\tilde{\alpha}r)^{-1}\cosh(\tilde{\alpha}r)\big) + K_4\big(\cosh(\tilde{\alpha}r)(1+3(\tilde{\alpha}r)^{-2}) - 3(\tilde{\alpha}r)^{-1}\sinh(\tilde{\alpha}r)\big) + \left(\frac{\beta^4 r^5}{280\tilde{\alpha}^2}\right), \tag{4.4}$$

where K_1, K_2, K_3 and K_4 are constants of integration. The first four terms in the above solution are identical to (2.51) for $\tilde{g}^{(o)}$, but are expressed in a slightly different manner to facilitate the application of boundary conditions. The boundary conditions (2.27) for $r \to 0$ require that $K_1 = K_4 = 0$. A relation between the constants K_2 and K_3 is obtained from the zero normal velocity boundary condition $\tilde{g}^{(i)} = 0$ at $r = 1$ (2.24),

$$\tilde{g}^{(i)} = K\Big[\sinh(\tilde{\alpha}r)(1+3(\tilde{\alpha}r)^{-2}) - r^3\sinh(\tilde{\alpha})(1+3\tilde{\alpha}^{-2}) - 3(\tilde{\alpha}r)^{-1}\cosh(\tilde{\alpha}r) + 3r^3\tilde{\alpha}^{-1}\cosh(\tilde{\alpha})\Big] + \beta^4\left(\frac{r^5 - r^3}{280\tilde{\alpha}^2}\right). \tag{4.5}$$

The constant K is determined from the tangential stress boundary condition (2.54).

Since the last term on the right-hand side in (4.5) is proportional to β^4, and the right-hand side of boundary condition at the surface (2.54) does not depend on β, the constant K is also proportional to β^4. Consequently, the functions $\tilde{g}^{(i)}$, the components of the velocity and the stress are all proportional to β^4. Therefore, the results are expressed as ratios of the dynamical quantities and β^4.

Vector plots for the real and imaginary parts of velocity vectors $\tilde{\boldsymbol{v}}$ are shown in figures 9(*a–c*) and 9(*d–f*) for three different values of Re_ω. The real and imaginary parts of $\tilde{V}_r$ and $\tilde{V}_\theta$, defined in (2.16), are shown as a function of r in figure 9(*g–i*). For $Re_\omega = 1$, the real part of $\tilde{v}$ is much larger than the imaginary part, and the real part is similar to that for a steady flow in figure 3 for $\eta_r = 1$. This is expected at low Reynolds number, where viscous effects are dominant and the flow is quasisteady. The term proportional to $\tilde{\alpha}^2 = 2\imath\, Re_\omega$ is neglected in (2.47), and $\beta \ll 1$ the asymptotic expression (B25) for $\tilde{F}$ is real. Due to this, the solution for the stream function and the velocity components are also real. The flow field responds instantaneously to the forcing at the same time instant. Therefore, the real part of the velocity field is similar to that for steady forcing. Moreover, the imaginary part of $\tilde{\boldsymbol{v}}$, which is related to the out-of-phase component of the velocity field, is small compared with the real part of $\tilde{\boldsymbol{v}}$ related to the in-phase component. Since the flow is quasisteady, the variation of $\mathrm{Re}(\tilde{V}_r)$ and $\mathrm{Re}(\tilde{V}_\theta)$ in figure 9(*g*) is numerically close to that of $\bar{V}_r$ and $\bar{V}_\theta$ in figure 4 for $\beta = 1$ and $\eta_r = 1$.

For $Re_\omega = 1000$, figure 9 shows that the imaginary part of the velocity vector is much larger than the real part. In the bulk of the drop, the term proportional to $\tilde{\alpha}^2 = 2\imath\, Re_\omega$ in (2.47) is dominant. Since $\tilde{F}$ is real for $\beta \ll 1$ (see (B25)), the leading-order solution for $\tilde{g}^{(i)}$ and $\tilde{\boldsymbol{v}}$ are imaginary for $Re_\omega \gg 1$ within the drop. However, there is a sharp increase in the real part close to the surface due to viscous effects. If the viscous terms are neglected in (2.47), a second-order differential equation results, and it is not possible to satisfy all the boundary conditions. The boundary layer approximation is invoked, where inertial and viscous effects are comparable in a layer of thickness $Re_\omega^{-1/2}$. The resulting sharp variations in the $\tilde{V}_r$ and $\tilde{V}_\theta$ close to the surface are captured in figure 9(*i*).

The oscillatory parts of the tangential velocity measure $\tilde{V}_\theta$ (2.16) and stress measure $\tilde{\Sigma}_{\theta r}$ (2.23) at the surface $r = 1$ can be evaluated analytically in the limits $Re_\omega \ll 1$ and

https://doi.org/10.1017/jfm.2025.10176 Published online by Cambridge University Press

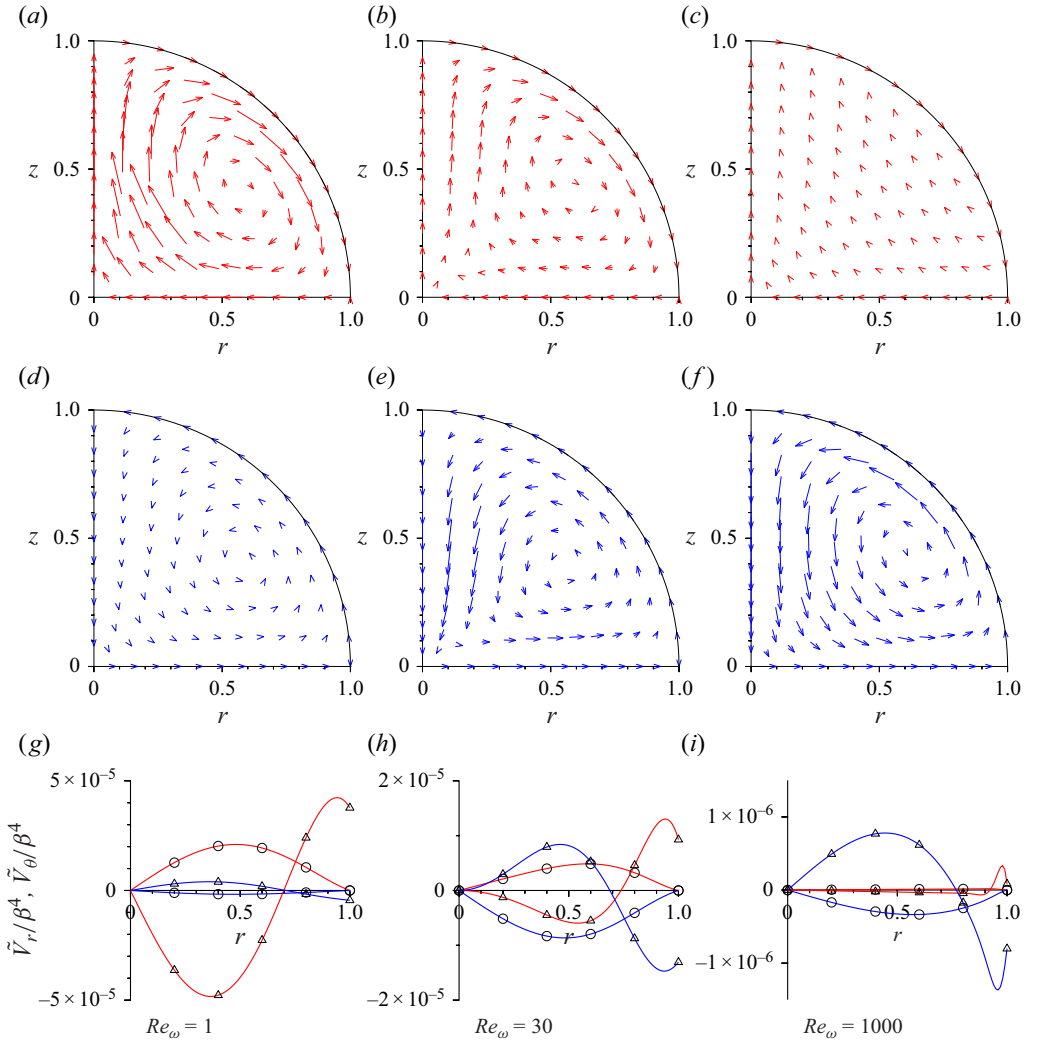


Figure 9. Vector plots of the real part (*a–c*) and imaginary part (*d–f*) of the velocity vectors and (*g–i*) the velocity measures $\tilde{V}_r = \tilde{v}_r/(3\cos(\theta)^2 - 1)$ ((2.16), ∘) and $\tilde{V}_\theta = \tilde{v}_\theta/(\sin(\theta)\cos(\theta))$ ((2.16), △) in the limit $\beta \ll 1$, all scaled by β^4, for $\eta_r = 1$ and for three different values of Re_ω. In (*g*)–(*i*), the real parts are the red lines and the imaginary parts are the blue lines.

$Re_\omega \gg 1$. In the limit $Re_\omega \ll 1$, the term proportional to $\tilde{\alpha}^2$ in (2.47) is neglected, and the equation becomes identical to that for a steady flow. The expressions for the tangential velocity and stress measures are identical to the relations (3.16),

$$\tilde{V}_\theta\Big|_{r=1} = \frac{\tilde{v}_\theta}{\sin(\theta)\cos(\theta)}\Big|_{r=1} = \frac{\beta^4}{6300(1+\eta_r)},$$
$$\tilde{\Sigma}_{\theta r}\Big|_{r=1} = \frac{\tilde{\sigma}_{\theta r}}{\cos(\theta)\sin(\theta)}\Big|_{r=1} = -\frac{\beta^4\eta_r}{1260(1+\eta_r)}. \tag{4.6}$$

In the limit $Re_\omega \gg 1$, the velocity and stress measures are

https://doi.org/10.1017/jfm.2025.10176 Published online by Cambridge University Press

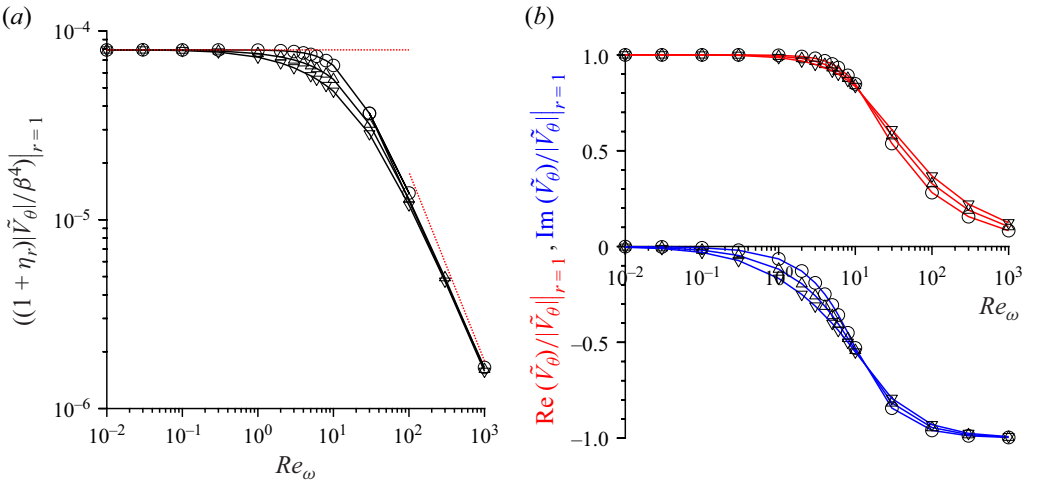


Figure 10. The measure (*a*) $((1+\eta_r)|\tilde{V}_\theta|/\beta^4)|_{r=1}$ and (*b*) $(\mathrm{Re}(\tilde{V}_\theta)/|\tilde{V}_\theta|)|_{r=1}$ (red) and $(\mathrm{Im}(\tilde{V}_\theta)/|\tilde{V}_\theta|)|_{r=1}$ (blue) as a function of Re_ω for viscosity ratio $\eta_r \to 0$ (○), $\eta_r = 1.0$ (△), $\eta_r \to \infty$ (▽). The definition of $\tilde{V}_\theta$ is given in (2.16). The dotted red line on the left in (*a*) is the $Re_\omega \ll 1$ asymptotic result (4.6). The dotted red line on the right in (*a*) is the $Re_\omega \gg 1$ asymptotic result (4.7).

$$\tilde{V}_\theta\Big|_{r=1} = -\frac{\imath\beta^4}{280 Re_\omega\left(1+\eta_r\sqrt{Re_\omega^{(o)}/Re_\omega}\right)},$$
$$\tilde{\Sigma}_{\theta r}\Big|_{r=1} = \frac{\beta^4(-1+\imath)\eta_r\sqrt{Re_\omega^{(o)}/Re_\omega}}{280\sqrt{Re_\omega}\left(1+\eta_r\sqrt{Re_\omega^{(o)}/Re_\omega}\right)}. \tag{4.7}$$

Here, we find that the shear stress at the surface decreases proportional to $Re_\omega^{-1/2}$ while the surface velocity decreases proportional to Re_ω^{-1}.

The asymptotic expressions (4.6) and (4.7) show that the velocity measures are independent of Re_ω for $Re_\omega \ll 1$, but they depend on both Re_ω and $Re_\omega^{(o)}$ for $Re_\omega \gg 1$. For the special case $Re_\omega = Re_\omega^{(o)}$, the velocity and stress measures $((1+\eta_r)\tilde{V}_\theta/\beta^4)$ and $((1+\eta_r)\tilde{\Sigma}_{\theta r}/\beta^4\eta_r)$ are functions of Re_ω. These are shown in figures 10 and 11. As predicted by (4.6) and (4.7), the magnitudes of $\tilde{V}_\theta|_{r=1}$ and $\tilde{\Sigma}_{\theta r}|_{r=1}$ tend to values independent of Re_ω and η_r for $Re_\omega \ll 1$, and the real parts are much larger than the imaginary parts. For $Re_\omega \gg 1$, the velocity measure in figure 10(*a*) decreases proportional to Re_ω^{-1}, the stress measure in figure 11(*a*) decreases proportional to $Re_\omega^{-1/2}$, and both these are independent of η_r for $Re_\omega^{(o)} = Re_\omega$. The velocity measure is imaginary for $Re_\omega \gg 1$ in figure 10(*b*), while the stress measure has real and imaginary parts consistent with (4.7). There is some variation in both the measures with η_r for intermediate values of Re_ω; while the magnitude of the velocity measure decreases monotonically for all values of η_r, the magnitude of the stress measure exhibits a maximum at an intermediate value of Re_ω.

The oscillatory drop deformation is characterised by the parameter $\tilde{h}_0$ defined in (2.31)–(2.33). This parameter is related to the normal stress difference across the drop by (2.67), where the pressure is evaluated from the θ momentum balance (2.56). Here, the forcing term $\tilde{F}_\theta$ turns out to be the dominant term in the momentum balance equation. This forcing term, evaluated in Appendix B, (B23), is $O(\beta^2)$ in the limit $\beta \ll 1$. In contrast,

https://doi.org/10.1017/jfm.2025.10176 Published online by Cambridge University Press

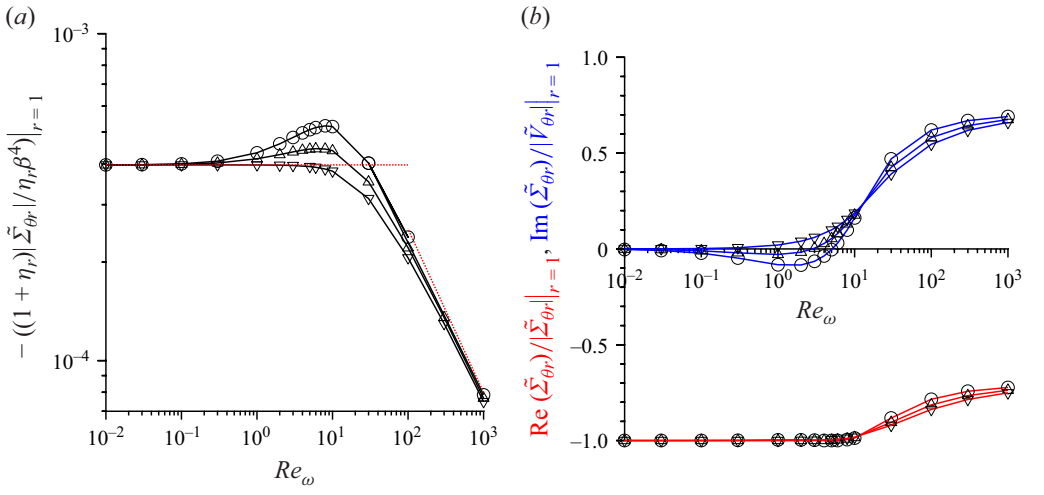


Figure 11. The measure (*a*) $-((1+\eta_r)|\tilde{\Sigma}_{\theta r}|_{r=1}/\eta_r\beta^4)$ and (*b*) $(\mathrm{Re}(\tilde{\Sigma}_{\theta r})/|\tilde{\Sigma}_{\theta r}|)|_{r=1}$ (red) and $(\mathrm{Im}(\tilde{\Sigma}_{\theta r})/|\tilde{\Sigma}_{\theta r}|)|_{r=1}$ (blue) as a function of Re_ω in the limit $\beta \ll 1$ for viscosity ratio $\eta_r \to 0$ (○), $\eta_r = 1.0$ (△), $\eta_r \to \infty$ (▽). The definition of $\tilde{\Sigma}_{\theta r}$ is given in (2.23). The dotted red line on the left in (*a*) is the $Re_\omega \ll 1$ asymptotic result (4.6). The dotted red line on the right in (*a*) is the $Re_\omega \gg 1$ asymptotic result (4.7).

$\tilde{g}^{(i)} \propto \beta^4$ (see discussion after (4.5)). Therefore, the dominant contribution to the pressure in the drop is due to the forcing $\tilde{F}_\theta$, and the $O(\beta^2)$ contribution to the pressure is evaluated by neglecting all terms except the pressure and $\tilde{F}_\theta$ in (2.56),

$$\tilde{P} = \frac{\imath\beta^2 r^2}{24}. \tag{4.8}$$

This is substituted into the stress balance across the interface, (2.67), to obtain

$$Ca^{-1}\tilde{h}_0 = -\frac{\imath\beta^2}{144}. \tag{4.9}$$

It should be emphasised that $\tilde{h}_0 \sim \beta^2$ in the limit $\beta \ll 1$, in contrast to the stream function and the velocity field which are $O(\beta^4)$. Thus, the oscillation of the drop is primarily due to pressure fluctuations which acts perpendicular to the surface, and the $O(\beta^2)$ contribution to the flow velocity in the drop is zero. The oscillation amplitude does not depend on Re_ω in the leading approximation in the limit $\beta \ll 1$.

4.3. *Limit* $\beta \gg 1$

The approximation (B26) is substituted into the (2.47) for $\tilde{g}^{(i)}$. The solution is the sum of a general solution of the homogeneous equation, $\tilde{g}_g^{(i)}$, which has the same form as the first term on the right-hand side in (4.5), and the particular solution. Since the force density (B26) is $O(1)$ in a region of thickness β^{-1} at the surface, the scaled variable is defined as $\xi = \beta(1-r)$. The equation (2.47) for $\tilde{g}_p^{(i)}$ is

$$0 = \beta^4 \frac{\mathrm{d}^4\tilde{g}_p^{(i)}}{\mathrm{d}\xi^4} - \frac{12\beta^2}{(1-\xi/\beta)^2}\frac{\mathrm{d}^2\tilde{g}_p^{(i)}}{\mathrm{d}\xi^2} - \frac{24\beta}{(1-\xi/\beta)^3}\frac{\mathrm{d}\tilde{g}_p^{(i)}}{\mathrm{d}\xi} + \tilde{\alpha}^2\left(\beta^2\frac{\mathrm{d}^2\tilde{g}_p^{(i)}}{\mathrm{d}\xi^2} - \frac{6\tilde{g}_p^{(i)}}{(1-\xi/\beta)^2}\right) - \left(\frac{9\beta(1+\imath)\exp\left[-\sqrt{2}(1+\imath)\xi\right]}{4\sqrt{2}(1-\xi/\beta)^2}\right). \tag{4.10}$$

https://doi.org/10.1017/jfm.2025.10176 Published online by Cambridge University Press

In the limit $\beta \gg 1$, the first and last terms on the right-hand side are the largest terms in the expansion. In the denominator of the last term on the right, $(\xi/\beta)^2$ is neglected in comparison with 1, and the equation is integrated to obtain

$$\begin{aligned}\tilde{g}_p^{(i)} &= -\frac{9(1+\imath)\exp\left(-\sqrt{2}(1+\imath)\xi\right)}{64\sqrt{2}\beta^3} \\ &= -\frac{9(1+\imath)\exp\left(-\sqrt{2}(1+\imath)\beta(1-r)\right)}{64\sqrt{2}\beta^3}.\end{aligned} \tag{4.11}$$

The sum of the general and particular solutions is

$$\begin{aligned}\tilde{g}^{(i)} = L\Big[&\sinh(\tilde{\alpha}r)\left(1+3(\tilde{\alpha}r)^{-2}\right) - 3(\tilde{\alpha}r)^{-1}\cosh(\tilde{\alpha}r) \\ &-r^3\left(\sinh(\tilde{\alpha})\left(1+3\tilde{\alpha}^{-2}\right) - 3\tilde{\alpha}^{-1}\cosh(\tilde{\alpha})\right)\Big] \\ &-\frac{9(1+\imath)\left[\exp\left(-\sqrt{2}(1+\imath)\beta(1-r)\right) - r^3\right]}{64\sqrt{2}\beta^3}.\end{aligned} \tag{4.12}$$

This solution satisfies the conditions (2.27) at $r = 0$ and the zero normal velocity condition (2.24) at $r = 1$.

The constant L is determined from the stress boundary condition, (2.54). The magnitude of L in the limit $\beta \gg 1$ is estimated as follows. The term on the right-hand side in (2.54) is independent of β. On the left-hand side, the second derivative $(\mathrm{d}^2\tilde{g}^{(i)}/\mathrm{d}r^2)$ in the numerator contains a contribution from the particular solution that is $O(\beta^{-1})$, and an $O(1)$ contribution from the general solution that is multiplied by L. The first derivative in the denominator on the left-hand side of (2.54) contains a contribution from the particular solution that is proportional to $O(\beta^{-2})$, and an $O(1)$ contribution from the general solution that is multiplied by L. From the balance between the left- and right-hand sides, it is inferred that $L \sim \beta^{-1}$ in the limit $\beta \gg 1$. Similarly, the coefficient D in the expression (2.51) for $\tilde{g}^{(o)}$ is also proportional to β^{-1} from the tangential stress balance condition. From this, the velocity and stress measures (2.16) and (2.23), are all proportional to β^{-1}.

The solution for $\tilde{g}^{(i)}$, (4.12), is substituted into the boundary condition (2.54), and r is set equal to 1 at the surface. The constant L is expressed as $L_0\beta^{-1}$, and only the $O(\beta^{-1})$ terms are retained in the resulting boundary condition to obtain L_0. This is then substituted into equation the solution (2.27) to determine the $O(\beta^{-1})$ contribution to $\tilde{g}^{(i)}$ and its first and second derivatives. These are then used to determine the velocity fields.

Vector plots of the real and imaginary parts of $\tilde{\boldsymbol{v}}$ for $\beta \gg 1$ are shown in figures 12(*a–c*) and 12(*d–f*). For $Re_\omega = 1$, the flow is expected to be quasisteady and the real and imaginary parts of the velocity vector are in phase with the forcing. Since the particular solution in (4.11) is complex with real and imaginary parts of equal magnitude, the solution for $\tilde{\boldsymbol{v}}$ has real and imaginary parts of equal magnitude and opposite sign. It should also be noted that the forcing is restricted to a thin region of thickness β^{-1} at the surface in the limit $\beta \gg 1$. This forcing causes a flow throughout the drop in the limit $Re_\omega \ll 1$ due to the quasisteady nature of momentum diffusion.

For $Re_\omega = 1000$, figure 12(*c,f,i*) shows that the flow is restricted to a thin region near the surface of the drop for two reasons. Firstly, the forcing in (4.11) is restricted to a thin region of thickness β^{-1} at the surface. Secondly, the diffusion length for momentum, $(\eta_i/\rho_i\omega)^{1/2}$, is much smaller than the radius of the drop for $Re_\omega \gg 1$. Due to this, momentum diffusion is restricted to a thin region at the surface in a manner similar to that for the Stokes oscillatory boundary layer. This results in a sharp variation in the tangential

https://doi.org/10.1017/jfm.2025.10176 Published online by Cambridge University Press

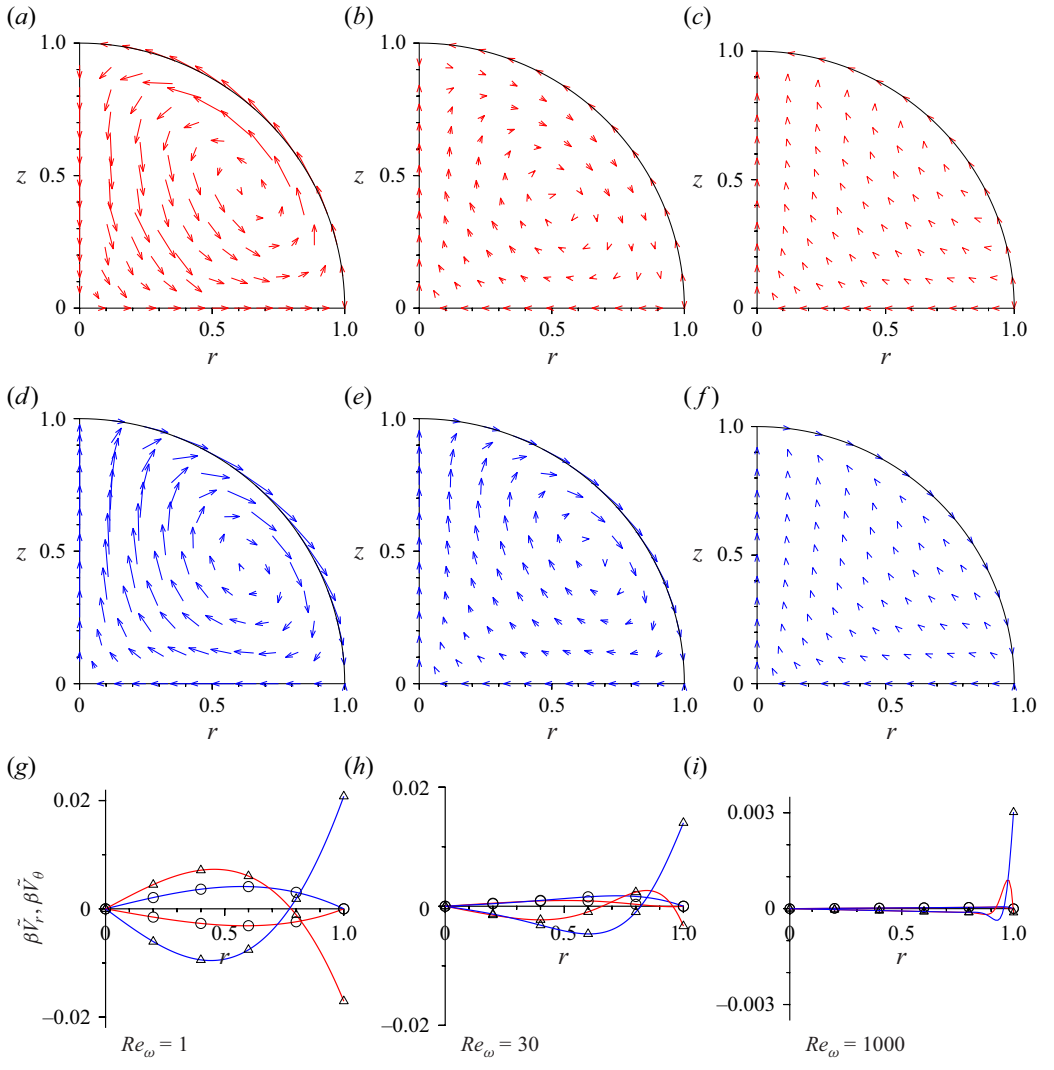


Figure 12. Vector plots of the real part (*a–c*) and imaginary part (*d–f*) of the velocity vectors and the velocity measures $\beta\tilde{V}_r = \beta\tilde{v}_r/(3\cos(\theta)^2 - 1)$ ((2.16), red line) and $\beta\tilde{V}_\theta = \beta\tilde{v}_\theta/(\sin(\theta)\cos(\theta))$ ((2.16), △) in the limit $\beta \gg 1$, for $\eta_r = 1$ and for three different values of Re_ω. The real parts are shown by the red lines, and the imaginary parts are shown by the blue lines.

and normal velocity at the surface observed in figure 12(*i*). The imaginary part of the velocity $\tilde{\boldsymbol{v}}$ is much larger than the real part in this case.

The oscillatory parts of the tangential velocity measure $\tilde{V}_\theta$ (2.16) and stress measure $\tilde{\Sigma}_{\theta r}$ (2.23) at the surface $r = 1$ are evaluated analytically in the limits $Re_\omega \ll 1$ and $Re_\omega \gg 1$. In the limit $Re_\omega \ll 1$,

$$\tilde{V}_\theta\Big|_{r=1} = \frac{\tilde{v}_\theta}{\sin(\theta)\cos(\theta)}\bigg|_{r=1} = -\frac{9(1-\imath)}{80\sqrt{2}\beta(1+\eta_r)},$$
$$\tilde{\Sigma}_{\theta r}\Big|_{r=1} = \frac{\tilde{\sigma}_{\theta r}}{\sin(\theta)\cos(\theta)}\bigg|_{r=1} = \frac{9(1-\imath)\eta_r}{16\sqrt{2}\beta(1+\eta_r)}. \tag{4.13}$$

https://doi.org/10.1017/jfm.2025.10176 Published online by Cambridge University Press

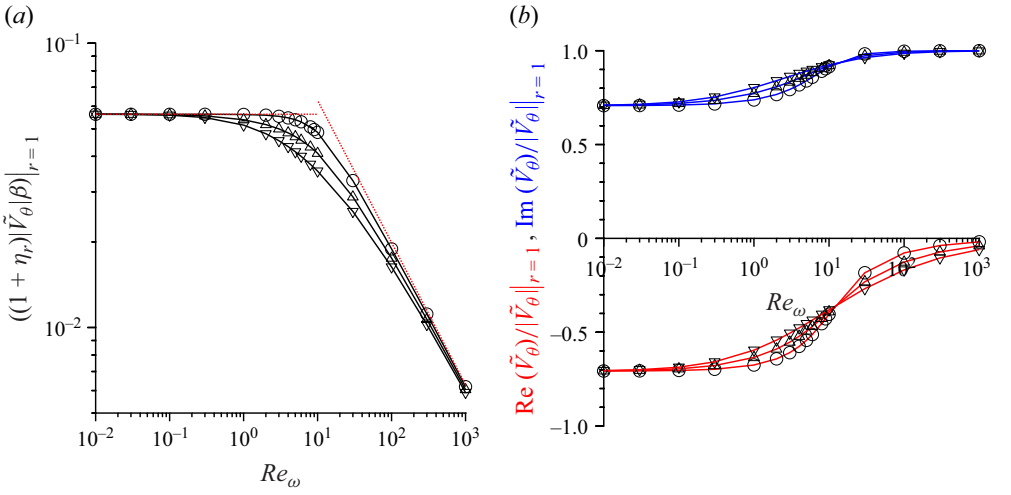


Figure 13. The measure (*a*) $((1+\eta_r)\beta|\tilde{V}_\theta|_{r=1})$ and (*b*) $\mathrm{Re}(\tilde{V}_\theta)/|\tilde{V}_\theta\|_{r=1}$ (red) and $\mathrm{Im}(\tilde{V}_\theta)/|\tilde{V}_\theta|$ (blue) as a function of β for viscosity ratio $\eta_r \to 0$ ($\circ$), $\eta_r = 1.0$ ($\triangle$), $\eta_r \to \infty$ (∇). The definition of $\tilde{V}_\theta$ is given in (2.16). The dotted red line on the left in (*a*) is the $Re_\omega \ll 1$ asymptotic result (4.13). The dotted red line on the right in (*a*) is the $Re_\omega \gg 1$ asymptotic result (4.14).

In the limit $Re_\omega \gg 1$, the velocity and stress measures are

$$\tilde{V}_\theta\Big|_{r=1} = \frac{9\iota}{16\sqrt{2}\beta\left(1+\eta_r\sqrt{Re_\omega^{(o)}/Re_\omega}\right)\sqrt{Re_\omega}},$$
$$\tilde{\Sigma}_{\theta r}\Big|_{r=1} = \frac{9(1-\iota)\eta_r\sqrt{Re_\omega^{(o)}/Re_\omega}}{16\sqrt{2}\beta\left(1+\eta_r\sqrt{Re_\omega^{(o)}/Re_\omega}\right)}. \tag{4.14}$$

Equation (4.13) shows that the velocity and stress measures are independent of Re_ω for $Re_\omega \ll 1$. In the limit $Re_\omega \gg 1$, the stress measure is independent of Re_ω, but the velocity measure decreases proportional to $Re_\omega^{-1/2}$. This is as expected for the Stokes oscillatory boundary layer driven by a fixed stress amplitude at the interface instead of a fixed velocity.

The measures $((1+\eta_r)\beta\tilde{V}_\theta)$ and $((1+\eta_r)\beta\tilde{\Sigma}_{\theta r}/\eta_r)$ are shown as a function of Re_ω in figures 13 and 14. Here, we have set $Re_\omega^{(o)} = Re_\omega$. The magnitude of the scaled velocity measure tends to a constant value that is independent of η_r for $Re_\omega \ll 1$, and it decreases proportional to $Re_\omega^{-1/2}$ for $Re_\omega \gg 1$. The results in figure 13 are in agreement with asymptotic results, (4.13) and (4.14). The scaled stress measure in figure 14 tends to the same constant value, independent of η_r, for both $Re_\omega \ll 1$ and $Re_\omega \gg 1$. The velocity and stress measures exhibit variation with η_r over a narrow range for intermediate values of Re_ω.

There is a non-monotonic variation of the tangential stress measures with Re_ω, but not the tangential velocity measures. The stress scales as the ratio of the tangential velocity and the penetration depth of the magnetic field into the fluid. In the limit $Re_\omega \ll 1$, figures 10 and 13 show that the scaled velocity approaches a constant, and the characteristic length is the drop radius, so the stress approaches a constant. In the limit $Re_\omega \gg 1$, the penetration depth is proportional to $Re_\omega^{-1/2}$, which is similar to the Stokes second problem for an oscillating boundary layer. The velocity in the limit $\beta \ll 1$ in figure 10

https://doi.org/10.1017/jfm.2025.10176 Published online by Cambridge University Press

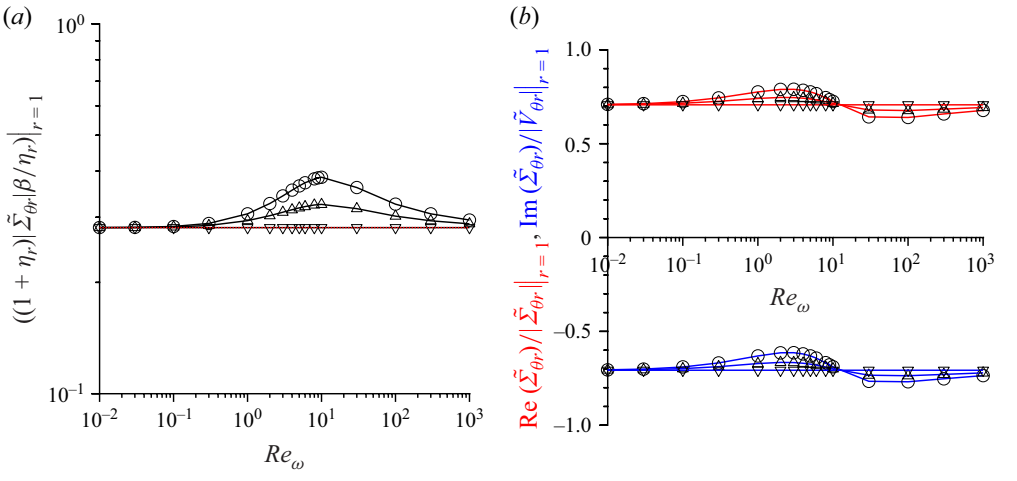


Figure 14. The measure (*a*) $((1+\eta_r)|\tilde{\Sigma}_{\theta r}|\beta/\eta_r)|_{r=1}$ and (*b*) $(\tilde{\Sigma}_{\theta r})/|\tilde{\Sigma}_{\theta r}||_{r=1}$ and $\mathrm{Im}(\tilde{\Sigma}_{\theta r})/|\tilde{\Sigma}_{\theta r}|$ as a function of Re_ω in the limit $\beta \ll 1$ for viscosity ratio $\eta_r = 0$ (○), $\eta_r = 1.0$ (△), $\eta_r \to \infty$ (▽). The definition of $\tilde{\Sigma}_{\theta r}$ is given in (2.23). The dotted red line on the left in (*a*) is the $Re_\omega \ll 1$ asymptotic result (4.13). The dotted red line on the right is the $Re_\omega \gg 1$ asymptotic result (4.14).

decreases proportional to Re_ω^{-1}, and therefore the stress in figure 11 decreases proportional to $Re_\omega^{-1/2}$. Similarly, in the limit $\beta \gg 1$, the velocity in figure 13 decreases proportional to $Re_\omega^{-1/2}$ for $Re_\omega \gg 1$, and therefore the stress approaches a constant value in figure 14. The stress exhibits a non-monotonic behaviour for intermediate values of Re_ω. This is because the tangential velocity decreases more slowly than the penetration depth as Re_ω is increased, resulting in an initial increase in the stress. This is followed by a decrease in the stress to a constant in the $Re_\omega \gg 1$ asymptotic regime.

The parameter $\tilde{h}_0$ (2.31)–(2.33) that characterises the oscillatory drop deformation is evaluated from the normal stress balance across the drop, (2.67). In the expression (2.59) for the normal stress within the drop, the largest term is the first term on the right-hand side, $(1/6)(\mathrm{d}^3\tilde{g}^{(i)}/\mathrm{d}r^3)$. In the (4.12) for $\tilde{g}^{(i)}$ in the limit $\beta \gg 1$, the first term on the right-hand side is $O(\beta^{-1})$ because L is $O(\beta^{-1})$ (see discussion after (4.12)), while the second term on the right-hand side is $O(\beta^{-3})$. In the expression for the third derivative, the derivative of the first term (proportional to L) is $O(\beta^{-1})$, whereas the third derivative of the second term on the right-hand side in (4.12) is $O(1)$. Therefore, the dominant contribution to the normal stress (2.59) is the $O(1)$ contribution due to the second term on the right-hand side in (4.12). The expression for the stress outside the drop depends on $\tilde{g}^{(o)}$ (2.52), and the constant D in this equation is $O(\beta^{-1})$ (see discussion after (4.12)). From the approximation (B24), the contribution due to $\tilde{F}_\theta$ on the right-hand side of (2.59) is also $O(1)$ in the limit $\beta \gg 1$. Therefore, the largest contribution to the interfacial normal stress balance is due to the third derivative of the particular solution $\tilde{g}_p^{(i)}$ and the Lorentz force within the drop,

$$\left(\frac{1}{6}\frac{\mathrm{d}^3\tilde{g}_p^{(i)}}{\mathrm{d}r^3} + \frac{r\tilde{F}_\theta}{6}\right)\bigg|_{r=1} = 6Ca^{-1}\tilde{h}_0. \tag{4.15}$$

Substituting the expression (4.11) for $\tilde{g}_p^{(i)}$ and (B24) for $\tilde{F}_\theta$, we obtain

$$Ca^{-1}\tilde{h}_0 = -\frac{1}{32}. \tag{4.16}$$

https://doi.org/10.1017/jfm.2025.10176 Published online by Cambridge University Press

R (mm)	$(\omega/2\pi)$ (Hz)	β	B_0 (T)	$(\bar{V}_\theta^\dagger\|_{r=1}/R)$ (s^{-1})	Re	Re_ω	$\bar{V}_\theta\|_{r=1}Ca$	$(\bar{Q}/V)$ W/m^3	ΔT K
0.1	4.7×10^7	6.1	10^{-3}	5.0	0.05	4.7×10^5	5×10^{-6}	4.7×10^7	0.26
			10^{-2}	500.0	5.0	4.7×10^5	5×10^{-4}	4.7×10^9	26
1.0	4.7×10^5	6.1	10^{-3}	5.0	5.0	4.7×10^5	5×10^{-5}	4.7×10^5	0.26
			10^{-2}	500.0	500.0	4.7×10^5	5×10^{-3}	4.7×10^7	26
0.1	10^5	0.28	10^{-2}	3.9×10^{-2}	3.9×10^{-4}	10^3	3.9×10^{-8}	2.0×10^5	1.1×10^{-3}
			10^{-1}	3.9	3.9×10^{-2}	10^3	3.9×10^{-6}	2.0×10^7	1.1×10^{-1}
1.0	10^4	0.89	10^{-3}	3.9×10^{-2}	3.9×10^{-2}	10^4	3.9×10^{-7}	2.0×10^3	1.1×10^{-3}
			10^{-2}	3.9	3.9	10^4	3.9×10^{-5}	2.0×10^5	1.1×10^{-1}

Table 2. The parameter β, the characteristic strain rate $(\bar{V}_\theta^\dagger|_{r=1}/R)$ for different combinations of the drop radius R, cyclical frequency $(\omega/2\pi)$ and magnetic flux density B_0. The dimensionless groups are $Re=(\rho\bar{V}_\theta^\dagger|_{r=1}R/\eta_i)$, the Reynolds number $Re_\omega=(\rho\omega R^2/\eta_i)$ based on the frequency of oscillations and the capillary number based on the tangential velocity measure $\bar{V}_\theta|_{r=1}Ca=(\eta_i\bar{V}_\theta^\dagger|_{r=1}/\gamma)$. For all cases, the electrical conductivity is $\kappa=10^7$S/m, the viscosity of the drop is $\eta_i=10^{-3}$ kg ms^{-1}, the surface tension is $\gamma=0.1$ kg s^{-2}, the ratio of viscosities is $\eta_r=1$, the density is 10^3 kg/m^3 and the magnetic permeability is $\mu_0=4\pi\times10^{-7}$ kg m^{2}s^{-2}A^{-2}. For the calculation of ΔT, the thermal conductivity of the ambient fluid is assumed to be 0.6 W mK^{-1}.

5. Applications

The parameter values required to drive a discernible steady flow in a droplet in practical applications are first estimated. For reference, the magnetic field strength is usually expressed in terms of the magnetic flux density, $B_0=\mu_0H_0$, with SI unit tesla. Small bar magnets can generate magnetic flux density of 10^{-3}T, Helmholtz coils can generate flux density in the range $10^{-2}-10^{-1}$T, but large laboratory magnets are required for flux density 1T or greater. Therefore, the magnetic flux density in the range $10^{-3}-10^{-1}$T is considered here. The range of frequencies that can be practically achieved in Helmholtz coils is limited by the resonant frequency, which can be up to 100 kHz or 1 MHz. The electrical conductivity of metals is in the range 10^6-10^7 S m^{-1}. Though liquid superconductors have been proposed (Edwards *et al.* 2006), they have not yet been realised in practice. Therefore, the calculations that follow are carried out for $\kappa=10^7$ S m^{-1}. The viscosity of liquid metals is comparable with the viscosity of water, approximately 10^{-3} kg ms^{-1}. Therefore, we consider $\eta_i=\eta_o=10^{-3}$ kg ms^{-1} in the following calculations. The magnetic permeability of non-magnetic materials is close to that of vacuum, $\mu_0=4\pi\times10^{-7}$ kg m^{2}s^{-2} A^{-2}. The numerical estimates are summarised in table 2

The velocity and stress measures for a steady flow, figures 5(*a*) and 5(*b*), are maximum at $\beta=\sqrt{\mu_0\kappa\omega R^2}\sim6.1$. It would be optimal to drive the flow at this value of β. For drops of size 0.1 mm, $\beta=6$ for cyclical frequency $(\omega/2\pi)=45$ MHz, which is in excess of the range of magnetic field frequencies in practical applications. Since the frequency decreases proportional to R^{-2} for fixed β, for drops of size 1 mm, $\beta=6.1$ for cyclical frequency $(\omega/2\pi)=0.45$ MHz. This is at the upper end of the feasible frequency range. The characteristic velocity at $\beta\sim6.1$ can be considered as $V_\theta|_{r=1}=(1.25\times10^{-2}/(1+\eta_r))$ from figure 5. The dimensional velocity is $V_\theta^\dagger=(\mu_0H_0^2R/\eta_i)(1.25\times10^{-2}/(1+\eta_r))$. The characteristic strain rate, the ratio of the velocity and the radius, is $(V_\theta^\dagger/R)=1.25\times10^{-2}(\mu_0H_0^2/\eta_i(1+\eta_r))$. If we assume that $\eta_i=10^{-3}$ kg/m/s and $\eta_r=1$, the characteristic strain rate is $5\,s^{-1}$ for magnetic flux density $B_0=\mu_0H_0=10^{-3}$T, and $500\,s^{-1}$ for

https://doi.org/10.1017/jfm.2025.10176 Published online by Cambridge University Press

$B_0 = 10^{-2}$T. Thus, relatively high strain rates can be achieved in 1 mm drops even with low magnetic fields, provided the magnetic field frequency is sufficiently high.

If we operate in the low β regime, the velocity measure $V_\theta|_{r=1}$ (3.16) is proportional to β^4. The dimensional strain rate is $(V_\theta^\dagger/R) = (\beta^4/6300(1+\eta_r))(B_0^2/\mu_0\eta_i)$ (see (3.16)). If we consider drops of radius 0.1mm subject to a field with frequency 100 kHz, the parameter β is 0.28, the strain rate is 3.9×10^{-2} s^{-1} for $B_0 = 10^{-2}$T. If B_0 is increased to 0.1T, the strain rate is 3.9 s^{-1}. The same range of strain rates are obtained if the radius is increased by a factor of 10, $R = 1$mm, and the cyclical frequency is decreased by a factor of 10, $(\omega/2\pi) = 10$ kHz. Thus, for drops of diameter 100μm, strain rates of the order of 1 s^{-1} require relatively large magnetic fields of the order 0.1T and frequency of 100kHz, whereas large strain rates can be generated in 1mm drops with reasonable combination of a magnetic field of 0.01T and frequency 10 kHz.

An important assumption in the analysis is that the nonlinear convective term in the momentum conservation equation is small compared with the viscous term. The ratio of the convective and viscous terms is the Reynolds number, $\mathrm{Re} = (\rho \bar{V}_\theta^\dagger|_{r=1} R/\eta_i)$ based on the characteristic velocity $\bar{V}_\theta^\dagger|_{r=1}$. This Reynolds number is shown in the fifth column in table 2. The Reynolds number is found to be small for all the parameters examined here, with the exception of the flow in a 1mm drop at a large frequency of 4.5×10^5 Hz and magnetic flux density 10^{-2}T, where the Reynolds number is 500. In all other cases, where the strain rate is of the order of 1 s^{-1} or less, the Reynolds number is small, and the nonlinear convective term in the momentum conservation equation can be neglected in comparison with the viscous term.

It should be noted that the Reynolds number Re based on the flow velocity is different from Re_ω based on the frequency of oscillations. The latter, which is shown in the sixth column of table 2, is large for the range of parameters considered here, due to the high oscillation frequency required to drive the flow. Therefore, the $Re_\omega \gg 1$ asymptotic results in § § 4.2 and (4.3) are relevant for the parameter range considered here.

Another important assumption is that the drop shape is not affected by the flow. The ratio of viscous and surface tension forces is the capillary number based on the surface velocity measure, $\bar{V}_\theta|_{r=1} Ca = (\eta_i \bar{V}_\theta^\dagger|_{r=1}/\gamma)$. Here, we have multiplied the capillary number by $\bar{V}_\theta|_{r=1}$, because figure 5 shows that the latter is numerically small. This dimensionless group, based on the estimate 0.1 kg s^{-2} for the surface tension, is shown in the seventh column in table 2. The capillary number is always small for the drop dimensions considered here, and a spherical shape is a good approximation for drops of radius 1mm or less.

A concern in employing eddy currents to generate flow is the heat generation. The rate of Joule heating is $\bar{Q}^\dagger = \bar{Q}(H_0^2 R/\kappa)$, where $\bar{Q}$ is given by (3.30). The heating rate per unit volume, $(\bar{Q}^\dagger/V)$, is shown in the eighth column in table 2. This is the heating rate per unit volume of the drop, and this is multiplied by the volume fraction of the drops to determine the heating rate per unit volume of the suspension. Another estimate of the Joule heating rate can be determined from the difference in temperature between the drop and the ambient due to the heating. If heat transfer in the ambient fluid is due to conduction, the rate of heat transfer from the drop is related to the temperature difference ΔT between the drop and the ambient, $(\bar{Q}^\dagger/4\pi k) = \Delta T R$, where k is the thermal conductivity of the ambient fluid. Therefore, the temperature difference can be expressed as $\Delta T = (\bar{Q} H_0^2/(4\pi k \kappa))$, where $\bar{Q}$ is plotted in figure 7. The conductivity of water, $k = 0.6$W/m/K is assumed for the estimation. The increase in temperature is shown in the ninth column in table 2. It is observed that for $\beta = 6.1$ where the characteristic

https://doi.org/10.1017/jfm.2025.10176 Published online by Cambridge University Press

velocity is a maximum, there is significant heating, and the drop temperature could be tens of degrees higher than the ambient. For lower values of β, the drop temperature exceeds the ambient by less than $1K$.

6. Conclusions

The present analysis shows that flows with significant strain rate can be generated in conducting drops due to an oscillating magnetic field of reasonable flux density, provided the frequency of oscillation is sufficiently large. The magnitude of the velocity is $(\mu_0 H_0^2 R/\eta_i)$ times a function of the dimensionless parameter $\beta = \sqrt{\mu_0 \kappa \omega R^2}$, which is the square root of the ratio of the magnetic field frequency and the current relaxation rate over a length R. The magnitudes of the velocity and the stress decrease proportional to β^4 for $\beta \ll 1$, and proportional to β^{-1} for $\beta \gg 1$. There is an intermediate value of β at which the velocity and stress are a maximum. The physical reason for these scalings is as follows. In the limit $\beta \ll 1$, the magnetic field penetrates the drop over a time scale small compared with the period of oscillation. From a regular perturbation analysis, the correction to the magnetic field due to the conductivity contrast of the drop is proportional to β^2, the ratio of the time scale for penetration of the field and the period of oscillation. The correction to the electric field is also proportional to β^2, since it is proportional to the time-varying part of the magnetic field. Therefore, the Lorentz force density and the magnitude of the velocity are proportional to β^4. For $\beta \gg 1$, the time for magnetic field penetration is large compared with the period of oscillation. The magnetic field penetration is restricted to a layer of thickness β^{-1} at the surface of the drop. The scaled electric field is β times the scaled magnetic field in the skin layer, because the electric field is the curl of the magnetic field. The force density, that is proportional to the cross product of the electric and magnetic field, is $O(\beta)$ within the skin layer. Since the curl of the force density is balanced by the fourth derivative of the stream function with respect to the coordinate normal to the surface, the particular solution for the stream function is $O(\beta^{-3})$ within the skin layer. This forcing in the skin layer drives a flow in the bulk of the drop. To satisfy the boundary conditions, we find that the homogeneous solution is proportional to $O(\beta^{-1})$. Therefore, the velocity and stress magnitudes are proportional to β^{-1} in the limit $\beta \gg 1$.

Universal relations were obtained for the velocity and stress measures for the steady flow, $\bar{V}_\theta$ and $\bar{\Sigma}_{\theta r}$ at the surface, which are independent of the ratio of viscosities η_r. These are shown in figure 5, and analytical expressions in the limits $\beta \ll 1$ and $\beta \gg 1$ are given in (3.16) and (3.23). The velocity and stress measures for the oscillating component of the flow, $\tilde{V}_\theta$ and $\tilde{\Sigma}_{\theta r}$, also depend on the Reynolds number Re_ω based on the magnetic field frequency. These measures were calculated using analytical expressions for the Lorentz force density in the limits $\beta \ll 1$ and $\beta \gg 1$. Universal relations can be obtained for these measures in the limits $Re_\omega \ll 1$ and $Re_\omega \gg 1$, as indicated by the asymptotic expressions (4.6)–(4.7) and (4.13)–(4.14). However, the measures do depend on β for intermediate Re_ω, as shown in figures 10, 11 ,13and 14.

The deformation of the drop has been estimated in the limit of low capillary number. Here, the velocity field for a spherical drop is used to calculate the variation in the normal stress along the surface, and the deformation of the drop due to the normal stress variation is determined. The steady component of the deformation is proportional to $(3\cos(\theta)^2 - 1)$, which is the axisymmetric spherical harmonic $Y_2^0(\theta, \phi)$. The coefficient of this harmonic, $\bar{h}_0$ is negative, implying that the sphere deforms into an oblate spheroid due to the mean flow. Figure 6 shows that $-Ca^{-1}\bar{h}_0$ increases proportional to β^4 for $\beta \ll 1$, and it approaches a constant for $\beta \gg 1$. The steady deformation exhibits very little variation with the viscosity contrast η_r.

https://doi.org/10.1017/jfm.2025.10176 Published online by Cambridge University Press

The resonant modes of oscillation of the drop have also been determined. The oscillatory surface displacement is proportional to $(3\cos(\theta)^2 - 1)\exp(2\imath t)$, and the complex coefficient $\tilde{h}_0$ has been evaluated in the limits $\beta \ll 1$ and $\beta \gg 1$. In the limit $\beta \ll 1$, the pressure normal to the surface and the surface deformation scales as β^2 (4.8)–(4.9). This is much larger than the velocity, which scales as β^4. Thus, surface motion is primarily driven by pressure oscillations and not by the flow. It is found that $Ca^{-1}\tilde{h}_0$ is imaginary, indicating that the oscillation amplitude is proportional to $\sin(2\imath t)$ in this limit. In the limit $\beta \gg 1$, the pressure and the Lorentz force are $O(1)$, while the velocity fields are $O(\beta^{-1})$. Therefore, the oscillations are driven primarily by the pressure and Lorentz force, and $Ca^{-1}\tilde{h}_0$ tends to a constant real value given by the result (4.16). The amplitude of the drop oscillations is proportional to $\cos(2\imath t)$ in this limit. Thus, simple asymptotic expressions have been obtained for the amplitude of oscillation of the drops in the limits $\beta \ll 1$ and $\beta \gg 1$; the drop oscillations are independent of Re_ω in both of these limits. The amplitude of oscillations will depend on Re_ω for intermediate values of β; this is a subject for further study.

Since the flow is axisymmetric and symmetric about the equatorial plane, there is no net force on the drop, and consequently no translation. However, there is a symmetric force dipole, a particle stress, which is induced. This results in long-range fluid velocity fluctuations which can be used for mixing and enhancing transport due to diffusion. In the presence of boundaries or other drops, there is the prospect of translational motion due to interactions. In the context of ferromagnetic particles in a magnetic field, it has been shown (Kumaran 2022) that interactions result in concentration amplification in certain directions. The effect of interactions can be expressed as an anisotropic diffusion tensor, with negative diffusivity in directions along which the concentration is amplified. A similar effect is likely to be observed in the present case as well. There is also the prospect of observing phenomena reported in the collective behaviour of active matter, where the particles exert a force dipole on the fluid.

The nonlinear term in the momentum conservation equation is neglected in the present analysis, and therefore it is valid only in the limit where the Reynolds number based on the velocity within the drop is small. For drops larger than approximately 1 mm, the Reynolds number is likely to be large, and it would be of interest to examine the modification of the velocity field due to inertial effects. Only the first correction to the shape of the drop has been considered here in the low capillary limit, using the flow field in a spherical drop. More work is required to consider the effect of deformation on the flow dynamics, and to examine phenomena such as drop breakup and coalescence by an oscillating magnetic field.

Funding. This work was supported by funding from the MHRD and the Science and Engineering Research Board, Government of India (grant no. SR/S2/JCB-31/2006) and Synopsys.

Declaration of interests. There are no conflicts to declare.

Appendix A. Magnetic and electric fields

The equations for the electric and magnetic fields in a neutral medium are expressed in dimensionless form using the non-dimensionalisation in table 1,

$$\nabla \cdot \boldsymbol{E} = 0, \quad \nabla \times \boldsymbol{E} = -\beta^2 \frac{\partial \boldsymbol{H}}{\partial t}, \tag{A1}$$

$$\nabla \cdot \boldsymbol{H} = 0, \quad \nabla \times \boldsymbol{H} = \boldsymbol{J} + \frac{\epsilon\omega}{\kappa}\frac{\partial \boldsymbol{E}}{\partial t}, \tag{A2}$$

https://doi.org/10.1017/jfm.2025.10176 Published online by Cambridge University Press

where $\beta = \sqrt{\mu_0 \omega \kappa R^2}$ is the ratio of the frequency of the magnetic field oscillation and the current relaxation rate. The ratio $(\epsilon\omega/\kappa)$ is small for an electrical conductor, and so the second term on the right-hand side is neglected in comparison with the first in (A2) for the curl of the magnetic field.

For an oscillating field, we substitute

$$\begin{aligned} \boldsymbol{H} &= \tfrac{1}{2}(\tilde{\boldsymbol{H}} \exp(\imath t) + (\tilde{\boldsymbol{H}} \exp(\imath t))^*), \\ \boldsymbol{E} &= \tfrac{1}{2}(\tilde{\boldsymbol{E}} \exp(\imath t) + (\tilde{\boldsymbol{E}} \exp(\imath t))^*), \end{aligned} \tag{A3}$$

where $\imath = \sqrt{-1}$, and * denotes the complex conjugate. Note that $t = \omega t^\dagger$ is time scaled by ω^{-1}, where $t^\dagger$ is the dimensional time. The magnetic field far from the drop, scaled by its amplitude H_0, is

$$\boldsymbol{H}_0 = \hat{\boldsymbol{H}} \cos(t) = \tfrac{1}{2}\hat{\boldsymbol{H}}(\exp(\imath t) + \exp(-\imath t)), \tag{A4}$$

where $\hat{\boldsymbol{H}}$ is the (constant) unit vector along the magnetic field direction, which is the axial $\hat{\boldsymbol{e}}_z$ direction in figure 1.

The current density is expressed in terms of the electric field in (A2), using Ohm's law, $\tilde{\boldsymbol{J}} = \tilde{\boldsymbol{E}}$ in scaled form,

$$\nabla \times \tilde{\boldsymbol{H}} = \tilde{\boldsymbol{E}}. \tag{A5}$$

An equation for $\tilde{\boldsymbol{H}}$ is obtained by taking the curl of the above equation, and substituting (A1) for $\nabla \times \boldsymbol{E}$,

$$\nabla \times \nabla \times \tilde{\boldsymbol{H}} = \nabla(\nabla \cdot \tilde{\boldsymbol{H}}) - \nabla^2 \tilde{\boldsymbol{H}} = -\imath\beta^2 \tilde{\boldsymbol{H}}. \tag{A6}$$

Since the divergence of the magnetic field is zero, the equation for $\tilde{\boldsymbol{H}}$ is

$$\nabla^2 \tilde{\boldsymbol{H}} = \imath\beta^2 \tilde{\boldsymbol{H}}. \tag{A7}$$

The magnetic field can be expressed as $\tilde{\boldsymbol{H}} = \nabla \times \tilde{\boldsymbol{A}}$ so that the zero-divergence condition (A2) is identically satisfied. The magnetic potential $\tilde{\boldsymbol{A}}$ is a real vector (the direction does not reverse upon inversion between right- and left-handed coordinates) which depends only on the pseudovector $\hat{\boldsymbol{H}}$. (The direction reverses upon inversion between right- and left-handed coordinates.) Therefore, the magnetic field can be expressed as $\tilde{\boldsymbol{A}} = \tilde{A}\nabla \times (\tilde{\chi}(r))\hat{\boldsymbol{H}}$, where $\tilde{A}$ is a complex constant and $\tilde{\chi}(r)$ is the spherically symmetric solution of the Helmholtz equation,

$$\nabla^2 \tilde{\chi} + \tilde{\beta}^2 \tilde{\chi} = 0, \tag{A8}$$

where $\tilde{\beta} = \sqrt{-\imath}\beta$. The solution for $\tilde{\chi}$ that is finite at the centre of the drop is

$$\tilde{\chi}(r) = \frac{\sin(\tilde{\beta} r)}{r}. \tag{A9}$$

The solution for the magnetic field in the conducting drop is

$$\tilde{\boldsymbol{H}} = \tilde{A}\nabla \times \nabla \times (\tilde{\chi}(r)\hat{\boldsymbol{H}}) = \tilde{A}[\nabla\nabla \cdot (\tilde{\chi}(r)\hat{\boldsymbol{H}}) - \nabla^2(\tilde{\chi}(r)\hat{\boldsymbol{H}})]. \tag{A10}$$

Since the function $\tilde{\chi}$ satisfies (A8), the second derivative $(\mathrm{d}^2\tilde{\chi}/\mathrm{d}r^2)$ is expressed in terms of $(\mathrm{d}\tilde{\chi}/\mathrm{d}r)$ and $\tilde{\chi}$ as

$$\frac{\mathrm{d}^2\tilde{\chi}}{\mathrm{d}r^2} = -\frac{2}{r}\frac{\mathrm{d}\tilde{\chi}}{\mathrm{d}r} - \tilde{\beta}^2\tilde{\chi}. \tag{A11}$$

https://doi.org/10.1017/jfm.2025.10176 Published online by Cambridge University Press

The term $\boldsymbol{\nabla\nabla}\cdot(\tilde{\chi}\hat{\boldsymbol{H}})$ in (A10) is simplified using indicial notation as

$$\begin{aligned}\boldsymbol{\nabla\nabla}\cdot(\tilde{\chi}(r)\hat{\boldsymbol{H}}) &= \frac{\partial}{\partial x_i}\left(\frac{\partial\tilde{\chi}(r)}{\partial x_j}\right)\hat{H}_j = \frac{\partial}{\partial x_i}\left(\frac{x_j}{r}\frac{\mathrm{d}\tilde{\chi}}{\mathrm{d}r}\right)\hat{H}_j \\ &= \left(\frac{\delta_{ij}}{r}\frac{\mathrm{d}\tilde{\chi}}{\mathrm{d}r} - \frac{x_i x_j}{r^3}\frac{\mathrm{d}\tilde{\chi}}{\mathrm{d}r} + \frac{x_i x_j}{r^2}\frac{\mathrm{d}^2\tilde{\chi}}{\mathrm{d}r^2}\right)\hat{H}_j \\ &= \frac{\hat{H}_i}{r}\frac{\mathrm{d}\tilde{\chi}}{\mathrm{d}r} - \frac{x_i x_j \hat{H}_j}{r^3}\frac{\mathrm{d}\tilde{\chi}}{\mathrm{d}r} + \frac{x_i x_j \hat{H}_j}{r^2}\frac{\mathrm{d}^2\tilde{\chi}}{\mathrm{d}r^2}. \end{aligned} \tag{A12}$$

This is expressed in vector notation as

$$\begin{aligned}\boldsymbol{\nabla\nabla}\cdot(\tilde{\chi}(r)\hat{\boldsymbol{H}}) &= \frac{\hat{\boldsymbol{H}}}{r}\frac{\mathrm{d}\tilde{\chi}}{\mathrm{d}r} + \left(-\frac{1}{r^3}\frac{\mathrm{d}\tilde{\chi}}{\mathrm{d}r} + \frac{1}{r^2}\left(-\frac{2}{r}\frac{\mathrm{d}\tilde{\chi}}{\mathrm{d}r} - \tilde{\beta}^2\tilde{\chi}\right)\right)\boldsymbol{x}(\boldsymbol{x}\cdot\hat{\boldsymbol{H}}) \\ &= \frac{\hat{\boldsymbol{H}}}{r}\frac{\mathrm{d}\tilde{\chi}}{\mathrm{d}r} + \left(-\frac{3}{r}\frac{\mathrm{d}\tilde{\chi}}{\mathrm{d}r} - \tilde{\beta}^2\tilde{\chi}\right)\hat{\boldsymbol{x}}(\hat{\boldsymbol{x}}\cdot\hat{\boldsymbol{H}}), \end{aligned} \tag{A13}$$

where $\hat{\boldsymbol{x}} = (\boldsymbol{x}/r) = \hat{\boldsymbol{e}}_r$ is the unit vector in the radial direction. Here, we have substituted (A11) for $(\mathrm{d}^2\tilde{\chi}/\mathrm{d}r^2)$. The term $\boldsymbol{\nabla}^2(\tilde{\chi}\hat{\boldsymbol{H}})$ in (A10) is simplified as

$$\boldsymbol{\nabla}^2(\tilde{\chi}(r)\hat{\boldsymbol{H}}) = \hat{\boldsymbol{H}}\boldsymbol{\nabla}^2(\tilde{\chi}(r)) = -\hat{\boldsymbol{H}}\tilde{\beta}^2\tilde{\chi}(r), \tag{A14}$$

to obtain the following expression for the magnetic field:

$$\tilde{\boldsymbol{H}} = \tilde{A}\left[\hat{\boldsymbol{H}}\left(\frac{1}{r}\frac{\mathrm{d}\tilde{\chi}}{\mathrm{d}r} + \tilde{\beta}^2\tilde{\chi}\right) + \hat{\boldsymbol{x}}(\hat{\boldsymbol{x}}\cdot\hat{\boldsymbol{H}})\left(-\frac{3}{r}\frac{\mathrm{d}\tilde{\chi}}{\mathrm{d}r} - \tilde{\beta}^2\tilde{\chi}\right)\right]. \tag{A15}$$

The magnetic field outside the sphere satisfies the equations $\boldsymbol{\nabla}\cdot\boldsymbol{H} = 0$ and $\boldsymbol{\nabla}\times\boldsymbol{H} = 0$. The field can be expressed as the gradient of a potential, since it is irrotational, and the solenoidal condition implies the potential satisfies the Laplace equation. Thus, the magnetic field outside the drop can be expressed as the sum of the imposed magnetic field $\hat{\boldsymbol{H}}$ and a disturbance due to the drop,

$$\tilde{\boldsymbol{H}} = \hat{\boldsymbol{H}} + \tilde{B}\boldsymbol{\Phi}^{(2)}\cdot\hat{\boldsymbol{H}}, \tag{A16}$$

where $\boldsymbol{\Phi}^{(2)}$ is the decaying second-order tensor solution of the Laplace equation,

$$\boldsymbol{\Phi}^{(2)} = \boldsymbol{\nabla\nabla}\left(\frac{1}{r}\right) = \frac{(3\boldsymbol{xx} - r^2\boldsymbol{I})}{r^5}. \tag{A17}$$

The continuity of the magnetic field at the surface of the sphere $r = 1$ in the $\hat{\boldsymbol{H}}$ and $\hat{\boldsymbol{x}}$ directions provides the following relations for the constants $\tilde{A}$ and $\tilde{B}$:

$$\tilde{A}\left(\frac{1}{r}\frac{\mathrm{d}\tilde{\chi}}{\mathrm{d}r} + \tilde{\beta}^2\tilde{\chi}\right)\Big|_{r=1} = 1 - \tilde{B}, \tag{A18}$$

$$-\tilde{A}\left(\frac{3}{r}\frac{\mathrm{d}\tilde{\chi}}{\mathrm{d}r} + \tilde{\beta}^2\tilde{\chi}\right)\Big|_{r=1} = 3\tilde{B}. \tag{A19}$$

https://doi.org/10.1017/jfm.2025.10176 Published online by Cambridge University Press

These equations are solved,

$$\tilde{A} = \frac{3}{2\tilde{\beta}^2\ \tilde{\chi}|_{r=1}} = \frac{3}{2\tilde{\beta}^2 \sin(\tilde{\beta})}, \tag{A20}$$

$$\tilde{B} = -\frac{1}{2} - \frac{3}{2\tilde{\beta}^2}\left(\frac{1}{\tilde{\chi}}\frac{\mathrm{d}\tilde{\chi}}{\mathrm{d}r}\right)\bigg|_{r=1} = -\frac{1}{2} + \frac{3}{2\tilde{\beta}^2} - \frac{3\cot(\tilde{\beta})}{2\tilde{\beta}}. \tag{A21}$$

Substituting the expression (A20) for $\tilde{A}$ into (A15), the magnetic field in the drop is

$$\tilde{\boldsymbol{H}} = \frac{3}{2\tilde{\beta}^2 \sin(\tilde{\beta})}\left[\hat{\boldsymbol{H}}\left(\frac{1}{r}\frac{\mathrm{d}\tilde{\chi}}{\mathrm{d}r} + \tilde{\beta}^2\tilde{\chi}\right) + \hat{\boldsymbol{x}}(\hat{\boldsymbol{x}}\cdot\hat{\boldsymbol{H}})\left(-\frac{3}{r}\frac{\mathrm{d}\tilde{\chi}}{\mathrm{d}r} - \tilde{\beta}^2\tilde{\chi}\right)\right]. \tag{A22}$$

In a spherical coordinate system, we substitute $\hat{\boldsymbol{H}} = \hat{\boldsymbol{e}}_r\cos(\theta) - \hat{\boldsymbol{e}}_\theta\sin(\theta)$ and $\hat{\boldsymbol{x}}(\hat{\boldsymbol{x}}\cdot\hat{\boldsymbol{H}}) = \hat{\boldsymbol{e}}_r\cos(\theta)$, to obtain

$$\tilde{\boldsymbol{H}} = -\frac{3}{2\tilde{\beta}^2 \sin(\tilde{\beta})}\left[\frac{2\hat{\boldsymbol{e}}_r\cos(\theta)}{r}\frac{\mathrm{d}\tilde{\chi}}{\mathrm{d}r} + \hat{\boldsymbol{e}}_\theta\sin(\theta)\left(\frac{1}{r}\frac{\mathrm{d}\tilde{\chi}}{\mathrm{d}r} + \tilde{\beta}^2\tilde{\chi}\right)\right]. \tag{A23}$$

Vector plots for the real and imaginary parts of $\tilde{\boldsymbol{H}}$ are shown for three different values of β in figures 15(*c,g,k*) and 15(*d,h,l*). In the absence of the conducting drop, $\mathrm{Re}(\tilde{\boldsymbol{H}})$ is along the z direction, and $\mathrm{Im}(\tilde{\boldsymbol{H}})$ is zero, since we have assumed $\boldsymbol{H}_0$ is real in (A4). For $\beta = 1$, very little distortion of $\mathrm{Re}(\tilde{\boldsymbol{H}})$ is observed in the drop, and $\mathrm{Im}(\tilde{\boldsymbol{H}})$ is small in magnitude compared with $\mathrm{Re}(\tilde{\boldsymbol{H}})$. As β is increased, the distortion in the field lines becomes larger. For $\beta = 3$, the magnitude of $\mathrm{Re}(\tilde{\boldsymbol{H}})$ and $\mathrm{Im}(\tilde{\boldsymbol{H}})$ is larger near the surface of the drop in comparison with the centre. For $\beta = 10$, it is observed that the magnetic field is significant in a thin region at the surface of the drop, and is negligible within the drop. This implies the conducting drop expels the field lines at high frequency.

Asymptotic expressions for $\tilde{\boldsymbol{H}}$ are derived in the limits $\beta \ll 1$ and $\beta \gg 1$. A regular perturbation expansion is used in the limit $\beta \ll 1$,

$$\tilde{\boldsymbol{H}} = \hat{\boldsymbol{e}}_r\cos(\theta)\left(1 - \frac{\imath\beta^2(5-3r^2)}{30}\right) + \hat{\boldsymbol{e}}_\theta\sin(\theta)\left(-1 + \frac{\imath\beta^2(5-6r^2)}{30}\right). \tag{A24}$$

Here, we have substituted $\tilde{\beta} = \sqrt{-\imath}\beta$. It is evident that the disturbance to the magnetic field due to the presence of the drop is proportional to β^2 in the limit $\beta \ll 1$. Moreover, the coefficients multiplying the $O(\beta^2)$ corrections in (A24) are numerically small. Consequently, there is very little deviation in the magnetic field lines for $\beta = 1$ in figure 15.

For the limit $\beta \gg 1$, the terms in the expression for the magnetic field are approximated as follows:

$$\begin{aligned}\frac{\sin(\tilde{\beta}r)}{\sin(\tilde{\beta})} &= \frac{\sin\left[\beta(1/\sqrt{2} - \imath/\sqrt{2})r\right]}{\sin\left[\beta(1/\sqrt{2} - \imath/\sqrt{2})\right]} \\ &= \frac{\exp\left[\imath\beta(1/\sqrt{2} - \imath/\sqrt{2})r\right] - \exp\left[-\imath\beta(1/\sqrt{2} - \imath/\sqrt{2})r\right]}{\exp\left[\imath\beta(1/\sqrt{2} - \imath/\sqrt{2})\right] - \exp\left[-\imath\beta(1/\sqrt{2} - \imath/\sqrt{2})\right]}.\end{aligned} \tag{A25}$$

https://doi.org/10.1017/jfm.2025.10176 Published online by Cambridge University Press

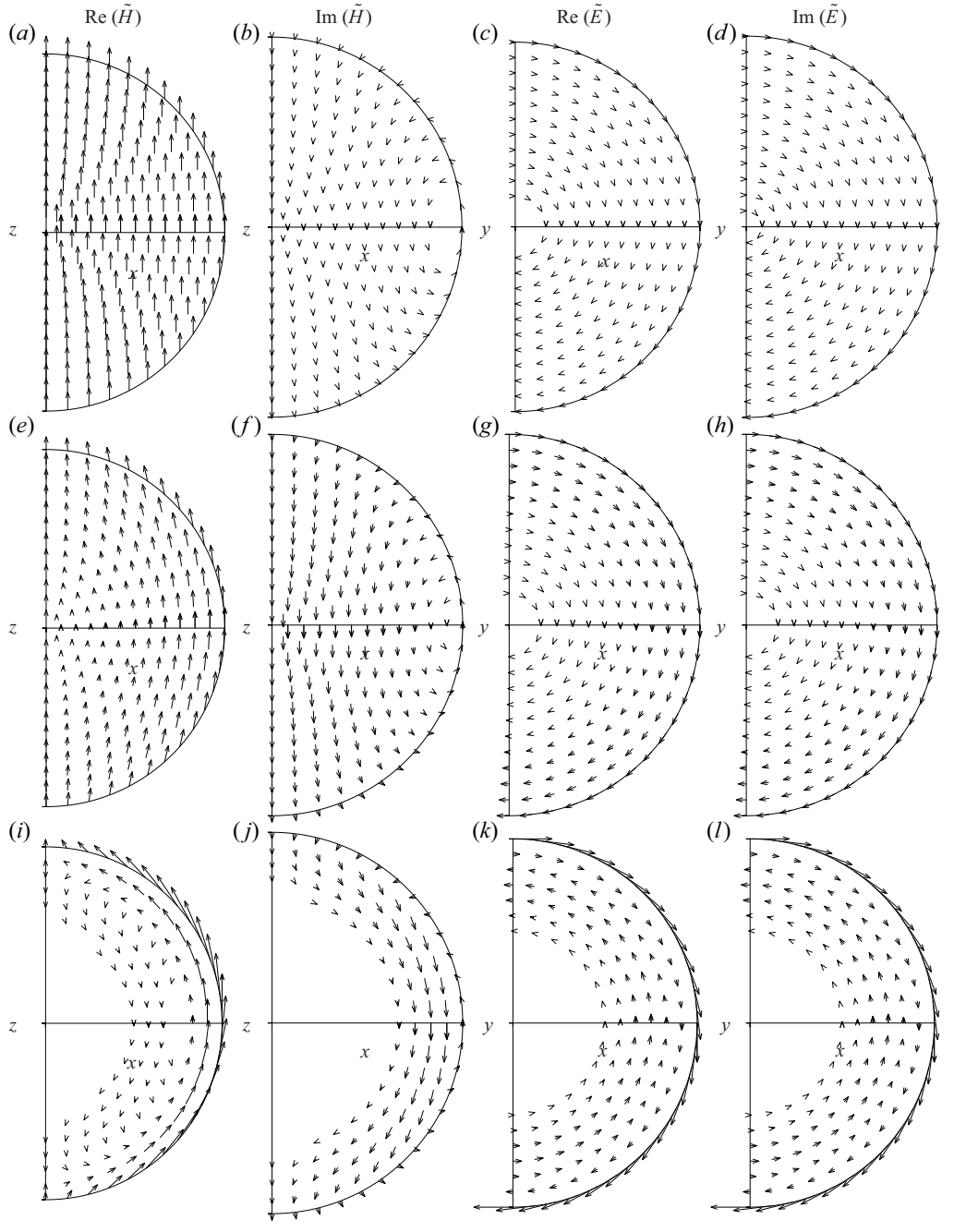


Figure 15. Vector plots of the real and imaginary parts of $\tilde{\boldsymbol{H}}$ and $\tilde{\boldsymbol{E}}$ for $\beta = 1$ (*a–d*), $\beta = 3$ (*e–h*) and $\beta = 10$ (*i–l*) within the spherical drop with boundary shown by the circle. The magnetic field, shown in the $x-z$ (meridional) plane, is axisymmetric about the z axis. The electric field is shown in the $x-y$ (equatorial) plane. At each location, the length of the arrow is proportional to the magnitude of the field. Arrows are not shown at locations where the magnitude of the field is less than 2 % of the maximum magnitude over the domain.

https://doi.org/10.1017/jfm.2025.10176 Published online by Cambridge University Press

The numerator and denominator are divided by $\exp[\iota\beta(1/\sqrt{2}-\iota/\sqrt{2})] = \exp[\beta(1/\sqrt{2}+\iota/\sqrt{2})]$,

$$\frac{\sin(\tilde{\beta}r)}{\sin(\tilde{\beta})} = \frac{\exp\left[-\beta(1/\sqrt{2}+\iota/\sqrt{2})(1-r)\right] - \exp\left[-\beta(1/\sqrt{2}+\iota/\sqrt{2})(1+r)\right]}{1-\exp\left[-2\beta(1/\sqrt{2}+\iota/\sqrt{2})\right]}. \tag{A26}$$

For $\beta \gg 1$, the second terms in the numerator and denominator of the above expression are neglected in comparison with the first terms, to obtain

$$\frac{\sin(\tilde{\beta}r)}{\sin(\tilde{\beta})} = \exp\left[-\beta(1/\sqrt{2}+\iota/\sqrt{2})(1-r)\right]. \tag{A27}$$

The expression above is small for $r \sim 1$, but is $O(1)$ for $(1-r) \sim \beta^{-1}$. Therefore, the ratio $(\sin(\tilde{\beta}r)/\sin(\tilde{\beta}))$ is $O(1)$ only within a region of thickness $O(\beta^{-1})$ close to the surface. A similar calculation can be carried out for $(\cos(\tilde{\beta}r)/\sin(\tilde{\beta}))$,

$$\frac{\cos(\tilde{\beta}r)}{\sin(\tilde{\beta})} = \iota \exp[-\beta(1/\sqrt{2}+\iota/\sqrt{2})(1-r)]. \tag{A28}$$

Using the $\beta \gg 1$ approximations (A27) and (A28), the equation (A23) for the magnetic field reduces to

$$\tilde{\boldsymbol{H}} = \frac{3(1-\iota)\cos(\theta)\hat{\boldsymbol{e}}_r \exp\left[-\beta\left(1/\sqrt{2}+\iota/\sqrt{2}\right)(1-r)\right]}{\sqrt{2}\beta r^2} - \frac{3\sin(\theta)\hat{\boldsymbol{e}}_\theta \exp\left[-\beta\left(1/\sqrt{2}+\iota/\sqrt{2}\right)(1-r)\right]}{2r}. \tag{A29}$$

Here, we have retained only the dominant contributions to $\tilde{\boldsymbol{H}}$, which are $O(\beta^{-1})$ in the $\hat{\boldsymbol{e}}_r$ direction and $O(1)$ in the $\hat{\boldsymbol{e}}_\theta$ direction.

The magnetic field decreases exponentially away from the surface over a distance comparable with β^{-1} in the limit $\beta \gg 1$, and it is small at the centre of the drop. This decrease is shown in the vector plots for $\mathrm{Re}(\tilde{\boldsymbol{H}})$ and $\mathrm{Im}(\tilde{\boldsymbol{H}})$ for $\beta = 10$ in figure 15. From (A29), it can also be inferred that the component of $\tilde{\boldsymbol{H}}$ in the $\hat{\boldsymbol{e}}_r$ direction is $O(\beta^{-1})$ close to the surface, while the oscillating component in the $-\hat{\boldsymbol{e}}_\theta$ direction is $O(1)$ and real. Therefore, the real part of the oscillating magnetic field is primarily in the $-\hat{\boldsymbol{e}}_\theta$ direction for $\beta = 10$ in figure 15, and the imaginary part is much smaller.

The electric field in the drop is determined from (A2),

$$\tilde{\boldsymbol{E}} = \boldsymbol{\nabla} \times \tilde{\boldsymbol{H}}. \tag{A30}$$

If we take the curl of the expression (A23) for the magnetic field, the expression for the electric field in the dropis

$$\tilde{\boldsymbol{E}} = -\frac{3\sin(\theta)\hat{\boldsymbol{e}}_\phi}{2\sin(\tilde{\beta})}\frac{\mathrm{d}\tilde{\chi}}{\mathrm{d}r}. \tag{A31}$$

The electric field is in the meridional direction perpendicular to the $r-\theta$ plane. The vector plots for $\mathrm{Re}(\tilde{\boldsymbol{E}})$ and $\mathrm{Im}(\tilde{\boldsymbol{E}})$ are shown in the $x-y$ (equatorial) plane in figures 15(*c,g,k*) and 15(*d,h,l*). The asymptotic expression for $\tilde{\boldsymbol{E}}$ for $\beta \ll 1$ is

$$\tilde{\boldsymbol{E}} = -\frac{\iota\beta^2 r\sin(\theta)\hat{\boldsymbol{e}}_\phi}{2}. \tag{A32}$$

https://doi.org/10.1017/jfm.2025.10176 Published online by Cambridge University Press

The electric field in the equatorial $x-y$ plane for $\beta = 1$ is shown in figure 15(a–d). In agreement with (A32), the electric field is in the $-\hat{\boldsymbol{e}}_\phi$ direction. Not apparent in figure 15 is that the imaginary part of the electric field is much larger than the real part, which is $O(\beta^4)$. The approximation (A32) is in numerical agreement, to within 1%, with the solution (A31) for $\beta = 1$. Equation (A28) is substituted into (A31) to obtain the asymptotic expression for $\tilde{\boldsymbol{E}}$ in the limit $\beta \gg 1$,

$$\tilde{\boldsymbol{E}} = -\frac{3(1+\imath)\beta \exp\left[-\beta\left(1/\sqrt{2}+\imath/\sqrt{2}\right)(1-r)\right]\sin(\theta)\hat{\boldsymbol{e}}_\phi}{2\sqrt{2}r}. \tag{A33}$$

The scaled electric field is $O(\beta)$ in a region of thickness β^{-1} close to the surface, and it decreases exponentially away from the surface in the limit $\beta \gg 1$.

The electric field outside the drop satisfies the Laplace equation $\boldsymbol{\nabla}^2\boldsymbol{E} = 0$, and is a linear function of the pseudovector $\hat{\boldsymbol{H}}$. Therefore, the electric field is necessarily of the form

$$\tilde{\boldsymbol{E}} = \tilde{C}\hat{\boldsymbol{H}} \times \boldsymbol{\Phi}^{(1)}, \tag{A34}$$

where $\boldsymbol{\Phi}^{(1)}$ is the decaying vector solution of the Laplace equation,

$$\boldsymbol{\Phi}^{(1)} = \boldsymbol{\nabla}\left(\frac{1}{r}\right) = -\frac{\boldsymbol{x}}{r^3}. \tag{A35}$$

The constant $\tilde{C}$ is determined from the boundary condition for the electric field at the spherical surface $r = 1$. The solutions (A31) and (A34) are consistent with the zero normal electric field condition at the interface between the conducting drop and the dielectric medium. The continuity condition for the tangential component of the electric field at the surface reduces to

$$\tilde{C} = \frac{3}{2\sin(\tilde{\beta})}\left.\frac{\mathrm{d}\tilde{\chi}}{\mathrm{d}r}\right|_{r=1} = \frac{3(\tilde{\beta}\cot(\tilde{\beta})-1)}{2}. \tag{A36}$$

Here, we have substituted $\tilde{\chi} = \sin(\tilde{\beta}r)/r$.

Appendix B. Force density

The Lorentz force density is expressed in dimensionless form as

$$\boldsymbol{f} = \boldsymbol{J} \times \boldsymbol{H} = \boldsymbol{E} \times \boldsymbol{H}. \tag{B1}$$

The force density $\boldsymbol{f}$ within the drop can be expressed as the sum of a steady and an oscillating part,

$$\boldsymbol{f} = \bar{\boldsymbol{f}} + \tfrac{1}{2}(\tilde{\boldsymbol{f}}\exp(2\imath t) + (\tilde{\boldsymbol{f}}\exp(2\imath t))^*), \tag{B2}$$

where the steady and oscillating components are

$$\bar{\boldsymbol{f}} = \tfrac{1}{4}(\tilde{\boldsymbol{E}} \times \tilde{\boldsymbol{H}}^* + \tilde{\boldsymbol{E}}^* \times \tilde{\boldsymbol{H}}), \quad \tilde{\boldsymbol{f}} = \tfrac{1}{2}(\tilde{\boldsymbol{E}} \times \tilde{\boldsymbol{H}}). \tag{B3}$$

B.1 *Steady component of force density*

Equation (B3) for the steady component of the force density is expressed using (A23) and (A31) for the magnetic and electric fields. The two terms in the expression for the steady

https://doi.org/10.1017/jfm.2025.10176 Published online by Cambridge University Press

force, (B3), are evaluated using the cross products $\hat{\boldsymbol{e}}_\phi \times \hat{\boldsymbol{e}}_r = \hat{\boldsymbol{e}}_\theta$ and $\hat{\boldsymbol{e}}_\phi \times \hat{\boldsymbol{e}}_\theta = -\hat{\boldsymbol{e}}_r$,

$$\frac{1}{4}(\tilde{\boldsymbol{E}} \times \tilde{\boldsymbol{H}}^*) = \frac{9\sin(\theta)}{16\tilde{\beta}^{*2}\sin(\tilde{\beta})\sin(\tilde{\beta}^*)}\frac{\mathrm{d}\tilde{\chi}}{\mathrm{d}r}\left[\frac{2\cos(\theta)\hat{\boldsymbol{e}}_\theta}{r}\frac{\mathrm{d}\tilde{\chi}^*}{\mathrm{d}r} - \hat{\boldsymbol{e}}_r\sin(\theta)\left(\frac{1}{r}\frac{\mathrm{d}\chi^*}{\mathrm{d}r} + \tilde{\beta}^{*2}\tilde{\chi}^*\right)\right], \tag{B4}$$

$$\frac{1}{4}(\tilde{\boldsymbol{E}}^* \times \tilde{\boldsymbol{H}}) = \frac{9\sin(\theta)}{16\tilde{\beta}^{2}\sin(\tilde{\beta})\sin(\tilde{\beta}^*)}\frac{\mathrm{d}\tilde{\chi}^*}{\mathrm{d}r}\left[\frac{2\cos(\theta)\hat{\boldsymbol{e}}_\theta}{r}\frac{\mathrm{d}\tilde{\chi}}{\mathrm{d}r} - \hat{\boldsymbol{e}}_r\sin(\theta)\left(\frac{1}{r}\frac{\mathrm{d}\chi}{\mathrm{d}r} + \tilde{\beta}^{2}\tilde{\chi}\right)\right]. \tag{B5}$$

The two terms are added, and we substitute $\tilde{\beta} = \sqrt{-\imath}\beta$, $\tilde{\beta}^* = \sqrt{\imath}\beta$ and $\tilde{\beta}^{*2} = -\tilde{\beta}^2$. It is apparent that the terms proportional to $(\mathrm{d}\chi/\mathrm{d}r) \times (\mathrm{d}\chi^*/\mathrm{d}r)$ sum to zero in the above equations, and the final expression for the steady force density is

$$\bar{\boldsymbol{f}} = -\frac{9\sin(\theta)^2\hat{\boldsymbol{e}}_r}{16\sin(\tilde{\beta})\sin(\tilde{\beta}^*)}\frac{\mathrm{d}(\tilde{\chi}\tilde{\chi}^*)}{\mathrm{d}r}. \tag{B6}$$

The last term on the right-hand side in (B6) simplified as

$$\frac{\mathrm{d}(\tilde{\chi}\tilde{\chi}^*)}{\mathrm{d}r} = \frac{\mathrm{d}}{\mathrm{d}r}\left(\frac{\sin(\tilde{\beta}r)\sin(\tilde{\beta}^*r)}{r^2}\right) = \frac{\mathrm{d}}{\mathrm{d}r}\left(\frac{\cos((\tilde{\beta}-\tilde{\beta}^*)r) - \cos((\tilde{\beta}+\tilde{\beta}^*)r)}{2r^2}\right). \tag{B7}$$

Substituting $\tilde{\beta} = \sqrt{-\imath}\beta = (1/\sqrt{2} - \imath/\sqrt{2})\beta$ and $\tilde{\beta}^* = (1/\sqrt{2} + \imath/\sqrt{2})\beta$, we obtain

$$\frac{\mathrm{d}(\tilde{\chi}\tilde{\chi}^*)}{\mathrm{d}r} = \frac{\mathrm{d}}{\mathrm{d}r}\left(\frac{\cosh(\sqrt{2}\beta r) - \cos(\sqrt{2}\beta r)}{2r^2}\right) = \frac{\beta(\sinh(\sqrt{2}\beta r) + \sin(\sqrt{2}\beta r))}{\sqrt{2}r^2} - \frac{\cosh(\sqrt{2}\beta r) - \cos(\sqrt{2}\beta r)}{r^3}. \tag{B8}$$

In a similar manner, the denominator of (B6) is simplified as follows:

$$\frac{1}{\sin(\tilde{\beta})\sin(\tilde{\beta}^*)} = \frac{1}{\frac{1}{2}(\cosh(\sqrt{2}\beta) - \cos(\sqrt{2}\beta))}. \tag{B9}$$

With these simplifications, the expression for the steady force is

$$\bar{\boldsymbol{f}} = -\frac{9\sin(\theta)^2\hat{\boldsymbol{e}}_r}{8(\cosh(\sqrt{2}\beta) - \cos(\sqrt{2}\beta))} \times \left(\frac{\beta(\sinh(\sqrt{2}\beta r) + \sin(\sqrt{2}\beta r))}{\sqrt{2}r^2} - \frac{\cosh(\sqrt{2}\beta r) - \cos(\sqrt{2}\beta r)}{r^3}\right). \tag{B10}$$

Thus, the steady component of the force is in the radial direction.

The forcing term in equation for the steady part of the stream function, (2.8), is

$$-\sin(\theta)\frac{\partial \bar{f}_r}{\partial\theta} = \sin(\theta)^2\cos(\theta)\bar{F}(r), \tag{B11}$$

https://doi.org/10.1017/jfm.2025.10176 Published online by Cambridge University Press

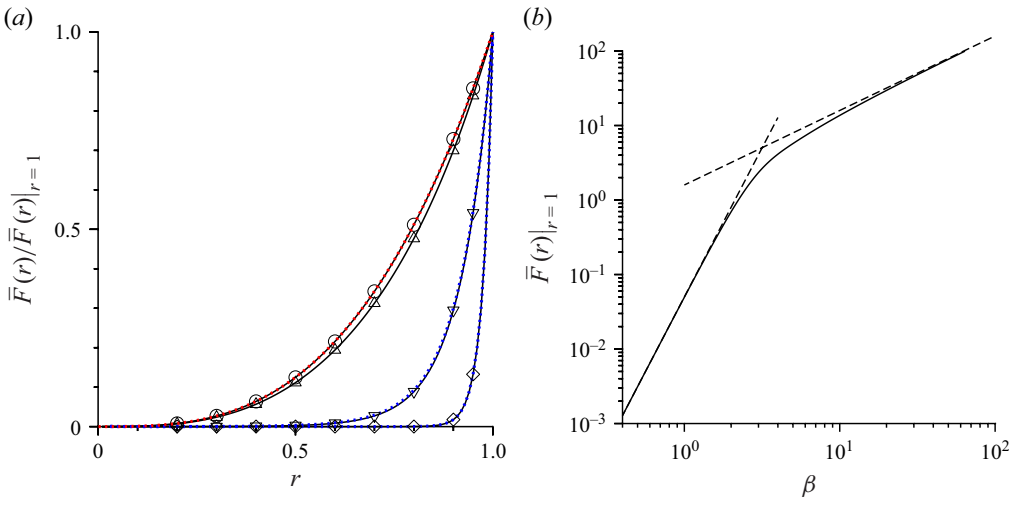


Figure 16. The variation of (*a*) the ratio $\bar{F}(r)/\bar{F}(r)|_{r=1}$ with r for $\beta = 1$ (○), $\beta = 3$ (△), $\beta = 10$ (▽), $\beta = 30$ (◇), and (*b*) the variation of the forcing at the surface $\bar{F}(r)|_{r=1}$ with β. In (*a*), the red line is $\bar{F}(r)/\bar{F}(r)|_{r=1} = r^3$ obtained from (B13), and the blue lines are $\bar{F}(r)/\bar{F}(r)|_{r=1} = (\exp(-\beta\sqrt{2}(1-r))/r^2)$ obtained from (B14). In (*b*), the dashed line on the left is $\bar{F}(r)|_{r=1} = (\beta^4/20)$ obtained from (B13), and the dashed line on the right is $\bar{F}(r)|_{r=1} = (9\beta/4\sqrt{2})$ obtained from (B14).

where

$$\bar{F}(r) = \left(\frac{9}{4(\cosh(\sqrt{2}\beta) - \cos(\sqrt{2}\beta))}\right) \times \left(\frac{\beta(\sinh(\sqrt{2}\beta r) + \sin(\sqrt{2}\beta r))}{\sqrt{2}r^2} - \frac{\cosh(\sqrt{2}\beta r) - \cos(\sqrt{2}\beta r)}{r^3}\right). \quad \text{(B12)}$$

The approximations for $\bar{F}$ in the limits of low and high β are

$$\bar{F} = \left(\frac{\beta^4 r^3}{20}\right) \text{ for } \beta \ll 1, \quad \text{(B13)}$$

$$= \left(\frac{9\beta \exp\left[-\beta\sqrt{2}(1-r)\right]}{4\sqrt{2}r^2}\right) \text{ for } \beta \gg 1. \quad \text{(B14)}$$

For $\beta \ll 1$, $\bar{F}$ increases proportional to β^4. For $\beta \gg 1$, $\bar{F}$ is significant only in a thin layer of thickness β^{-1} close to the surface, and it decreases exponentially away from the surface.

The variation of $\bar{F}$ with r is shown in figure 16(*a*) for different values of β. To facilitate comparison, $\bar{F}(r)$ is scaled by its value at the surface $\bar{F}(r)\big|_{r=1}$ in this figure. The dashed red line is obtained from the $\beta \ll 1$ asymptotic result (B13), $(\bar{F}/\ \bar{F}\big|_{r=1}) = r^3$. It is observed that the asymptotic result is in quantitative agreement with the numerical result for $\beta \leqslant 1$. This is due to the small numerical factor $\frac{1}{20}$ premultiplying the $O(\beta^4)$ term in (B13). There is good agreement between the $\beta \ll 1$ asymptotic result and numerical result even for $\beta = 3$. The blue lines, obtained from the $\beta \gg 1$ asymptotic result (B14), are in quantitative agreement with the numerical results for $\beta \geqslant 10$. In agreement with the asymptotic prediction, the forcing is restricted to a thin region of thickness $\sim \beta^{-1}$ close to the surface for $\beta \gg 1$.

https://doi.org/10.1017/jfm.2025.10176 Published online by Cambridge University Press

Figure 16(*b*) shows the variation of the forcing at the surface, $\bar{F}(r)\big|_{r=1}$, with β. The forcing at the surface increases proportional to β^4, as predicted by (B13), for $\beta \lesssim 3$, and it increases proportional to β, as predicted by (B14), for $\beta \gtrsim 10$.

Oscillatory component of force density

Substituting (A31) for $\tilde{\boldsymbol{E}}$ and (A20) for $\tilde{\boldsymbol{H}}$ into (B3), the oscillating component of the force density is

$$\tilde{\boldsymbol{f}} = \frac{9\sin(\theta)}{8\tilde{\beta}^2\sin(\tilde{\beta})^2}\frac{\mathrm{d}\tilde{\chi}}{\mathrm{d}r}\left[\frac{2\cos(\theta)\hat{\boldsymbol{e}}_\theta}{r}\left(\frac{\mathrm{d}\tilde{\chi}}{\mathrm{d}r}\right) - \sin(\theta)\hat{\boldsymbol{e}}_r\left(\frac{1}{r}\frac{\mathrm{d}\tilde{\chi}}{\mathrm{d}r} + \tilde{\beta}^2\tilde{\chi}\right)\right]. \tag{B15}$$

The expression (A9) is used for $\tilde{\chi}$, and the oscillating force density is expressed as

$$\begin{aligned}\tilde{\boldsymbol{f}} &= \tilde{f}_r\hat{\boldsymbol{e}}_r + \tilde{f}_\theta\hat{\boldsymbol{e}}_\theta \\ &= \tilde{F}_r\sin(\theta)^2\hat{\boldsymbol{e}}_r + \tilde{F}_\theta\sin(\theta)\cos(\theta)\hat{\boldsymbol{e}}_\theta,\end{aligned} \tag{B16}$$

where $\tilde{F}_r$ and $\tilde{F}_\theta$ are functions of r,

$$\begin{aligned}\tilde{F}_r = -\frac{9}{8\tilde{\beta}^2\sin(\tilde{\beta})^2 r}&\left(\frac{\tilde{\beta}\cos(\tilde{\beta}r)}{r} - \frac{\sin(\tilde{\beta}r)}{r^2} + \tilde{\beta}^2\sin(\tilde{\beta}r)\right) \\ &\times\left(\frac{\tilde{\beta}\cos(\tilde{\beta}r)}{r} - \frac{\sin(\tilde{\beta}r)}{r^2}\right),\end{aligned} \tag{B17}$$

$$\tilde{F}_\theta = \frac{9}{4\tilde{\beta}^2\sin(\tilde{\beta})^2 r}\left(\frac{\tilde{\beta}\cos(\tilde{\beta}r)}{r} - \frac{\sin(\tilde{\beta}r)}{r^2}\right)^2. \tag{B18}$$

The forcing in (2.8) is proportional to the curl of the force density,

$$\sin(\theta)\left(\frac{\partial(r\tilde{f}_\theta)}{\partial r} - \frac{\partial\tilde{f}_r}{\partial\theta}\right) = \sin(\theta)^2\cos(\theta)\tilde{F}(r), \tag{B19}$$

where

$$\begin{aligned}\tilde{F}(r) = \frac{9}{4\sin(\tilde{\beta})^2}&\left(-\frac{\tilde{\beta}\cos(\tilde{\beta}r)\sin(\tilde{\beta}r)}{r^2} + \frac{\sin(\tilde{\beta}r)^2 - 3\cos(\tilde{\beta}r)^2}{r^3}\right. \\ &\left. + \frac{6\cos(\tilde{\beta}r)\sin(\tilde{\beta}r)}{\tilde{\beta}r^4} - \frac{3\sin(\tilde{\beta}r)^2}{\tilde{\beta}^2r^5}\right).\end{aligned} \tag{B20}$$

The expansions for $\tilde{F}_r(r)$, $\tilde{F}_\theta(r)$ and $\tilde{F}(r)$ in the limits $\beta \ll 1$ and $\beta \gg 1$ are

$$\tilde{F}_r(r) = -\frac{\imath\beta^2 r}{4} + \frac{\beta^4 r(9r^2-10)}{120} \quad \text{for } \beta \ll 1, \tag{B21}$$

$$= -\frac{9(1+\imath)\beta\exp\left(-\sqrt{2}(1+\imath)\beta(1-r)\right)}{8\sqrt{2}r^2} \quad \text{for } \beta \gg 1, \tag{B22}$$

$$\tilde{F}_\theta(r) = -\frac{\imath\beta^2 r}{4} + \frac{\beta^4 r(3r^2-5)}{60} \quad \text{for } \beta \ll 1, \tag{B23}$$

https://doi.org/10.1017/jfm.2025.10176 Published online by Cambridge University Press

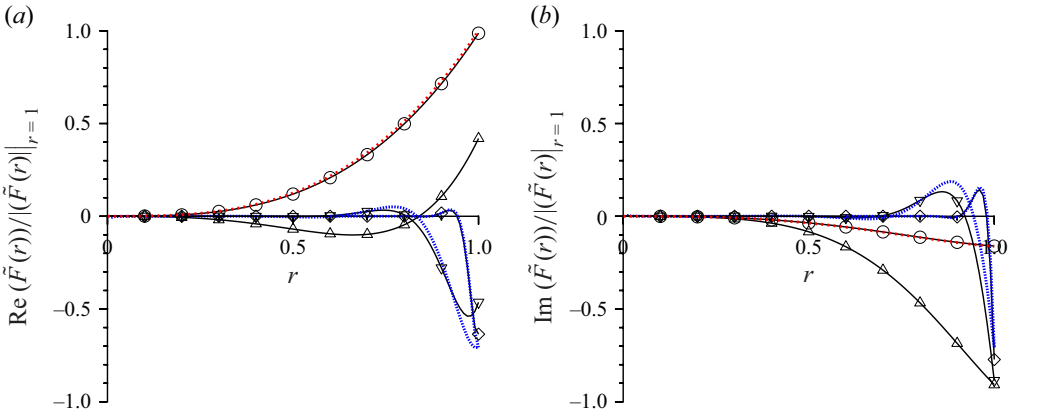


Figure 17. The variation of (*a*) the ratio $\mathrm{Re}(\tilde{F}(r))/|\tilde{F}(r)||_{r=1}$ and (*b*) the ratio $\mathrm{Im}(\tilde{F}(r))/|\tilde{F}(r)||_{r=1}$ with r for $\beta = 1$ ($\circ$), $\beta = 3$ ($\triangle$), $\beta = 10$ (∇), $\beta = 30$ ($\diamond$), and (*b*) the variation of the forcing at the surface $\tilde{F}(r)|_{r=1}$ with β. The red lines are obtained from the $\beta \ll 1$ asymptotic result, (B25), for $\beta = 1$, and the blue lines obtained from the $\beta \gg 1$ asymptotic result, (B26), for $\beta = 10$ and $\beta = 30$.

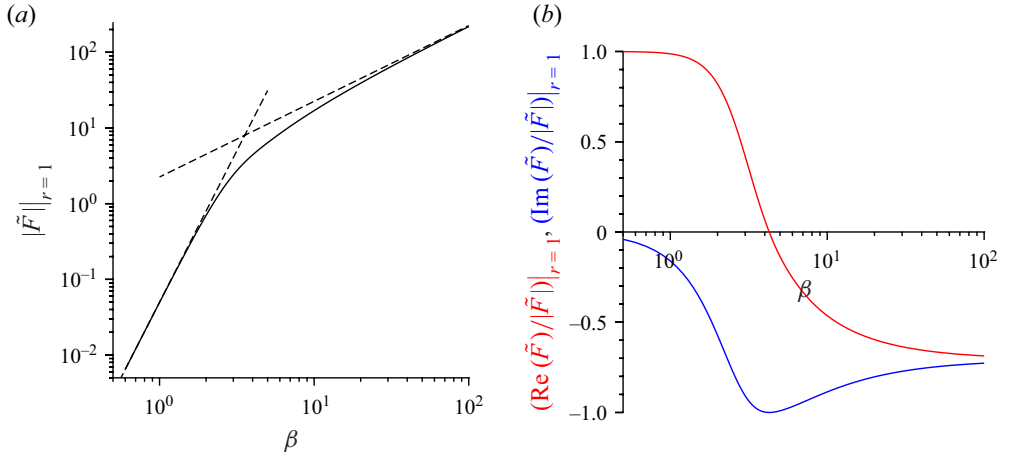


Figure 18. The variation of (*a*) $|\tilde{F}(r)||_{r=1}$ and (*b*) the ratios $(\mathrm{Re}(\tilde{F})/|\tilde{F}(r)|)|_{r=1}$ (red) and $((\mathrm{Im}(\tilde{F})/|\tilde{F}|)|_{r=1}$ (blue) with β. In (*a*), the dashed line on the left is obtained from the $\beta \ll 1$ asymptotic result, (B25), and the dashed line on the right is the $\beta \gg 1$ asymptotic result, (B26).

$$= -\frac{9\exp\left(-\sqrt{2}(1+\imath)\beta(1-r)\right)}{4r^3} \quad \text{for } \beta \gg 1, \tag{B24}$$

$$\tilde{F}(r) = \frac{\beta^4 r^3}{20} \quad \text{for } \beta \ll 1, \tag{B25}$$

$$= -\frac{9(1+\imath)\beta\exp\left(-\sqrt{2}(1+\imath)\beta(1-r)\right)}{4\sqrt{2}r^2} \quad \text{for } \beta \gg 1. \tag{B26}$$

To derive the approximation (B26), only the terms multiplied by $\tilde{\beta}$ are retained in (B20), and the approximations (A27) and (A28) are used.

The real and imaginary parts of $\tilde{F}$, scaled by $|\tilde{F}|\Big|_{r=1}$, are shown in figure 17. There is quantitative agreement with the numerical result and the $\beta \ll 1$ asymptotic result, (B25),

https://doi.org/10.1017/jfm.2025.10176 Published online by Cambridge University Press

for $\beta \lesssim 1$. For $\beta \gtrsim 10$, the $\beta \gg 1$ asymptotic result, (B26), is in quantitative agreement with the numerical result.

The magnitude of $\tilde{F}$ at the surface, $r = 1$, is shown as a function of β in figure 18(*a*). The two scalings predicted by (B25) and (B26) are in quantitative agreement with the numerical results for $\beta \lesssim 1$ and $\beta \gtrsim 10$, respectively. The ratios $(\mathrm{Re}(\tilde{F})/|\tilde{F}|)\big|_{r=1}$ and $(\mathrm{Im}(\tilde{F})/|\tilde{F}|)\big|_{r=1}$ are shown in figure 18(*b*). The ratio $(\mathrm{Re}(\tilde{F})/|\tilde{F}|)\big|_{r=1}$ is close to 1 for $\beta \ll 1$, indicating that the forcing is in phase with the magnetic field oscillation. This is consistent with the $\beta \ll 1$ asymptotic expression, (B25). For $\beta \gg 1$, both the real and imaginary part of $\tilde{F}$ are $-(1/\sqrt{2})$ times $|\tilde{F}|$. This is consistent with the $\beta \gg 1$ asymptotic expression, (B26).

References

ALMOG, Y. & FRANKEL, I. 1995 The motion of axisymmetric dipolar particles in a homogeneous shear flow. *J. Fluid Mech.* **289**, 243–261.

BATCHELOR, G.K. 1970 The stress in a suspension of force-free particles. *J. Fluid Mech.* **41** (3), 545–570.

BOLCATO, R., ETAY, J., FAUTRELLE, Y. & MOFFATT, H.K. 1993 Electromagnetic billiards. *Phys. Fluids A: Fluid Dyn.* **5** (7), 1852–1853.

CHAVES, A., ZAHN, M. & RINALDI, C. 2008 Spin-up flow of ferrofluids: asymptotoic theory and experimental measurements. *Phys. Fluids* **20** (5), 053102.

DAS, D. & SAINTILLAN, D. 2021 A three-dimensional small-deformation theory for electrohydrodynamics of dielectric drops. *J. Fluid Mech.* **914**, A22.

DAVIDSON, P.A. 1999 Magnetohydrodynamics in materials processing. *Annu. Rev. Fluid Mech.* **31** (1), 273–300.

EDWARDS, P.P., RAO, C.N.R., KUMAR, N. & ALEXANDROV, A.S. 2006 The possibility of a liquid superconductor. *ChemPhysChem* **7** (9), 2015–2021.

FENG, J.Q. & SCOTT, T.C. 1996 A computational analysis of electrohydrodynamics of a leaky dielectric drop in an electric field. *J. Fluid Mech.* **311** (-1), 289–326.

HAPPEL, J. & BRENNER, H. 1983 Low Reynolds number hydrodynamics. *The Hague*. Martinus Nijhoff Publishers.

HINCH, E.J. & LEAL, L.G. 1979 Rotation of small non-axisymmetric particles in a simple shear flow. *J. Fluid Mech.* **92** (3), 591–608.

JEFFERY, G.B. 1923 The motion of ellipsoidal particles immersed in a viscous fluid. *Proc. R. Soc. A* **123**, 161–179.

KARYAPPA, R.B., DESHMUKH, S.D. & THAOKAR, R.M. 2014 Breakup of a conducting drop in a uniform electric field. *J. Fluid Mech.* **754**, 550–589.

KLINGENBERG, D.J. 2001 Magnetorheology: applications and challenges. *AIChE J.* **47** (2), 246–249.

KLINGENBERG, D.J., ULICNY, JC. & GOLDEN, M.A. 2007 Mason numbers for magnetorheology. *J. Rheol.* **51** (5), 883–893.

KUMARAN, V. 2019 Rheology of a suspension of conducting particles in a magnetic field. *J. Fluid Mech.* **871**, 139–185.

KUMARAN, V. 2020*a* Bifurcations in the dynamics of a dipolar spheroid in a shear flow subjected to an external field. *Phys. Rev. Fluids* **5** (3), 033701.

KUMARAN, V. 2020*b* A suspension of conducting particles in a magnetic field - the maxwell stress. *J. Fluid Mech.* **901**.

KUMARAN, V. 2021*a* Dynamics of polarizable spheroid in a shear flow subjected to a parallel magnetic field. *Phys. Rev. Fluids* **6** (4), 043702.

KUMARAN, V. 2021*b* Steady and rotating states of a polarizable spheroid subjected to a magnetic field and a shear flow. *Phys. Rev. Fluids* **6** (6), 063701.

KUMARAN, V. 2022 The effect of inter-particle hydrodynamic and magnetic interactions in a magnetorheological fluid. *J. Fluid Mech.* **944**, A49.

KUMARAN, V. 2024 Eddies driven by eddy currents: magnetokinetic flow in a conducting drop due to an oscillating magnetic field. *Europhys. Lett.* **148** (6), 63001.

LANDAU, L.D., LIFSHITZ, E.M. & PITAEVSKII, L.P. 2014 *Electrodynamics of Continuous Media*. Butterworth-Heinemann.

https://doi.org/10.1017/jfm.2025.10176 Published online by Cambridge University Press

MELCHER, J.R. & TAYLOR, G.I. 1969 Electrohydrodynamics: a review of the role of interfacial shear stresses. *Annu. Rev. Fluid Mech.* **1** (1), 111–146.
MHATRE, S., DESHMUKH, S. & THAOKAR, R. 2015 Electrocoalescence of a drop pair. *Phys. Fluids* **27** (9), 092106.
MISRA, I. & KUMARAN, V. 2024*a* Dynamics of a magnetic particle in an oscillating magnetic field. *Phys. Rev. Fluids* **9** (7), 074303.
MISRA, I. & KUMARAN, V. 2024*b* Dynamics of a magnetic particle in an oscillating magnetic field subject to a shear flow. *J. of Fluid Mech.* **988**, A49.
MOFFATT, H.K. 1978 *Magnetic Field Generation in Electrically Conducting Fluids*. Cambridge University Press.
MOFFATT, H.K. 1990 On the behaviour of a suspension of conducting particles subjected to a time-periodic magnetic field. *J. Fluid Mech.* **218** (-1), 509–529.
MOFFATT, H.K. 1991 Electromagnetic stirring. *Phys. Fluids* **3** (5), 1336–1343.
MOSKOWITZ, R. & ROSENSWEIG, R.E. 1967 Nonmechanical torque-driven flow of a ferromagnetic fluid by an electromagnetic field. *Appl. Phys. Lett.* **11** (10), 301–303.
PUYESKY, I. & FRANKEL, I. 1998 The motion of a dipolar spherical particle in homogeneous shear and time-periodic fields. *J. Fluid Mech.* **369**, 191–216.
RAYLEIGH, L. 1882 On the equilibrium of liquid conducting masses charged with electricity. *Phil. Mag.* **14** (87), 184–186.
RINALDI, C. & ZAHN, M. 2002 Effects of spin viscosity on ferrofluid flow profiles in alternating and rotating magnetic fields. *Phys. Fluids* **14** (8), 2847–2870.
ROSENSWEIG, R.E. 2023 Spin-up flow in ferrofluids: a toy model. *Eur. Phys. J. E* **46** (9), 83.
ROSENSWEIG, R.E. 2000 Continuum equations for magnetic and dielectric fluids with internal rotations. *J. Chem. Phys.* **121** (3), 1228–1242.
SHERMAN, S.G., BECNEL, A.C. & WERELEY, N.M. 2015 Relating Mason number to Bingham number in magnetorheological fluids. *J. Magn. Magn. Mater.* **380**, 98–104.
SHVYDKIY, E., BAAKE, E. & KOPPEN, D. 2020 Liquid metal flow under traveling magnetic field–solidification simulation and pulsating flow analysis. *Metals* **10** (4), 532.
SOBECKI, C.A., ZHANG, J., ZHANG, Y. & WANG, C. 2018 Dynamics of paramagnetic and ferromagnetic ellipsoidal particles in shear flow under a uniform magnetic field. *Phys. Rev. Fluids* **3** (8), 084201.
SQUIRES, T.M. & BAZANT, M.Z. 2004 Induced-charge electro-osmosis. *J. Fluid Mech.* **509**, 217–252.
STOKES, V.K. 1966 Couple stresses in fluids. *Phys. Fluids* **9** (9), 1709–1715.
TAYLOR, G.I. 1964 Disintegration of water drops in an electric field. *Proc. R. Soc. Lond. A* **280** (1382), 383–397.
TAYLOR, G.I. 1966 Studies in electrohydrodynamics. I. The circulation produced in a drop by an electric field. *Proc. R. Soc. Lond. A* **291** (1425), 159–166.
TIMOFEEV, V.N. & KHATSAYUK, M.YU 2016 Theoretical design fundamentals for MHD stirrers for molten metals. *Magnetohydrodynamics* **52** (4), 495–506.
DE VICENTE, J., KLINGENBERG, D.J. & HIDALGO-ALVAREZ, R. 2011 Magnetorheological fluids: a review. *Soft Matter* **7** (8), 3701–3710.
ZAITSEV, V.M. & SHLIOMIS, M.I. 1969 Entrainment of ferromagnetic suspension by a rotating field. *J. Appl. Mech. Tech. Phys.* **10** (5), 696–700.

https://doi.org/10.1017/jfm.2025.10176 Published online by Cambridge University Press